Master thesis

On the Structure and Geothermal Energy Potential of the Sedimentary Basins of Africa

Jetze Hofstra, 6148808

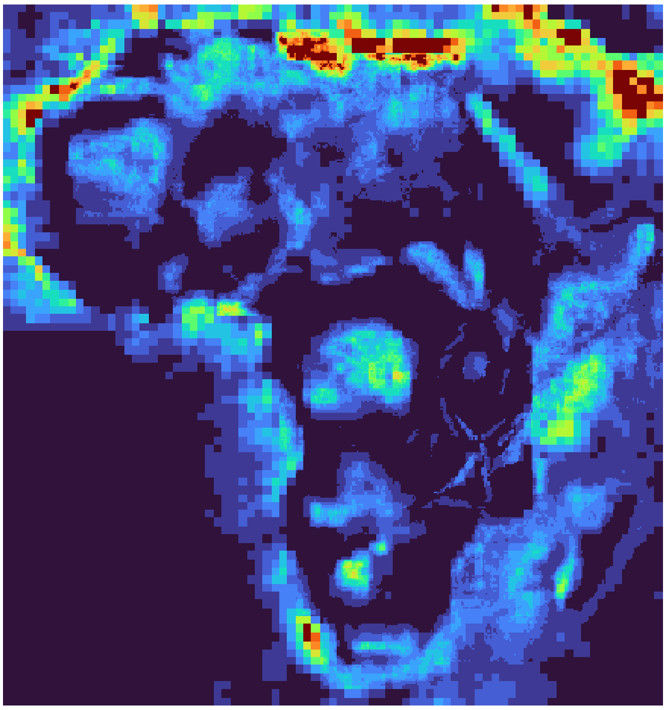

Figure 1: Sediment thickness of the sedimentary basins of Africa.

First advisor: dr. Fred Beekman (UU)

Second advisor: Prof. dr. Jan-Diederik van Wees (TNO/UU)

March 2024

Abstract

The increase in the African population size and the corresponding increase in energy demand is one of the most relevant challenges facing continental Africa to date. This problem, coupled with the need for the reduction of greenhouse gases in the context of climate change, exacerbates the demand for more sustainable renewable energy sources. Harnessing geothermal energy (the energy/heat stored in the earth) might provide a solution in meeting these energy demands.

In this research, we provide constrains on some of the key parameters that are important for determining preliminary geothermal energy resources potential estimates of Africans sedimentary basins. Here we provide estimates and comparisons on the porosity-depth relationships of the sedimentary basins of Africa to determine if these are similar enough to be assumed identical for modelling purposes. We also provide a 25km resolution sediment thickness map for continental Africa.

Given the scale of the continent and the heterogeneous nature of the quality of the available data, few studies have attempted to model the geothermal energy resource potential of Africa. The ones that did, have made assumptions due to the scarcity and poor quality of the available data that largely ignore the differences between basins and their potential reservoirs. Additionally, we find that the current highest resolution public sediment thickness map for Africa, is insufficient for performing more detailed numerical modelling of the resource potential.

We compile publicly available Porosity-depth data and construct basins specific porosity-depth relationships based on standard burial compaction equations. These curves are subsequently analysed to determine potential burial anomalies and their discrepancies with standard clastic sediment curves. The new sediment thickness map is created via the Basin3D inversion modelling software of TNO, using satellite gravity data and geological constrains obtained from the literature.

This research provides critical sidenotes on the assumptions made in previous geothermal energy potential modelling work and provides new sediment thickness maps that can be used as either a starting point or as validation for local basin modelling. These results as part of the work done by Geothermal Atlas for Africa project, aim to provide a starting for future geothermal energy exploration studies to be performed in the countries of Africa.

1. Introduction

1.1. LEAP-RE & GAA

This study is conducted as part of the Geothermal Atlas for Africa (GAA) project. The GAA in turn, falls under the umbrella of the Long-term Europe-Africa Partnership for Renewable Energies (LEAP-RE) initiative. This international partnership, between 85 institutions from 33 countries based in the African and European unions, aims to create a long-term collaboration between academic, private and governmental institutions on the topic of renewable energies.

The GAA, as the name suggests, dedicates its attention to the exploration of geothermal energy resources in Africa, with the goal to provide an interactable online atlas that visually shows relevant information on geothermal energy. The GAA consists of different work-packages (WP) that each focus on different aspects of geothermal energy exploration. For example, WP 9.1 focuses on the geoscientific aspect of geothermal energy, WP9.2 on the engineering aspects, WP9.3 on the social sciences, WP9.4 on the development of the online atlas and WP 9.5 and 9.6 focus on research knowledge sharing and project management respectively.

1.2. Internship Hofstra (2022)

This thesis project and the previous internship project (Hofstra, 2022) are part of WP9.1 and WP9.4 of LEAP-RE with the emphasis on WP9.1. Both projects focus specifically on exploring the geothermal potential of sedimentary basins of Africa. The main objective of the internship project was the construction of a new model of the African sedimentary basins by collecting, quality-checking, and integrating existing data from previous basin models, supplemented by data from literature and other data sources. Moreover, several data sets in the new basin model have also been classified based on various data-quality criteria. Another key result of Hofstra (2022), were geothermal energy potential indicator maps, shown in Figure 2. These maps aim to provide a first order analysis of the geothermal potential of the sedimentary basins of Africa based on direct (i.e. temperature, porosity) and indirect (i.e. hydrocarbon exploitation, sediment thickness, sediment age) geothermal indicators.

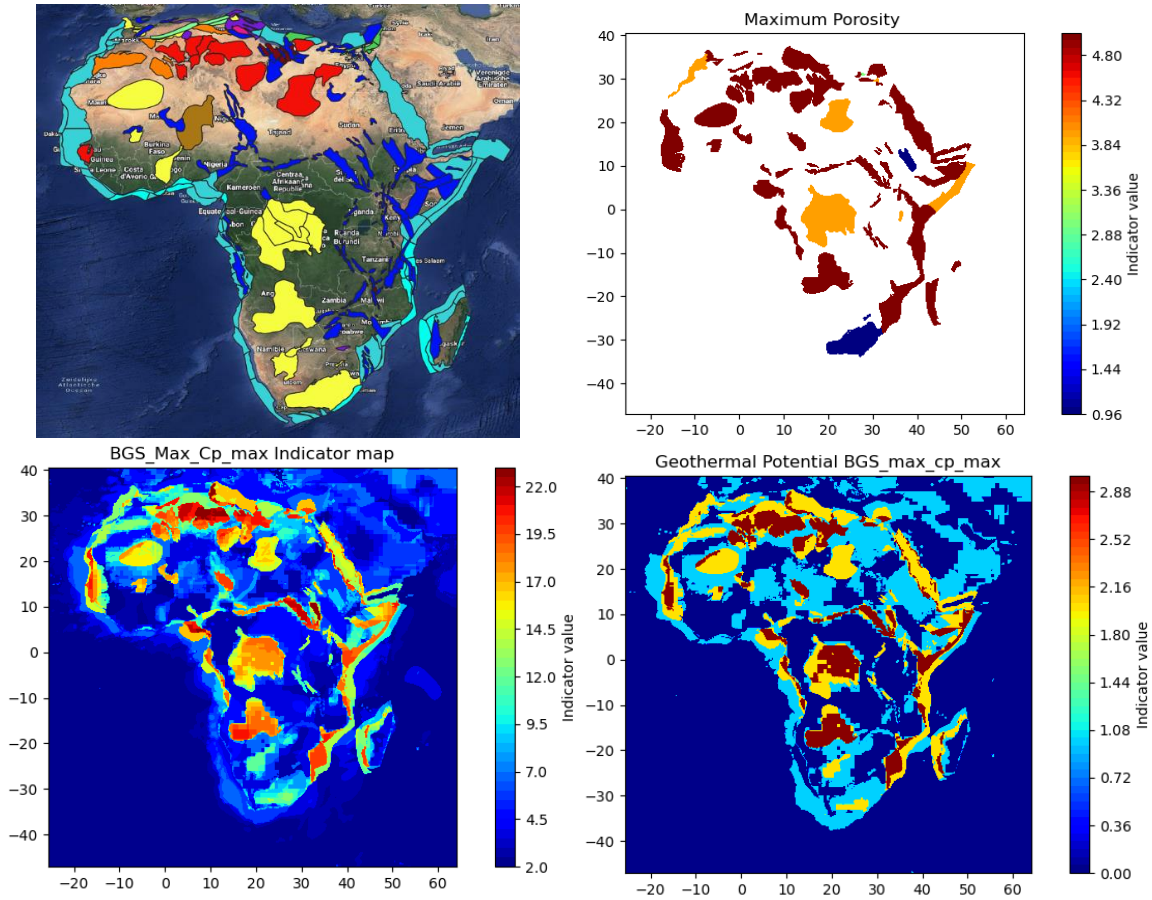

Figure 2: Overview of the indicator analysis results from Hofstra (2023).

1.3. Problem statement

Currently, the highest resolution open access African sediment thickness maps are by Laske & Masters (2013) for the onshore parts of Africa and by Straume et al. (2019) for the offshore parts (Figure 3). The Laske & Masters (2013) data set is the most important for modelling studies of the continental sedimentary basins of Africa. The resolution of the offshore data set is approximately 0.083° x 0.083° and 1° x 1° for the onshore data set, corresponding to distances (i.e., cell or grid sizes) of about ~10 km and ~111km respectively. The resolution of the onshore data set, however, is insufficient for detailed geothermal energy potential modelling and analysis. Higher resolution sediment thickness maps do exist for the African continent but are not freely accessible as they are locked behind paywalls of private companies (i.e. Exploration Fabric of Africa® (EFA), 2020; Getech Group plc®, 2023).

Of the few geothermal energy modelling studies that consider porosity, the majority that covers multiple or individual basins (e.g. Limberger et al., 2018; Barkaoui et al., 2014) generally assume uniform basin/reservoir properties. However, each basin is its own entity/system, especially in a relatively old/stable continent as Africa. Whilst it is possible that multiple basins (located in relatively close proximity to each other) (Basins in Algeria, Egypt, West & Central rift basins and basins in the Horn of Africa) have experienced similar geologic evolutions, it is not unlikely that there are (significant) differences between their respective evolutions. This raises the question if assumptions made on reservoir characteristics in geothermal/basin modelling are based correctly and accurately on the currently available data?

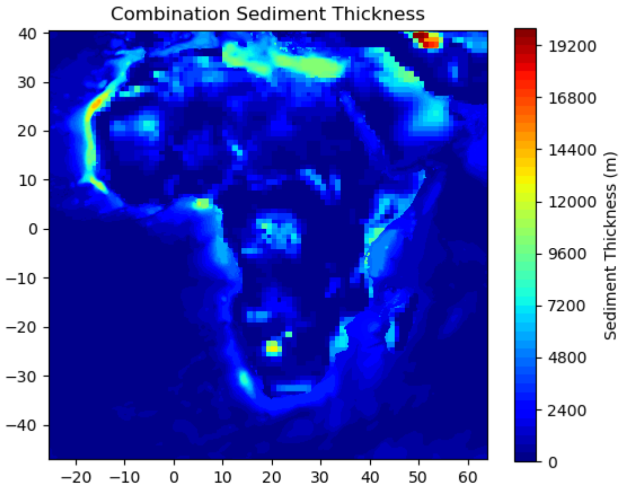

Figure 3: Highest resolution publicly available sediment thickness map composed of onshore data from Laske & Masters (2013) and offshore data from Straume et al. (2019).

1.4. Status quo, geothermal energy in Africa

While instances of geothermal energy for direct heat use date back several thousand years ago (Stober et al., 2013), dedicated efforts of harnessing the heat of the earth have only been in development since the early 1900's (Stober et al., 2013). However, these developments were generally focused on high enthalpy systems. Dedicated publications on low enthalpy geothermal system developments for direct heat use and/or electricity generation only exist from the recent decades starting in the 1970's (e.g. Balling, 1978; Lejeune et al., 1981; Rybach & Jaffe, 1981 Majorowicz et al., 1985). These early publications generally cover only locations in the western world. In Africa, interest in geothermal energy exploitation is not new (Dickson & Fanelli, 1988), but the emphasis on low enthalpy geothermal energy only came about in the past decades.

The geothermal energy potential of the African continent can be considered undeveloped given that only a small percentage of the total renewable energy of Africa is of geothermal origin (IRENA and AfDB, 2022; IEA, 2019). Hence the incorporation of the GAA into the LEAP-RE project. Therefore, a key question that remains to be adequately answered is the following. Which areas/sedimentary basins (outside of the East-African rift valley) are suitable for geothermal energy exploitation and how large, in terms of energy and/or monetary value, is the geothermal energy potential of said places?

Presently, geothermal energy exploitation in Africa is limited to the high enthalpy systems of the East African rift valley (IRENA and AfDB, 2022). As mentioned in IRENA and AfDB (2022), only Kenya and Ethiopia are currently operating geothermal power plants. Other countries in the East African Rift Valley, like Eritrea, Djibouti, Uganda and Tanzania have only recently started with plans to create geothermal energy exploitation capacity (IEA, 2019). Other countries, including but not limited to Algeria, Kenya, South-Africa Tanzania, Egypt, (e.g. Lebbihiat et al., 2021; Lashin, 2020; Kombe & Muguthu, 2019; Dhansay et al., 2017), are exploring the potential of low enthalpy geothermal energy targets/reservoirs. However, as with the majority of the data originating from Africa, the differences between the extent and quality of these efforts vary greatly.

Additionally, only a few studies combine information about reservoir characteristics (porosity, permeability, transmissivity) with data about the thermal energy present in the subsurface. Concluding that the sub-surface contains sufficient heat is an important step in geothermal exploration, however, on its own, it is insufficient to determine the geothermal potential at a given location, specifically in sedimentary basins. Thus, much work still needs to be done in determining the geothermal energy potential of the sedimentary basins of Africa.

1.5. Scientific importance

According to (Ritchie et al., 2023; United Nations, 2022; IEA, 2019), the population of Africa is expected to grow significantly in the coming years (Figure 4,5). The economic development expressed in gross domestic product (GDP), shown in Figure 6 right, also shows a similar trajectory (IEA, 2019). Consequently, due to the economic development of African countries the living standards of the population are also expected to increase (IEA, 2019). This development is often paired with significant increases in energy needs per household, but more significantly is the development of industry which puts an arguably higher strain on the energy budget of a country. The expected growth of the total primary energy demand in Africa for the coming years (Figure 6, Left), visualises this issue.

The economic growth of the countries in Africa is therefore expected to pose a challenge in terms of energy needs. This is a complex endeavour but paired with the goal of the reduction of carbon dioxide emissions as discussed in the Paris climate agreement (United Nations, 2018), the challenge becomes even more difficult. Therefore, it is important to explore all potential sources of renewable energy to reduce the current and potential future emissions of CO2 resulting of the use of fossil fuels. Geothermal energy as renewable energy source, should therefore not be neglected in these endeavours.

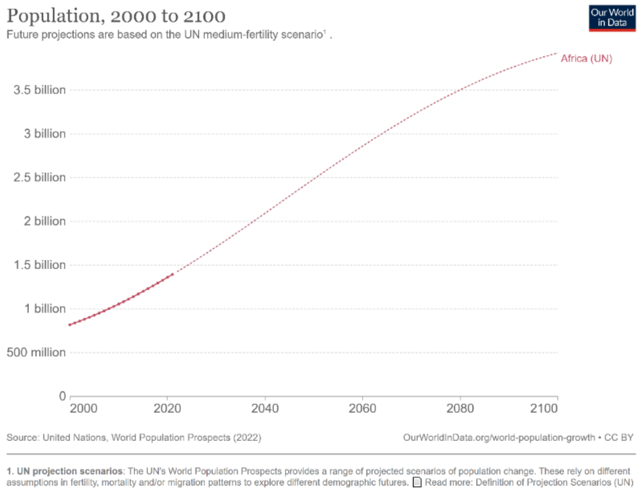

Figure 4: Projected population growth until 2100 for the African continent based on United Nations medium fertility scenario (2022).

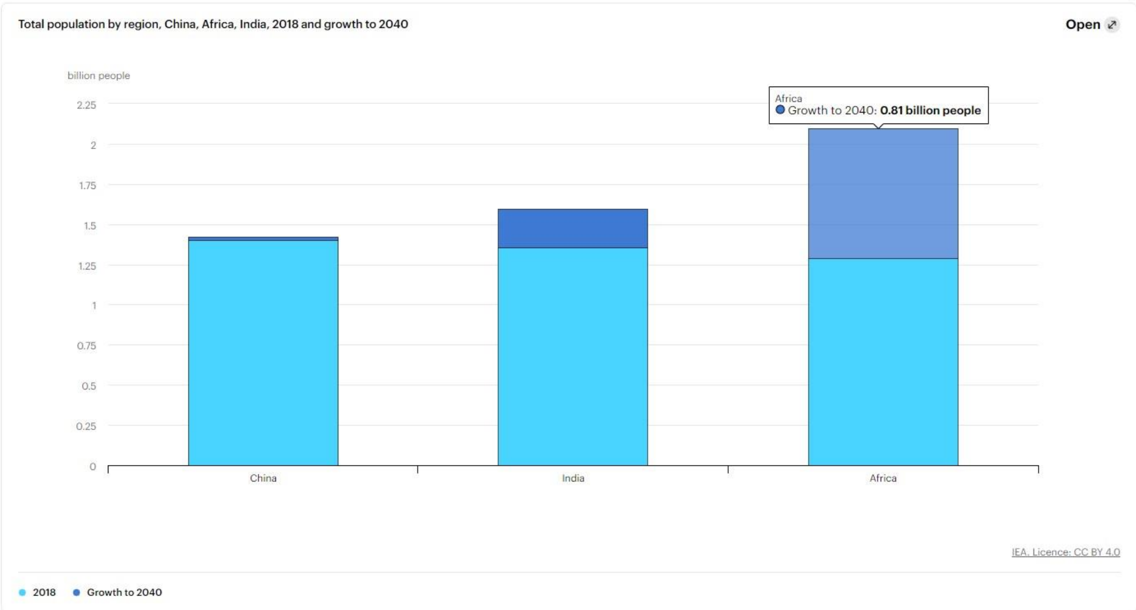

Figure 5: Population growth of China, India and Africa (left to right) from 2018 to 2040, IEA (2019).

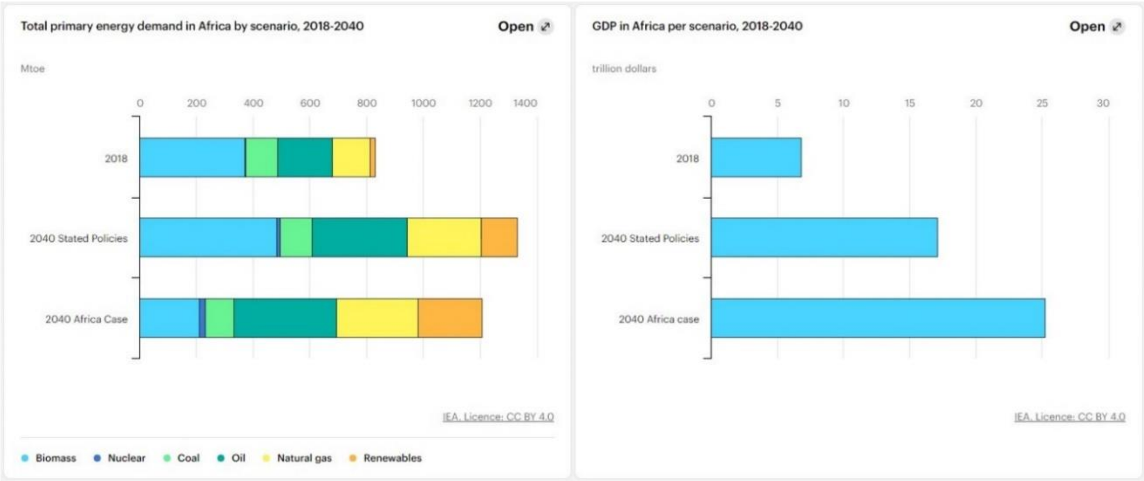

Figure 6: Expected total primary energy demand for Africa on the left and the GDP in Africa per scenario from 2018-2040 on the right, IEA (2019).

Additionally, the search for renewable energy sources and the development of renewable energy technologies are not a challenge unique to the African continent. Progress in these developments in Africa is likely to also produce transferable knowledge that can be used in geothermal energy exploration and exploitation elsewhere.

The academic reasons for conducting this sort of research are multi-faceted. For example, creating a higher resolution sedimentary thickness map of the sedimentary basins of Africa in the public domain can be beneficial for future basin, reservoir and geothermal potential modelling endeavours. Sediment-basement depth modelling can be important for more applications other than geothermal energy potential specifically reservoir modelling (hydrogen storage, aquiver/groundwater modelling, hydrocarbon industry, mineral resource exploration, etc.).

Moreover, gaining (preliminary) insight in the geothermal energy potential of Africa, specifically the low enthalpy systems (sedimentary basins), is important for de-risking and evaluating the geothermal energy potential of African countries. The results can subsequently be used to determine the feasibility of financially sustainable geothermal energy exploitation for direct heat use and/or electricity generation.

Lastly, this research can be used to evaluate the accuracy/usability of an indicator analysis approach as conducted by Hofstra (2022), to determine geothermal potential of a study area. If proven useful, a first-order geothermal energy potential estimate can be determined based on a few direct and indirect parameters.

1.6. Aims & deliverables

The main goal of the GAA project is to determine the geothermal energy potential of the sedimentary basins of Africa. More specifically, which areas of Africa appear to be suitable for geothermal energy exploration (direct heat use and/or electricity generation) and warrant further research. The future aim is to express the geothermal energy potential in terms of energy or monetary value (LCOE). Unfortunately, due to time constrains this aim is not in the scope of this research. These results can subsequently be used to evaluate the results and workflow of the indicator analysis of Hofstra (2022). The end goal is to visualize these results in digital maps which subsequently will be uploaded to the online Geothermal Atlas for Africa.

In order to achieve the goal for the GAA as described above, two goals are defined as the aims for this thesis project. The first objective is to further develop and improve the new basin model created during the internship project (Hofstra, 2022), by expanding the data-quality based classification and by incorporating more precise, observation-based porosity-depth measurements for the sedimentary basins of Africa. This improved model is important for constraining important geothermal parameters required for basin modelling. The result will be an updated basin/reservoir characteristics database of Hofstra (2022), with more accurate parameters describing the porosity-depth relationships for reservoir rocks per basin. These relationships can be described by parameters which subsequently can be expressed spatially to produce digital maps that predict areas with burial anomalies.

With this data, we aim to evaluate if/or how much the publicly available porosity-depth data of Africa supports the assumptions made in continental scale basin/reservoir modelling (Limberger et al., 2018). We particularly aim to determine how accurate it is to assume identical reservoir parameters for the different sedimentary basins in Africa?

The second objective is to conduct a numerical modelling study, using the (reservoir characteristics) data from the new basin model, to improve the resolution of current estimates of the basement depth of sedimentary basins in Africa by Laske & Masters (2013) and to create a geothermal potential map for the geothermal potential of the sedimentary basins of Africa. Basement depth data is important as it and the directly related sediment thickness are first-order input parameters in the assessment of the geothermal energy potential of sedimentary basins. The numerical modelling will first involve gravity inversion followed by geothermal energy potential modelling to create a digital geothermal energy potential map and an improved sediment thickness map. Due to time constrains, the temperature and geothermal potential modelling will be performed by colleagues from TNO.

2. Methods, Software and Data

2.1. GAA & Project workflow

As mentioned in the introduction, the thesis is an extension/addition to the work of Hofstra (2022). Both studies cover parts of the geoscientific approach for the GAA as defined by TNO and Utrecht University (UU) (Figure 7). The emphasis of the work of Hofstra (2022) was on the data complication, data quality checking, reservoir characteristics database, data management and Indicator analysis. The focus of this thesis is on improving and adding on to the reservoir characteristics database and on performing numerical analysis, via gravity inversion. These results are subsequent used for the geothermal energy potential modelling, performed by the colleagues of TNO. The workflow of this thesis project is shown in Figure 8.

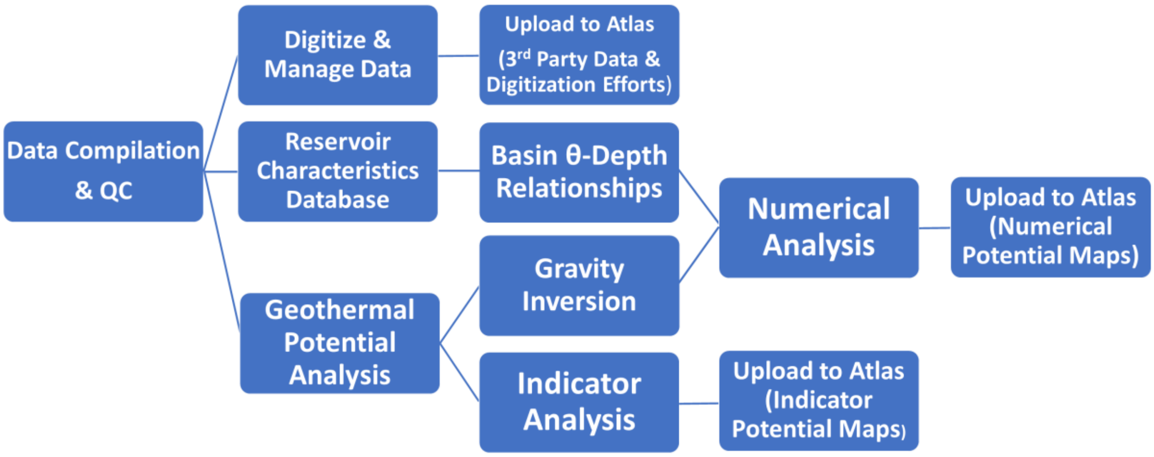

Figure 7: Geoscientific workflow for the Geothermal Atlas for Africa for UU & TNO.

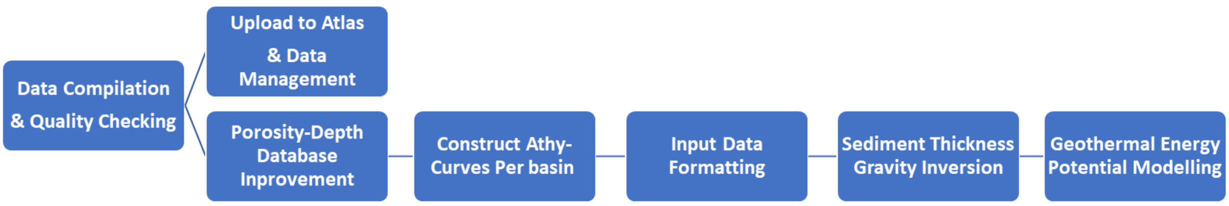

Figure 8: More specific workflow for this MSc thesis project as part of the larger GAA workflow.

In addition to the data compiled by Hofstra (2022), more data is compiled during this thesis. Examples of the compiled data include satellite data on gravity and magnetic, surface temperature measurements, crust and mantle depths and additional Porosity-depth measurement data. The data is carefully evaluated to determine its use in the context of this MSc thesis and the overall GAA project.

2.2. Porosity-Depth

2.2.1. Data compilation

The porosity-depth data, compiled by Hofstra (2022) and additional data compiled during this thesis, are re-examined to determine true porosity-depth measurements rather than averaged values per reservoir. The raw data is directly extracted from the literature and is stored in a excel database following the information protocol shown in table (1).

The data occurs in one of three different forms, each of which has a specific workflow for extraction of the data. The porosity-depth data listed in a table format will directly be incorporated into the database. The porosity-depth data mentioned in the text of the paper is directly incorporated in the database if both the porosity and depth values are given explicitly. If only the porosity value is mentioned, the corresponding depth is estimated from the figure. The porosity-depth data shown in figures (i.e. well logs or porosity-depth trends) is manually estimated using the Plot Digitizer open-source software (www.sourceforge.net/projects/plotdigitizer.com). When both effective and total porosity values are available (i.e. Makled et al., 2022; Sarhan, 2020), the total porosity values are chosen. Also, when maximum, minimum and average/mean porosity values are presented (i.e. Klett, 2000), the average/mean value is chosen.

Parameter Name	Parameter Description
Basin	Basin name
Well	Well name of which the measurement originates
Age_period	Age period of the measurement
Age_extra	More detailed age information if available (Epoch, Age)
Lithology	Lithology of rock the measurement originates (Carbonate, Clastic, Mixed)
Depth	Depth of measurement (m)
Porosity	Porosity value (%)
Phi0	Estimated surface porosity (%), Athy curve
Phibase	Estimated base porosity (%), Athy curve
K	Estimated compaction parameter (-), Athy curve
Ref	Literature reference from which the measurement is taken
Source	Form of porosity-depth measurement (Table, Figure, Paper)

Tabel 1: Description of the parameters included in the improved porosity-depth database.

2.2.2 Porosity-depth relationships

The compiled porosity-depth data will subsequently be separated by age, lithology and basin. Per basin, a porosity-depth Athy-curve (Athy, 1930) will be constructed that best fits the data. Note that the measurements from carbonate reservoirs are excluded in the fitting of the data; see the Discussion for a detailed explanation.

The relationship between burial depth, porosity, bulk volume, density and compaction for sedimentary rocks are experimentally derived by Athy (1930). The relationship shown in Equation 1, is the result of these experiments. The formula describes how the porosity (of clastic rock) changes with depth due to mechanical compaction.

$$\textbf{Equation 1:}\ \theta = \theta_0 * e^{-k_{athy}*(Z)}$$

Where θ is the porosity at depth z (unitless), θ_0 is the surface porosity (unitless), k_{athy} is the porosity-depth decay factor for a specific rock type (unitless), Z is the depth (m). This formula can also be expressed in terms of z-scale as shown in Equation 2. Note that when a burial anomaly is present (more compaction than expected at depth), depth Z is expressed as $Z = Z_{Depth} + Z_{burial}$, where Z_{burial} is the extra burial depth (m).

$$\textbf{Equation 2:}\ \theta = \theta_0 * e^{\left(\frac{-Z}{Z_{scale}}\right)}$$

For a given depth range, Athy-curves are described by any combination of two of the following three (Athy) parameters: surface porosity, porosity-depth decay factor and the porosity at the base of the curve. These three parameters are incorporated into the porosity-depth database in the format listed in Table (1). The Athy-curve that fits best through all the data of the sedimentary basin of Africa is assumed to be the default curve. Its respective Athy parameters are used as the default values for the basins that lack sufficient (publicly available) Porosity-depth data. The porosity-depth decay factor can also be expressed as a term called z-scale. The z-scale indicates the depth (in meters) at which the surface porosity is reduced to a factor of 1/e. The porosity value at this depth is called the base porosity. The z-scale can be derived from the decay factor by dividing 1000 by the decay factor. This conversion is necessary as the inversion software (Basin3D) requires the z-scale as input parameter rather than base porosity.

As mentioned in Evenick (2021) and Hofstra (2022), the definition, name and extend of the sedimentary basins of Africa are not uniformly agreed upon. Therefore, it is important to mention how to data linked to a specific basin (name) is represented spatially. To link this data to basin models, we use the nomenclature hierarchy as established by Hofstra (2022). This nomenclature hierarchy is also used to extrapolate data originating from a "sub-basin" to a "main-basin" and link data originating from a "main-basin" to their respective "sub-basins".

Here we project the three basin specific Athy parameters onto the basin model shapefile of Evenick (2021) to create three Athy parameter grids. This grid data is subsequently extrapolated outwards to populate the data onto Africa. These grids are later used as direct input parameters for the gravity inversion 3d basin modelling.

2.3. Numerical Modelling

2.3.1. Forward VS Inversion modelling

Most of the subsurface knowledge is based on indirect measurements (seismic, gravity, extrapolations from outcrops) that are calibrated by significantly fewer direct measurements (i.e. drill cores). However, each of the different data types has their own limitations. In the case of gravity specifically, the gravity (anomaly) measured can be explained by an infinite number of combinations of varying layer geometry and rock parameters. This non-uniqueness problem can be minimized by applying geological evidence based constrains. This, in essence, is the concept of geological modelling using gravity (anomaly) measurements.

The goal of gravity modelling is to create a geological model that best explains the observed gravity (anomaly) signals measured at the Earth's surface or at a given height (measured by satellites), by applying geological constrains. The sub-surface parameters of interest (i.e. density, layer geometry) can be derived by comparing gravity observations with the gravity response of a prior model (Blakely, 1996). This can either be done via forward or inversion modelling.

In the forward modelling approach, starting from a prior model, the modelled/computed gravity response is matched with observed gravity measurements by manually changing geologically relevant parameters as density and layer geometry and rock properties. However, in more complex areas or locations where the data density is insufficient for providing geological constrains, this approach might be difficult to produce reliable results. In these instances, inversion modelling can provide a solution.

In an inversion modelling approach, model parameters are also iteratively changed starting from a prior model to better match the model values with the observations. However, as opposed to forward modelling, the iterative changes are automatized and performed by an algorithm using for example, data assimilation methods (i.e. Riechle, 2008).

To create a geological model using data assimilation methods, constrains on the variable parameters are needed. For the data assimilation, three things need to be specified 1) the variable parameters, 2) the allowed variation range, 3) the part of the model (layers) affected by the data assimilation. During the data assimilation, modelled and observed gravity values are compared. When there is a discrepancy between these values after the consideration of the respective uncertainties, the selected parameters are changed (within the imposed range) to minimise the difference between observed and modelled values.

2.3.2. Basin 3D software

For the gravity inversion we use the TNO in-house developed software Basin3D (TNO AGS). Basin3D is a numerical modelling software implemented in JAVA, based on the work done by Tontini et al. (2009) and Cooley and Tukey (1965). This forward and inversion modelling software is elaborately described and benchmarked in the MSc thesis paper of Sejan (2018). However, these tests and descriptions might be partly outdated due to the developments made on the software during this project.

2.3.3. Gravity geophysics

It is beyond the scope of this thesis to re-derive the gravity formulas used in inversion modelling, but we will attempt to briefly describe the concepts of gravity in geosciences that are used in the Basin3D software.

Newton's law of gravitation, shown in Equation 3, describes the force that acts between two point masses.

Equation 3: $$F_g = G * \frac{m_1 * m_2}{r^2}$$

Where F_g is the force of gravity in Newton, G is the gravitational constant 6.67*10^-11 Nm^2/kg^2, m1 & m2 are the masses of the two objects in kg and r is the distance between the two objects in meters.

Because of these gravitational forces caused by the mass of the earth, objects on the earth's surface remain grounded. In a geological context, this means that the geological layers of the earth each contribute to the mass of the earth and thus exert a gravitational pull on objects on the surface (and above). The contribution of each geological layer to the total gravitational signal of the earth largely depends on their respective density and geometry.

If we assume that the earth is a perfect sphere with geological layers at predetermined depths with homogeneous densities, we can determine an average gravity for a given depth. However, by measuring the gravitational pull at different locations at the earth, we observe that there are gravity anomalies in the gravity measurements. This very much expected given that this spherical earth assumption is not supported by geological observations.

In order to explain the measurement gravity anomalies, we have to assume lateral (along a given radius from the earth's core) density differences in the earth due to the geology in the subsurface. Given that the force of gravity is proportional to the distance between objects squared, deeper geological structures (sources of density contrasts) have an overall smaller contribution in the gravitational signal compared to shallower geological structures. However, these deeper sources also effect a larger area compared to the shallower structures. This difference in contribution in the gravity signal is often expressed in terms of long- and short-wavelength contributions, where larger/deeper structures have a longer wavelength contribution (regional trends) compared to shallower/smaller short wavelength contributions (residual trends). By filtering out the long-wavelength contribution of the gravity signal, it is theoretically possible to describe the observed gravity anomalies by lateral density differences in crustal and shallow geological structures.

However, as the gravity measured at the earth's surface is composed of all of the gravity components of the individual geological layers and given that the geology of certain regions can be complex, it is difficult to attribute a gravity anomaly to a single geological feature. Additionally, it is possible that a smaller high density body at a deeper depth, has the same gravity contribution as a larger low-medium density body located at a shallower depth (Figure 9). Therefore, when modelling the subsurface with the use of gravity (and magnetic) anomalies, the derived solution is not unique due to the infinite amount of geological configurations that can be used to explain the observed gravity anomaly. For this reason, it is important to constrain the geological configurations by other data types and sources like for example well-logs, seismic and in field observations.

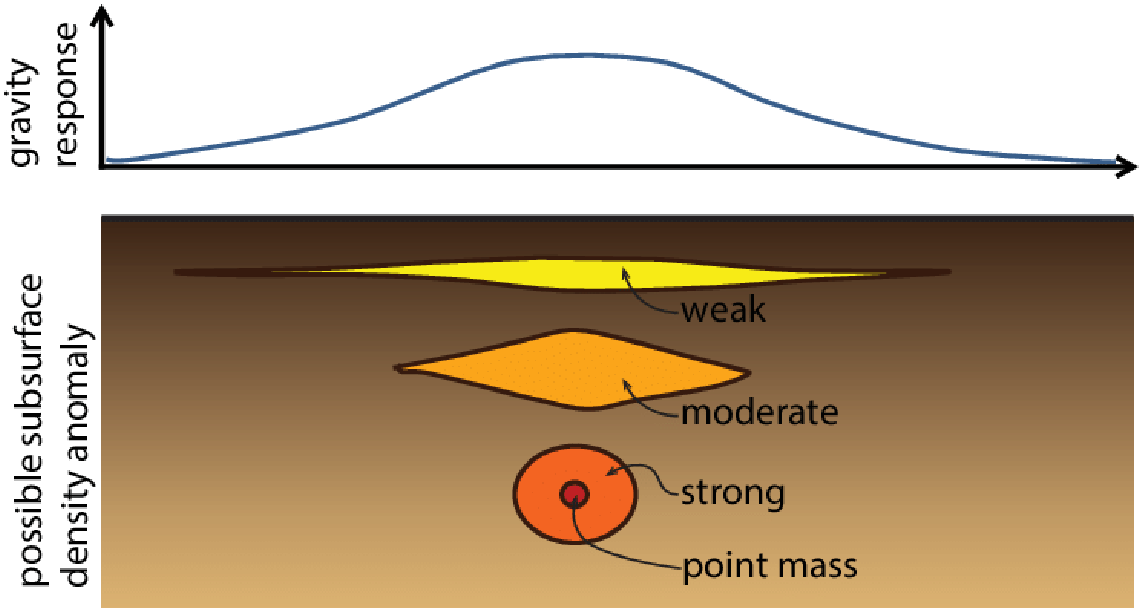

Figure 9: Sketch taken from PHD Thesis Blom (2018), illustrating potential gravity sources that could explain a given gravity anomaly.

2.3.4. Fourier domain

Similar to the comments made in the gravity section above, it is beyond the scope of this thesis to re-derive how these gravity potential fields can be described in the Fourier/frequency domain. For an elaborate derivation of how the Fourier domain can be used in modelling of potential fields (gravity and magnetic fields) look at the work of Bhattacharyya (1967). One of the main benefits of calculating the gravity field potential in the Fourier domain is that due to the relatively simple form of the description of the potential field, the computation time is significantly reduced compared to traditional modelling in the spatial domain (Den Hollander, TNO report).

2.3.5. Data assimilation

The Basin3D software uses the ensembles smoother with multiple data assimilation method described by Emerick and Reynolds (2013). This method is an extension of the Kalman filter which is generally used for solving non-linear problems (Evensen, 1994). As stated in the TNO report of Den Hollander, the ensemble smoother method is not considered a 'true' inversion method comparable to least-square approaches. However, Iglesias et al. (2013) showed that the accuracy of this method is comparable to the accuracy of least-square approaches.

2.3.6. Detailed gravity inversion workflow

The Basin3D gravity inversion modelling workflow is composed of subsequent steps as shown in Figure 10.

The first step is the construction and pre-processing of a realistic a priori (initial) geological layer model, in which the rock properties, geometry and extend of said layers are defined. This prior model is used as input for the gravity inversion modelling using data assimilation. The result of the gravity inversion is a voxet file that can be used in subsequent gravity inversion calculations as prior model input. Thus, the gravity inversion can be repeated by using the results of the previous inversion and by changing data assimilation settings to produce different/higher resolution results.

For our gravity inversion numerical analysis, data from the new African basin model is used to construct priori initial 3D models of basin geometries (including basement depth). Surface gravity anomalies derived from these models are compared with satellite gravity anomaly data. Using an inversion procedure, the basement depth, (porosity-controlled) density of the sediments and the upper-crustal densities are varied iteratively until the difference between predicted and observed anomalies has been minimized. The reason for only varying the upper-crustal density rather than the other deep earth layers is discussed in the Discussion section.

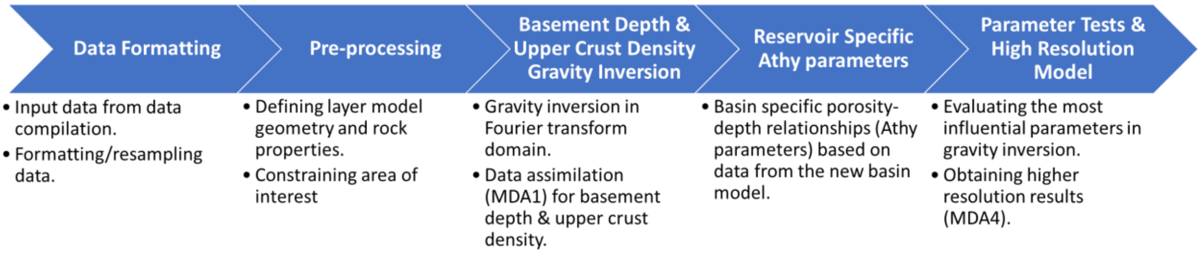

Figure 10: Detailed Basin3D gravity inversion modelling workflow.

The initial output horizontal grid resolution is chosen to be 25km^2. However, if the computational limitations allow it, this resolution is increased to 12.5km^2.

The initial inversion modelling per sub-area is performed using MDA1 assuming static Athy parameters. For the second run, the Athy parameters as described in the porosity-depth relationship section are used to account reservoir/basin rock variations. This run is used to validate if changing these sediment parameters increases the fit of the model to the gravity observations. The final run uses static Athy parameter inputs and MDA4 to achieve the best fitting results.

The degree of fit between model and observations is evaluated by comparing the differences between the observed satellite gravity measurements with the mean gravity response of the basin model. Additionally, the sediment thickness results are also evaluated on their geological accuracy by comparing them with other published work, particularly geological and seismic cross-sections that were compiled from literature during the internship of Hofstra (2022).

This workflow is performed on different sub-areas of the African continent rather than performing the inversion on continental Africa as a whole. The main reason for this approach is the limited computational power of the hardware used. Other reasons are discussed in the Discussion section.

Each sub-area is defined by a specific basin or group of basins based on the sedimentary thickness map of Laske & Masters (2013). Note that the sub-areas are focused on onshore basins and largely exclude passive margin basins for reasons discussed later. The highest resolution sediment thickness map of each sub-area is incorporated in the highest resolution map available, increasing the resolution at these locations.

2.4. Basin3D input parameters

The following explanation of the input parameters used in Basin3D workflow are meant to illustrate the possibilities of the software with the emphasis on gravity inversion modelling. This description will therefore not be extensive in describing all the software capabilities in detail. For more information, please contact TNO and ask for the Basin3D software manual.

2.4.1. Pre-process module

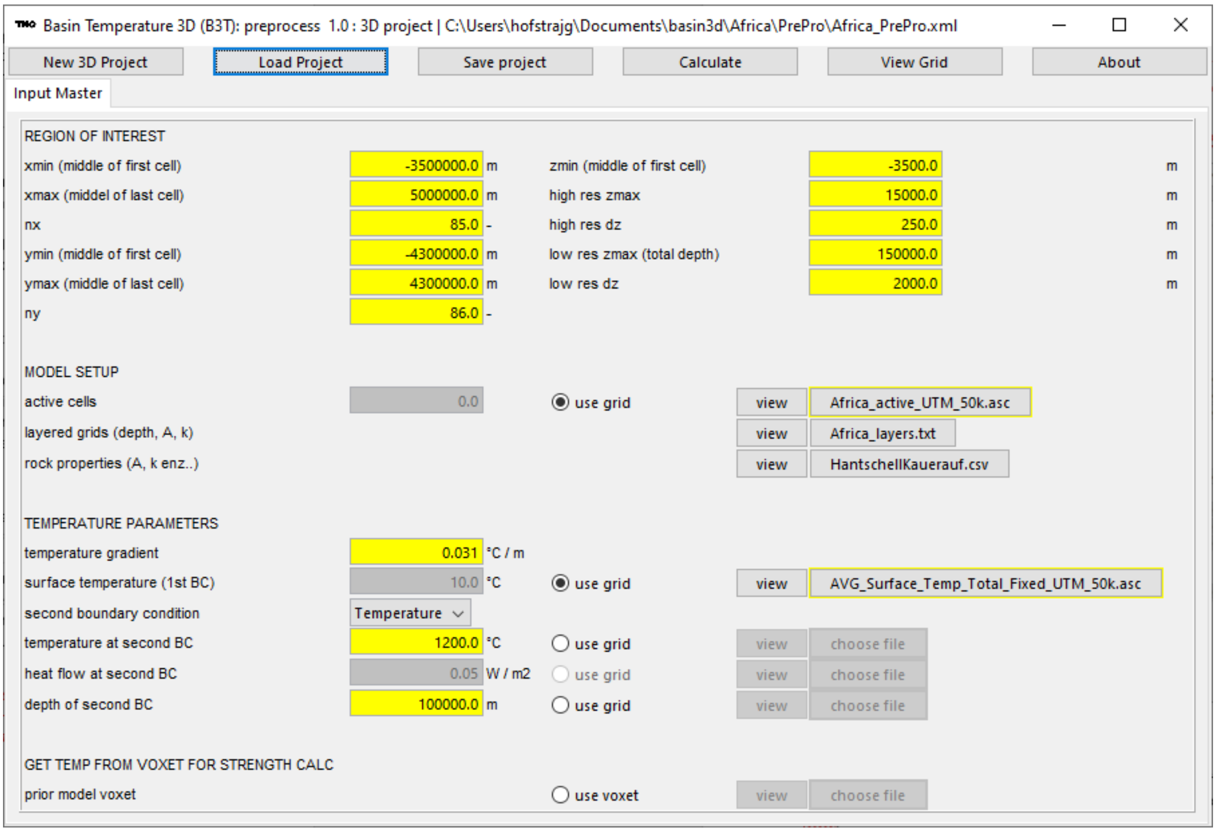

Figure 11: Basin3D Preprocess interface

The interface of the preprocess module is shown in Figure 11.

- Under the “region of interest” section the spatial extend of your model in both the horizontal (x,y) and the vertical/depth direction (z) is determined. The depth direction is divided into a high-resolution upper part and a lower resolution lower part of the model. This is because the gravitational response of deeper structures is generally expressed in large-wavelength (regional) signals which are less important for the shallower structure/basin modelling done in this project.

- The region of interest inputs are specific to each sub-area, however, the number of horizontal grid points nx and ny are chosen such that the maximum grid size is 25km^2 or less (preferably 12.5km^2) if the computational time remains acceptable. The input parameters in the z direction (with z positive downwards) are identical for each of the sub area. The upper boundary of the model is located at -3500 meter above to surface to accommodate for the free-air gravity anomaly observations that are transposed to this altitude. The high-resolution part of the model has a dz of 250 meter and extends from the upper boundary down until a depth of 15km. The low-resolution part of the model, with a dz of 1500 meters, extends from this depth to the base of the model at a depth of 150km.

- The active cell grid, also specific to a given sub area, has generally the same size and extend as the region of interest for areas located exclusively on the continent. For regions of interest covering off-shore areas, the active area grid only covers parts of the offshore passive-margin basin.

- Both the layered-grids file and the rock-properties file are identical for all sub-area models. However, due to an absence of sediment thickness measurements in the maps of Laske & Masters (2013) in the SE Africa rift basin region, an average sediment thickness of 2km is assumed and projected onto the basin outlines defined by Evenick (2022).
- The individual layers and their geological properties are listed from deepest to shallowest in the layers grid file (Table 2). Each layer and its properties are defined spatially by its lower boundary.

TIME(Ma)	Grid-TVD/Thickness(m)	Elevation/TVD/Thickness	Active kzmix (standard kz)	Layer-k	Layer-A[muW/m3]/burial anom[m]	shrink [m]	extrapolate [m]	V0k: k-value [1/s]	V0k: V0-value [m/s]
-3	110000	TVD	☐	100_KmLM	0.03	0	20000	77	3320
-2	Moho_Finger_2022_UTM_50km_fixed.asc	TVD	☐	100_KmLC	0.3	0	20000	77	2940
-1	UC_Finger_2022_UTM_50km.asc	TVD	☐	100_KmUC	1	0	20000	77	2700
3	Africa_S_Thick_Combi_UTM_50k.asc	Thickness	☐	50_CSSandTyp_50_CSShaleTyp	Top2sur_UTM_50km.asc	0	20000	77	2700
2	Africa_ETOPO1_UTM_50k.asc	Elevation	☐	1000	0	0	20000	77	1030
1	Africa_surface_UTM_50k.asc	Elevation	☐	1000	0	0	20000	77	0
0	-4000	Elevation	☐	0	0	0	20000	77	0

Tabel 2: Basin3D layer model interface, excluding scale factor columns to enhance readability.

  - The “Time (Ma)” column conventionally lists the ages of the specific layers in Ma. The mantle and crustal layers are an exception as the negative numbers in ascending order indicate the lower mantle, lower crust and upper crust boundaries respectively. These layers are followed by stratigraphically shallower layers with positive descending indices capped off by the top layer with the index “0”. Note, that as our model contains one sedimentary thickness layer with an unspecified age, we choose to fill this column with the index of the layers rather than age. This approach has no effect on the gravity inversion modelling we perform, as it considers only the present-day basin structures, densities and porosities.

  - In the “Grid-TVD/Thickness(m)” column the depth of the boundary is specified by a value or by a grid file. The “Elevation/TVD/Thickness” column, indicates if the value in the previous column indicates an elevation, a true vertical depth (TVD) or a thickness.

  - The “Active kzmix (standard kz)” column dictates if the thermal conductivity in the z-direction is calculated as a mix of lithologies. In the “Layer-k” column, the thermal conductivity of the layer is determined by either the lithology fraction per layer (e.g. 60% sandstone, 40% shale) or by providing thermal conductivity values. In the case of the former, the lithological fraction is used to determine the thermal conductivity value from the chosen rock-property database file. This software is developed with the rock-property database of Hantschel & Kauerauf (2009) in mind, we therefore use their work in this analysis.

  - The next column, “Layer-A[muW/m^2]/burial anom[m]”, either specifies a radiogenic heat production or a burial anomaly for a specific layer. The former requires a value whereas the latter requires a dedicated grid file. By inserting the value “0” the heat production is determined using the rock property database.

  - The “shrink” and “extrapolate” columns are used to impose either a shrinking or an extrapolation of the input grids. The shrink function can be used to exclude edge effects whereas the extrapolate column is used to fill gaps in the input grids. In our modelling, we extrapolate each of the layers by 20 kilometres.

- The next two columns, “V0k: k-value[1/s]” and “V0-value [m/s]”, are used to specify layer densities. For column 9, the value is 77 indicates that the value specified in column 10 is a direct density value. For a value of 99 in column 9, the density is determined by the mechanical compaction with depth for a given lithology described in Hantschel & Kauerauf (2009). Here we choose to model using direct initial densities per layer.
- The last two columns are used to scale the thermal conductivity and radiogenic heat production respectively, but these options are not used for the gravity inversion modelling.

The layer model shown in Table 2, is used for all sub area models.

- The lithospheric mantle lower boundary is set to a depth of 110km. For the lithospheric mantle a heat production of 0.03 muW/m^3 and a density of 3320 kg/m^3 are adopted.
- For the Moho depth/(lower) crustal boundary the results of Finger et al. (2022) are used with a heat production of 0.3 muW/m^3 and a density of 2940 kg/m^3.
- The upper-lower crust boundary is defined by dividing the Moho depth from Finger et al. (2022) in half and has a heat production of 1 muW/m^3 and an initial density of 2700 kg/m^3.
- The initial sediment thickness is defined by the numerical modelling results of Laske & Masters (2013) on the continents and the results of Straume et al. (2019) for the offshore area. The sedimentary layers are merged into one layer due to limitations in software and data availability. The sediments are assumed to be composed of an equal mixture of “typical sandstone” and “typical shale” as defined by Hantschel & Kauerauf (2009). This lithological composition also determines the thermal conductivity of this layer. The sediments are assumed to have an initial bulk density of 2600 kg/m^3, which is between the values listed for sandstones and shales in Hantschel & Kauerauf (2009). To properly model the effects of mechanical compaction on sediments, a “burial anomaly” map that describes the distance from the top of the model to the level of the topography/bathymetry is required.
- The topography-bathymetry boundary, described in the next row, is based on the ETOPO1 model (NOAA, 2022). The properties of this layer describe the properties of seawater with a density of 1030 kg/m^3.
- The next layer describes the water surface (0 meters altitude) and the continental topography. The density of air, described in this row, is assumed to be 0 kg/m^3. For both the ocean water and the air, a high thermal conductivity of 1000 W/(m.K) is assumed to disregard the thermal conductivity contribution of these layers.
- The last layer indicates the upper boundary of the model at the height of 4000 meters. This height is chosen to account for the topography in the free-air gravity anomaly used in the gravity modelling. Note that the highest point in Africa, Kilimanjaro (5895 m) exceeds the upper limit of the model. However, due to the resolution of 50 km^2 of the input maps/grids, the highest altitude averages out below 4000 meters. The properties listed for this last layer have no effect on the modelling calculation, as they describe the layer above the upper boundary of the model.

- The temperature parameters are of lesser importance for the gravity inversion modelling and are therefore not changed for all models. The surface temperature grid used is the average annual surface temperature measured by NASA over the year 2022 (NEO/NASA, 2022).

2.4.2. Gravity Inversion module

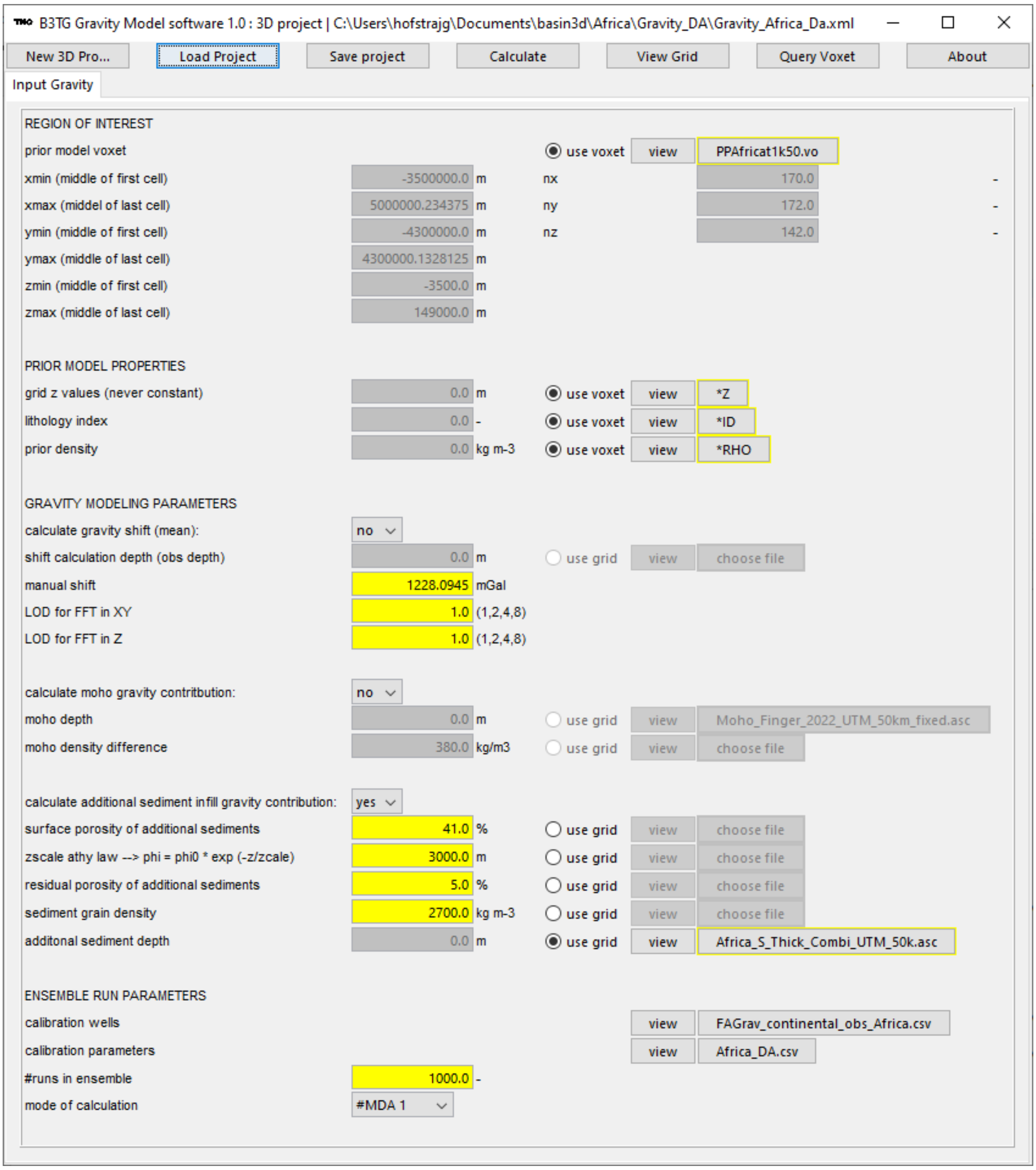

Figure 12: Basin3D gravity inversion interface.

The gravity inversion module interface is shown in Figure 12.

- Prior model

The first section of the gravity module is identical to the preprocess module. However, here the prior model voxet can be loaded to specify the inputs for the "region of interest" and the "prior model properties". It is self-explanatory that this input voxet is dependent on the sub-area in question.

- Gravity modelling

Under "gravity modelling parameters", the gravity shift, the LOD for the Fourier domain in the horizontal and the vertical direction, the Moho contribution and the sediment specific density parameters are specified.

- Gravity shift

  A shift in the vertical axis is required to ground/fit the gravity anomaly observations to the model. This shift is a correction to account for the mean gravity effect of the deep earth and to discount biases in density assumption. The best mean shift for the selected region can be calculated by running the gravity inversion module without data assimilation (no DA) by toggling the "calculate gravity shift (mean)" to yes. After the no DA run, the mean gravity shift is displayed in the console of the software. For the subsequent DA modelling, the gravity shift can be entered under "manual shift", after toggling the "calculate gravity shift (mean)" off. For our analysis we will use this method to obtain the main gravity shift per sub-area.

- LOD for FFT in XY & Z

  The "LOD for FFT in XY/Z" can be used to change the ratio between the cell-size in the horizontal and the vertical plane respectively. As the calculation takes place in the Fourier domain, the ratio between the horizontal and vertical direction affects the results of the gravity inversion. If this ratio exceeds 100, the error of the results becomes significant (>5%). In our analysis, we keep the ratio of the LOD parameters to 1:1. For a dz of 250 meters (assumed for all models), we aim to keep the dx/dy below 25km as to not exceed a ratio of 1:100.

- Moho contribution

  The Moho contribution can be calculated by toggling the "calculate Moho gravity contribution" to "yes". In the first two rows you specify the Moho depth and density difference, respectively. We focus on the gravity component of the sedimentary basins of Africa and therefore choose to not calculate the Moho contribution.

- Sediment Parameters

  In the last part of the "Gravity modelling parameters" section, the gravity contribution of the sediments can be specified by toggling the "calculate additional sediment infill gravity contribution" to "yes". Here the porosity-depth relationship for the sediment layer can be constrained by specifying Athy parameters (surface porosity, z-scale and the base porosity).

  For the static Athy parameter modelling we use 41%, 3000m and 0% respectively. For the basins-specific Athy parameter modelling we use the results of the Athy-curve estimation as described in "Porosity-depth" section.

- Sediment grain density

  For the sediment grain density, we assume an average value of 2600 kg/m^3 for all models. This value is 100 kg/m^3 lower than the initial density of the underlying upper crust and is on the low-end for sandstones (Hantschel & Kauerauf, 2009).

- Sediment depth

  Under "Additional sediment depth", the starting sediment-basement interface depth is specified. Here we use the work of Laske & Masters (2013) for all models except for the SE African rift zone. For the SE African rift areas not covered by the model of Laske & Masters (2013) due to the limited resolution, we use a constant sediment depth of 2000 meters, superimposed on the basin model of Evenick (2022) as stating depth.

- Ensemble run parameters

The last section called "ensemble run parameters" covers all input parameters that specify the data assimilation part of the gravity inversion modelling.

- Gravity observations

Under "calibration wells", the gravity observations used to constrain the geological model are specified via a CSV-file. In our analysis, we use the BGI WGM2012 free-air gravity anomaly model (Bonvalot et al. 2012) transposed to a height of 3500 meters. The effect of this translation is calculated via Equations 4 and 5.

$$\textbf{Equation 4: } g_{FA} = g_{obs} - (g_{theoretical} - \delta g_{FA})$$

$$\textbf{Equation 5: } \delta g_{FA} = \frac{2g}{R} * h$$

Where g_{FA} is the free-air gravity anomaly in mGal, g_{obs} is the observed gravity (measurement) in mGal, $g_{theoretical}$ is the theoretical gravity in mGal, δg_{FA} is the free-air correction in mGal/m, g is the gravitational acceleration in m/s^2, R is the radius of the surface of the earth in meters and h is the height to which the free-air gravity anomaly is corrected.

For the gravitational acceleration we use a value of 9.81 m/s^2, for R we assume the radius of the earth of 6.371 * 10^6 m and for h we use a grid that describes the distance from the ETOPO1 elevation model to a height of 3500 metres. Note that the free-air correction is negative given that we are moving away from the centre of the earth.

The CSV-file, an example is shown in Figure 13, requires 6 columns that specify the spatial coordinates (x,y,z coordinates, UTM projection) of the gravity anomaly measurements followed by the (free-air) gravity anomaly in mGal, an error column and a column the measurement name. For the inversion modelling we choose an error of 15 mGal for all measurements.

	A	B	C	D	E	F
1	X(m)	Y(m)	z(m)	property	error	name
2	-3150021	1904598	-3500	66.56	15	obs
3	-3100021	1604598	-3500	25.07	15	obs
4	-3100021	1654598	-3500	24.62	15	obs
5	-3100021	1704598	-3500	31.45	15	obs
6	-3100021	1804598	-3500	20.39	15	obs
7	-3100021	1854598	-3500	13.93	15	obs
8	-3100021	1904598	-3500	33.6	15	obs
9	-3100021	1954598	-3500	36.58	15	obs
10	-3050021	1554598	-3500	3.43	15	obs
11	-3050021	1604598	-3500	17	15	obs
12	-3050021	1654598	-3500	19.38	15	obs

Figure 13: Gravity observation data csv-file sample.

The gravity observations are subsequently clipped to exclude data outside the "active area grid" to reduce the computation demand on the system. Due to reasons discussed in the Discussion section, the final modelling attempt is performed using a more strictly filtered dataset that excludes most of the gravity observations from off-shore Africa.

- Data assimilation parameters

Under "calibration parameters", the variable parameters, their respective variation range and the effected layers are specified in a text-file. The DA-file used in this analysis is shown in Table 3.

- The "Active" column is used to indicate which parameters are used in the gravity inversion modelling.
- The "parameter name" column specifies the parameter to be varied. The next four columns are used to constrain the variation range of the variable parameters. First the minimum and maximum values are specified by either scaling (multiply the initial value with a and b) or by shifting (the initial value from -a to a).
- The "a" and "b" columns specify the upper and lower limit of the range as specified above. The "distribution" column is used to specify if the scale or shift is performed using a triangular or a uniform distribution.

- The ”var range (-1=c)” column is used to specify the spatial correlation of a cell property. This is defined by a variogram following Gaussian distributions. For a constant scale/shift, the value is set to -1. Other values indicate the variogram’s range in the x and y direction.
- The last 3 columns are used to specify which layers are affected by the data assimilation. The last two columns (“k1 & k2”) are used to determine, from and up to, which layer should be affected in the data assimilation, respectively.

During our inversion modelling, we vary both the density of the upper crust and the sediment-basement interface. To filter out long wavelength contributions to the gravity signal, the density of the upper crust is allowed to vary by ± 20% of the initial density value, affecting the surrounding 20 cells. The caveats of this approach are discussed in length in the Discussion section.

The sediment thickness parameters are allowed to decrease by 90% or increase by 100%, affecting the surrounding 5 cells. This allowed range might seem peculiar, however as later established in the Parameter study section, changing the range will not have a large effect on the results.

C:\Users\hofstrajg\Documents\basin3d\Africa\Gravity_DA\Africa_DA.csv

Active	Parameter name	scale or shift	a	b	distribution	var range (-1=c)	useindex(1)	k1	k2
☐	RHO	SCALE	0.8	1.2	TRIANGULAR	5	INDEX	3	4
☑	RHO	SCALE	0.8	1.2	TRIANGULAR	20	INDEX	-1	0
☑	SEDDEPTH	SCALE	0.1	2	TRIANGULAR	5	INDEX	-3	-3

OK CANCEL

Tabel 3: Basin3D data assimilation file.

- Runs in ensemble

The second to last row in the gravity interface determines the amount of runs per ensemble. For the no DA run to determine the gravity shift per sub-area, this value is set to 1. For all other models the runs per ensemble are set to 3000.

- Number of MDA

Under “mode of calculation”, the type of data assimilation used in the inversion modelling is specified. Here we use one of three options, no DA, MDA1 and MDA4. The number stands for the number of ensembles that are ran during the data assimilation after the initiation of the model. As mentioned before, no DA runs are used to forward model and determine the mean gravity shift per prior-model. For the initial and basin specific Athy-curve modelling we use MDA1. The final models are ran using MDA4 to ensure the best fit possible. MDA1 is considered be sufficient for linear problems whereas MDA4 is sufficient for non-linear problems (Emerick & Reynolds, 2013). The respective differences results are described in the Results and Discussion sections.

2.5. Data resolution and formatting

Input Layer	Source	Resolution
Lower Mantle boundary	N/A (Constant Value)	50 x 50 km (Default)
Crust Mantle boundary	Finger et al. (2022)	1° x 1°
UC-LC boundary	Finger et al. (2022) (divided by 2)	1° x 1°
Sediment Thickness	Laske & Masters (2013), Straume et al. (2019)	1° x 1° & 0.083° x 0.083°
Elevation-Bathymetry	NOAA National Centers for Environmental information (2022)	0.0167° x 0.0167°
Water Layer	N/A (Bathymetry to 0 NAP)	0.0167° x 0.0167°
Air Layer	N/A (Constant Value)	50 x 50 km (Default)
Surface Temperature	NASA Earth Observations (NEO) et al. (2022)	0.1° x 0.1°
Gravity Observations	Bonvalot et al. (2012) (BGI WGM2012 FA)	0.0333° x 0.0333°
Athy Parameter Grids	N/A (Raw measurements from different sources)	50 x 50 km (Default)
Active Grid	N/A	50 x 50 km (Default)

Tabel 4: Input data source and resolution.

The input data, used in the gravity modelling are listed in Table (4). Each of the input layers has different resolutions and areal extents. Both the resolution and the extent of the data have significant effect on the computation power required to calculate the sediment thickness by the means of gravity inversion. We therefore, format all input files prior to the inversion modelling to have the same cell size and extend. Additionally, due to software specifications/limitations, the input files require to be (re-)projected using an UTM projection. Here we choose the UTM 33N projection for all input files as this projection best covers the central part of Africa, minimizing the average distortion at the edges of the grid. The justification and associated problems are discussed in the Discussion section. For the initial resolution we choose a cell size of 50 x 50 km.

For data formatting and projecting, we use a combination of the following software: Surfer, a gridding and plotting software (Surfer®, Golden Software, LLC); QGIS, a GIS-based data visualization and projecting tool (QGIS Association, 2023) and PyCharm, a python-based coding tool for data manipulation (JetBrains s.r.o. (2023)). For the latter we mainly use packages as Pandas, Geo-Pandas, NumPy, Matplotlib and other supporting packages.

2.6. Temperature, geothermal potential calculations and the GAA

Key parts of the GAA workflow, not covered in this thesis due to time constrains are the temperature and numerical geothermal potential modelling. This also includes the creation of the online geothermal atlas environment developed by TNO. However, due to their importance to the end product of the GAA project we will briefly mention a simplified workflow for each.

The temperature model of Africa will be created using the temperature modelling functionality of the Basin3D software. This temperature model will be created using the forward modelling utilizing the updated sediment thickness map obtained from the gravity inversion. The results from the porosity-depth relationship analysis in addition to other temperature data will be used to model the temperature in (the sedimentary basins of) Africa.

By combining the temperature model of Africa with the new sedimentary basin model, estimates on the numerical geothermal energy potential can be calculated using the software of ThermoGIS/DoubletCalc (thermogis.nl; nlog.nl). This software, developed by TNO, is also used for the geothermal energy potential calculations of the Dutch subsurface (nlog.nl). For more information about this software, download the instructions listed on the website (nlog.nl/tools).

The new sedimentary thickness, temperature and geothermal energy potential maps of Africa will be uploaded to the online Geothermal Atlas for Africa. Other open sources data compiled and quality checked during this analysis will also be included in the atlas. This online atlas environment developed by TNO, provides an online interactive map viewer experience where all (open source and partner) data relevant to geothermal energy are shown.

3. Results

3.1. Porosity-depth relationships

3.1.1. Porosity-depth data

Figure 14 shows all the (publicly) available porosity-depth data categorized by age for the sedimentary basins of Africa. The left part of the figure shows the porosity-depth data from clastic and mixed reservoirs whereas the right part shows all the data including data from carbonate reservoirs. Here we can observe the following.

- The porosity-depth data of different ages are largely concentrated in point clouds/lines for different depths.
- Most of the porosity measurements range from 0 to 40, with some exceeding 40 to a maximum of 60 percent.
- Generally, the porosity decreases with an increase in depth. The general trend shows a porosity between 30 and 35 percent at the surface that decreases to porosities ranging from 5 to 15 percent at a depth of 4000 meters. However, some outliers as for example the Silurian cluster with average porosities of 8 percent at depths around 100 meters and the Paleogene line/cluster around a depth of 2500 meters deviate from this trend.
- Excluding the carbonate reservoirs does not change the general trend of the porosity-depth relationship. The data clusters that deviate from the general trend are still present despite the filtering.
- Separating the measurements by age, the Cretaceous and Neogene measurements, show a decently clear gradual decrease in porosity with depth in accordance with Athy's law. For the measurements of different ages, no clear trend is observed.

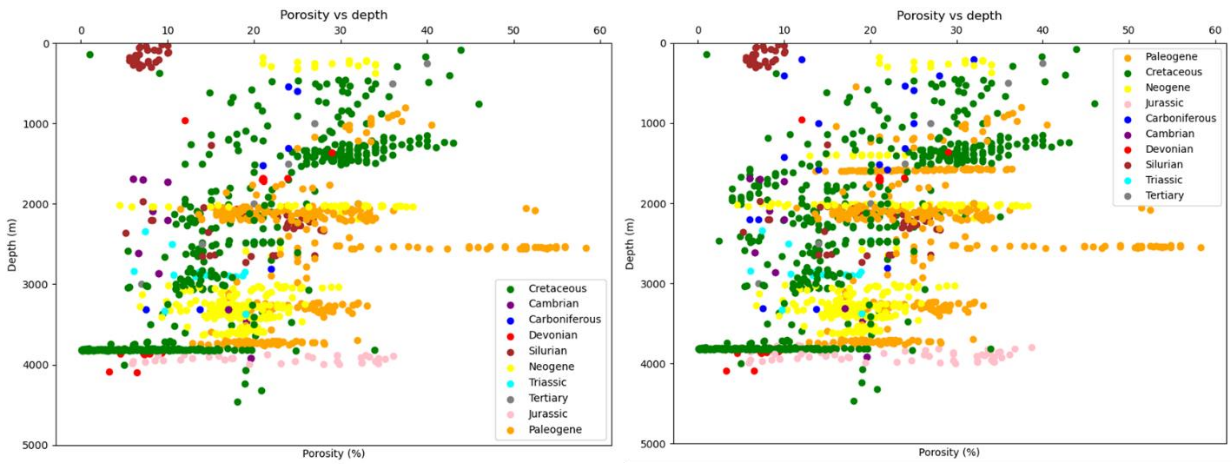

Figure 14: All publicly available porosity-depth data categorized by age used in this project. The figure on the left shows the carbonate filtered measurements and the figure on the right shows all data introspective of reservoir type.

3.1.2. Porosity-depth data coverage.

Figure 15 shows the location of the basins that have sufficient porosity-depth data to estimate an Athy-curve. Here we observe that regions with sufficient data are the basins in northern Africa (Algeria, Tunisia, Libia, Egypt), the west and central Eastern African Rift basins, the Nile and Niger delta, small parts of the horn of Africa and the basins of South-Africa extending the basins in coastal Mozambique. The other parts of Africa do not have sufficient data to construct a specific Athy-curve. We also observe that the areas with sufficient data are smaller in the BGS basin model compared to the Evenick basin model (Evenick, 2021).

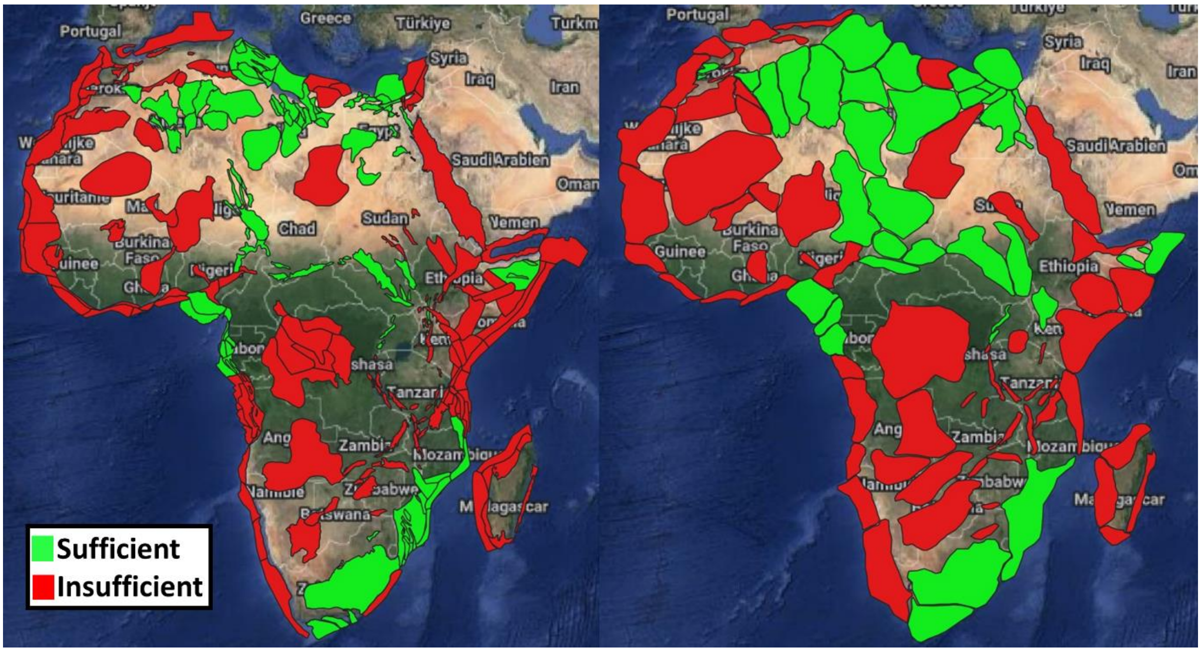

Figure 15: Visualisation of which basis contain sufficient amount of data to construct an Athy-curve. The data is projected onto the BGS TARGET shapefile (Jones, 2022) (left) and onto the Evenick (2021) shapefile (right).

3.1.3. Athy curves per basin

Figure 16 (left) shows the porosity-depth data filtered by basin (name). Figure 16 (right) shows the fitted Athy-curves per basin (name). Here we observe that most of the data points in the point clouds belong to same basin. Generally, the data of a basin is concentrated around one point cloud. Some exceptions (i.e. Abu Gharadig, Gindi, Albert, Nile and Niger Delta, Sirte, Shushan) do exist. Most Athy-curves have surface porosity values ranging between 25 and 45 percent, with the complete range being 9 to approximately 55 percent. At 3000 m depth, the porosity ranges from approximately 2 to 25%.

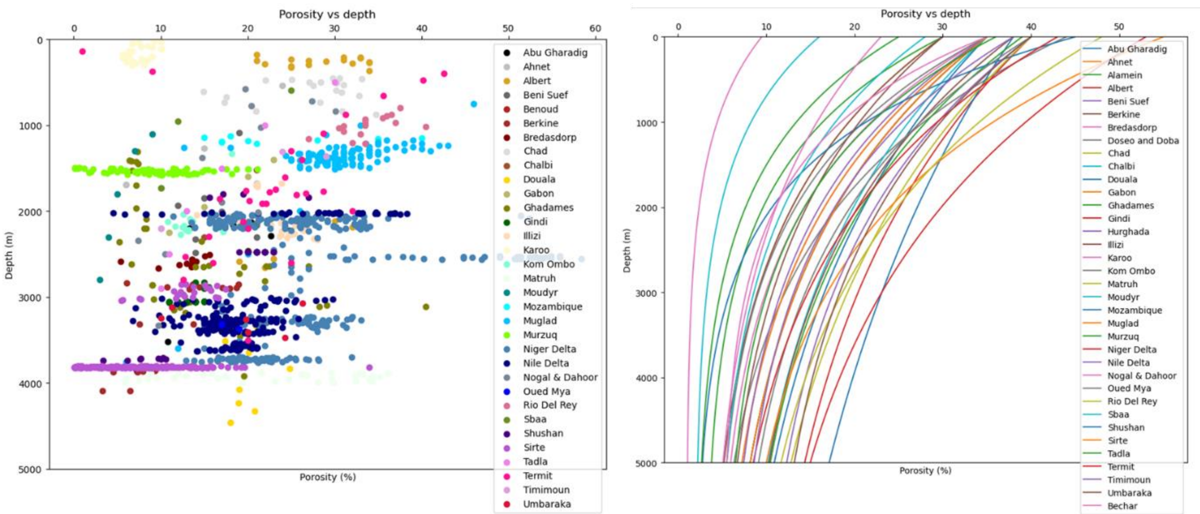

Figure 16: All filtered publicly available porosity-depth data categorized by basin of origin (left). Constructed Athy curves based on Porosity-depth data for the sedimentary basins in Africa (right).

3.1.4. Athy-parameters

The spatial representation of the extrapolated Athy-parameters (including z-scale) are shown in Figure 17. Note that the average/default values for surface porosity, base porosity, k and z-scale are 30%, 4%, 0.45 and 2222,222 m respectively.

From this figure we can observe which porosity-depth relationships deviate from the average values. We observe that the central rift basins in addition to coastal Mozambique, the Nile and Niger Deltas and some basins in N-Africa show higher surface porosities compared to the average value. Notable basins that show lower surface porosities compared to the average value are the Karoo, Murzuq and the Moudyr basins.

Notable basins/areas with elevated base porosity values compared to the average value are the Muglad and Melut central rift basins, the Benue trough and the Nile and Niger Deltas and the Illizi, Ghadames and Pelagian basins in North Africa. The Mouydir and Ahnet basins in Algeria, the Bogor, Doba and Doseo central rift basins and the Karoo and Mozambique basins in the southern part of Africa show base porosity values lower than the average value.

The Mouydir, Bechar and Murzuq basins in North Africa, the Alamein basin in Egypt and the Karoo and Mozambique basins in Southern Africa, show elevated Athy reduction parameter values. Notable basins with lower Athy reduction parameter values are the Albert Edward and Turkana, East Rift basins, the Douala and Niger Delta in coastal Nigeria and Cameroon and the Matruh-Shushan Abu Gaharadig basins in Egypt. The Z-scale parameter values show the inverse trend of the Athy reduction parameter, given that these are inversely correlated.

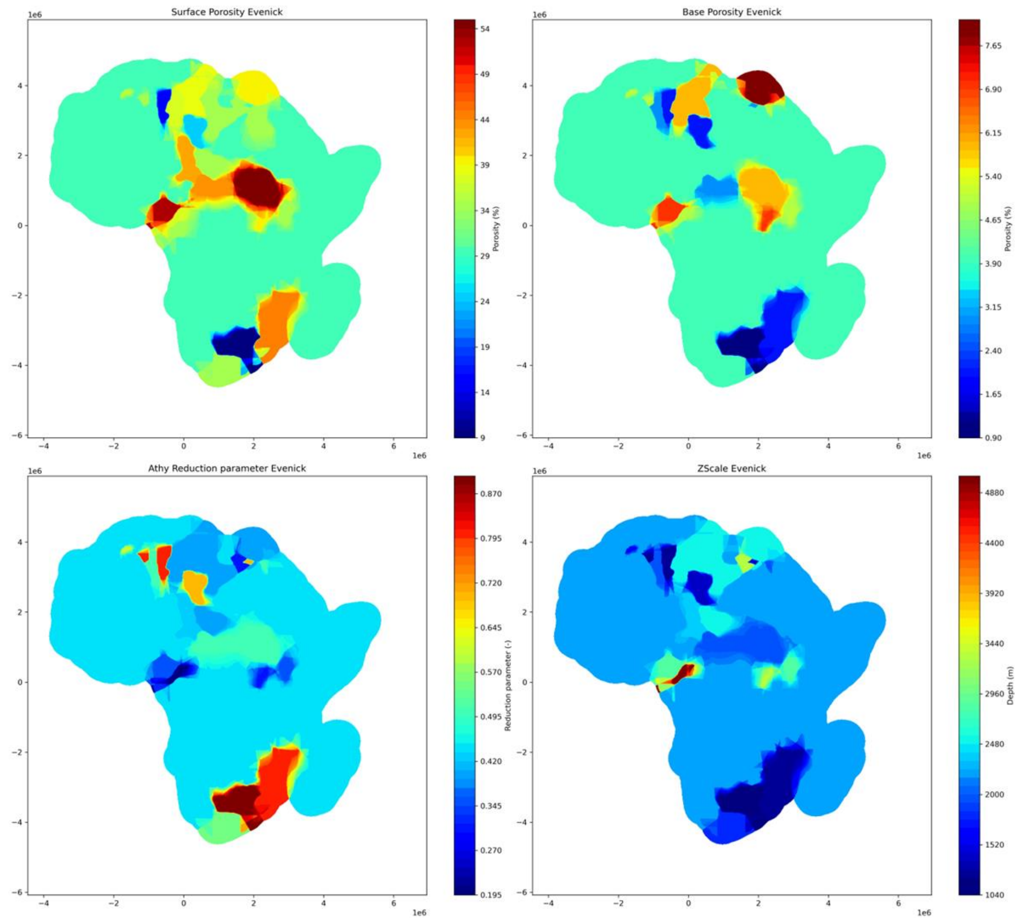

Figure 17: Spatial representation of the Athy parameters projected onto the Evenick (2021) shapefile, used in this analysis. From top left to bottom right: surface porosity, base porosity, Athy reduction parameter and zscale.

3.2. Gravity Inversion

3.2.1. Initial/prior model

Figure 18 shows an example of an initial model of the sedimentary basins of Africa based on the sedimentary thickness maps of Laske & Masters (2013) and Straume et al. (2019). The left window shows a horizontal cross-section in map view at a given depth, the middle window shows a E-W cross-section at a given latitude/northing, the right window shows a N-S cross-section at a given longitude/easting. The depth can be chosen interactively by clicking in the cross-section (middle and right) windows whereas the vertical cross-section latitude/longitudes can be determined by clicking the plan view (left) window. The layers of the model from top to bottom are air (yellow), seawater (orange), sediment (dark orange), upper crust (light green), lower crust (dark green), mantle (blue).

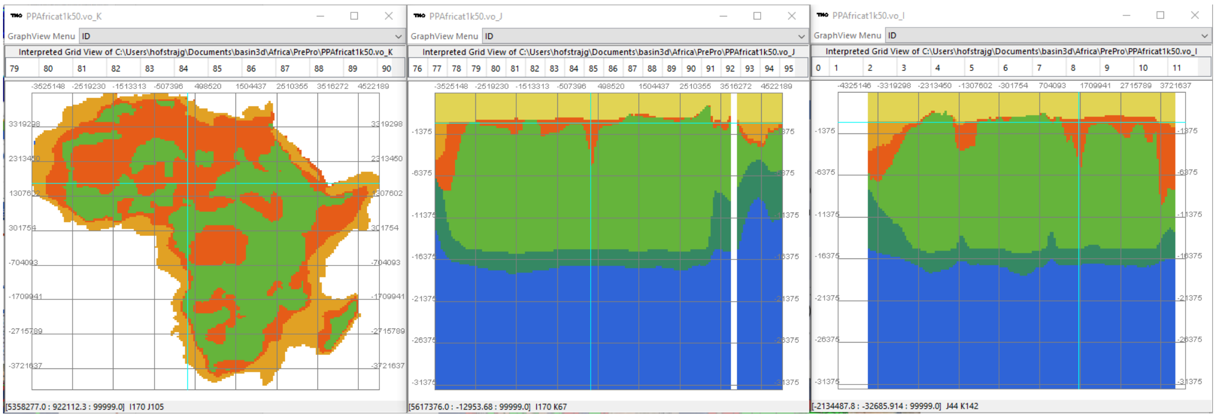

Figure 18: Basin3D prior model visualisation. From left to right: Map view, N-S cross-section, E-W cross-section.

3.2.2. Sedimentary Thickness Maps (MDA4)

The results of the gravity inversion MDA4 runs are presented for each sub-area respectively. The results for the Zaire basin are shown here (Figures 19-22), whereas the other sub-area results are shown in the Appendix section.

The left part of the first figure per sub-area section shows the gravity anomaly observation values (circles in front) versus the gravity anomalies values derived from the model resulting from the inversion model (cells in the back). The color indicates the magnitude of the gravity anomaly (mGal) as indicated by the scale bar. Note that both the scale bar for the observations (left) and the model (right) are identical, therefore the observation values and the model values can be compared directly. The right part of the first figure per sub-area section shows the residual between the gravity observations and the model gravity anomaly values (circles in front) (mGal) versus the modeled gravity values in the back (cells in the back). The residual is defined by the subtraction of the observed values from the modeled values. The left scale bar is for the residual values in front and the right scale bar is for the modeled values in the back, these are not identical.

The second figure per sub-area section shows the modeled gravity anomalies (y-axis) versus the gravity anomaly observations (x-axis) in mGal.

The third figure per sub-area section shows the sediment thickness of the prior model (in meters) on the left and the sediment thickness obtained through gravity inversion modeling (in meters) on the right.

The fourth figure per sub-area section shows density values in the Basin3D viewer with the panels as described in the initial/prior section. The depth and location of these cross-sections are chosen such that they show a representative part of the sub-area in question. Note that these figures are meant to illustrate general crustal density variations under the sub-area.

Zaire

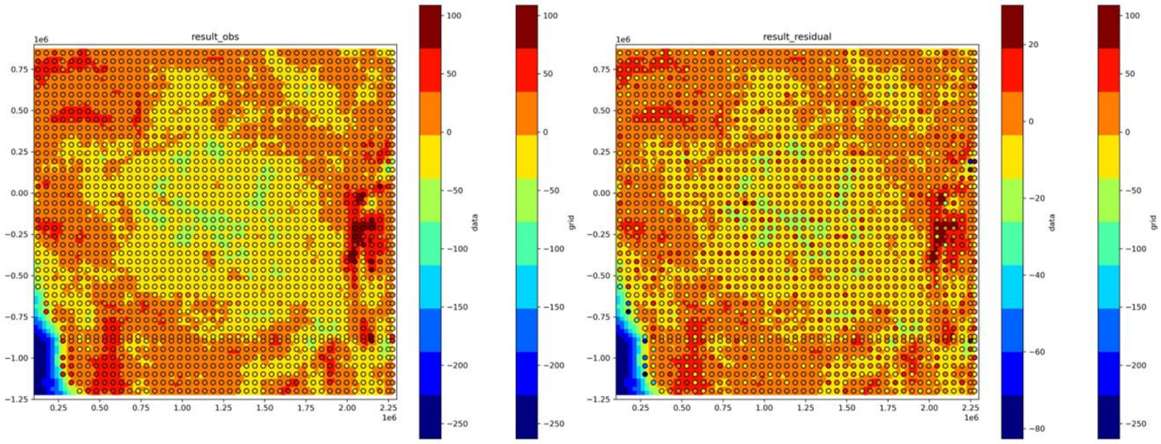

Figure 19: The left part shows the gravity anomaly observation values (circles in front) versus the gravity anomalies values derived from the model resulting from the inversion model (cells in the back). The right part shows the residual between the gravity observations and the model gravity anomaly values (circles in front) (mGal) versus the modeled gravity values in the back (cells in the back)

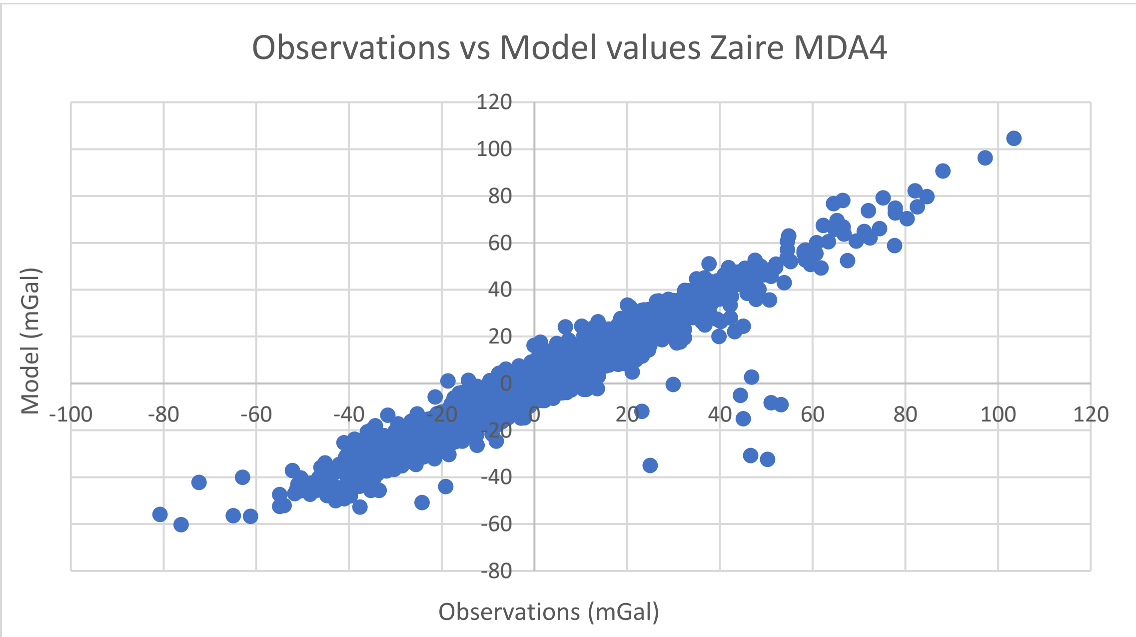

Figure 20: Gravity anomaly observations (x-axis) vs the modelled values (y-axis) for the MDA4 Zaire basin inversion model.

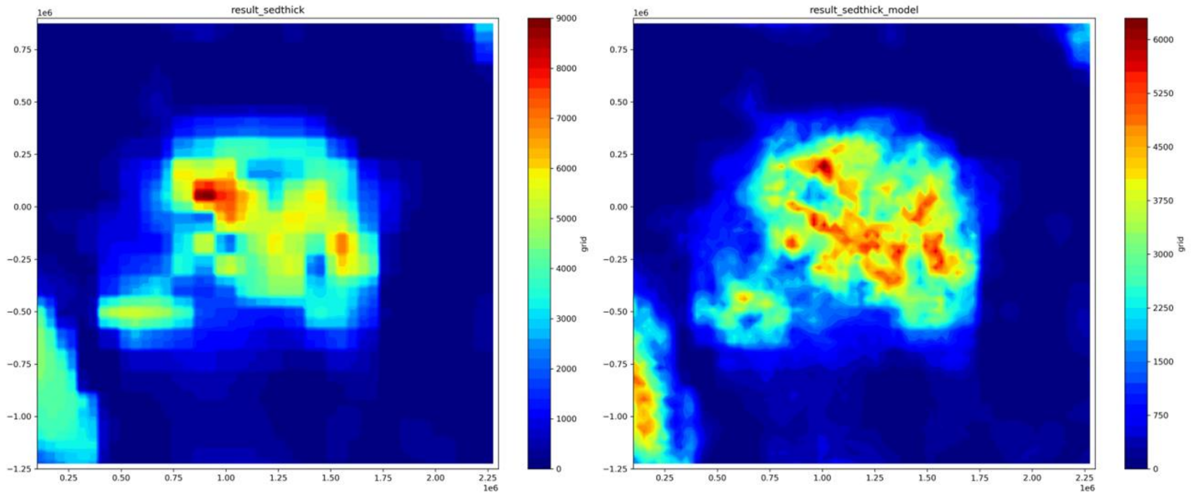

Figure 21: Sediment thickness maps of the prior model (left) and the modelling results (right), of the Zaire basin.

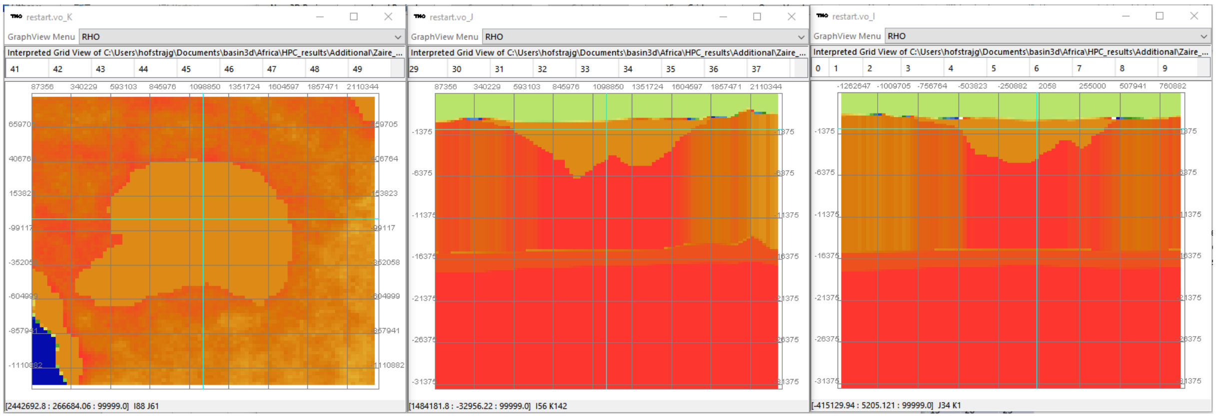

Figure 22: Crustal density distribution Zaire basin. From left to right: Map view, N-S cross-section, E-W cross-section.

Figure 23 shows the sediment thickness map of all the sub area inversion results stitched together onto the input sediment thickness map.

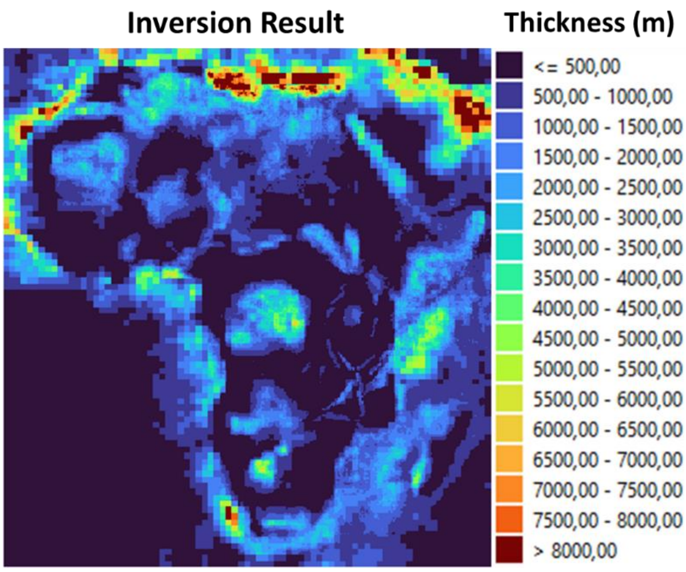

Figure 23: All sub-area gravity inversion results stitched onto the prior model. Note that the "," is supposed to be a "." in the legend.

From these sub-area results and figures we can make the following general observations.

- The resolution of the new model is significantly better than the resolution of the prior model. The results of the results of the low resolution continental scale “sub area” map are an exception. Consequently, the fit of the continental sub-area model to the observations compared to the fit of other (sub-area) models is worse.
- Note that the apparent resolution decrease of the offshore areas is because these areas have not been modified during the inversion modeling and therefore retain their input resolution.
- The basin structures of the MDA4 model results are similar to the ones of the prior models.
- However, the sediment depth of these models is shallower than the sediment depth of the prior models.
- For most of the models, we observe a clear fit between the observations and the model with a trend that fits around the y = x line.
- The absolute residual around this main trend generally ranges from 0 to 15 mGal and rarely exceeds 20 mGal. These residuals show no clear preference to negative or positive values.
- This fit is also expressed in the spatial distribution figures except for offshore areas. The absolute residual increases significantly when transitioning from the onshore to the offshore part of the model.
- The model gravity anomalies in the offshore parts of the sub-area are significantly smaller than the gravity anomaly observations at the same location. This large discrepancy between the model and observations in these areas often exceeds the six standard deviations maximum imposed by the Basin3D software. This is expressed by the straight line parallel to the main trend (y = x). This maximum error line can roughly be expressed by y = x – 80 for all sub-areas.
- In the areas with this maximum error line, in addition to the residuals around the main trend (y = x), most residuals appear to be negative between -20 and -80 mGal.
- Sub-areas that do not cover (large) offshore areas do not show these large residuals.
- When ignoring the effect of the onshore-offshore transition, no clear absolute residual increase towards the edges of the sub-area is observed.
- Looking at the crustal densities we observe that the upper crustal densities are significantly increased under sedimentary basins and the offshore parts of the model. These values far exceed the lower crustal density values and approach density values comparable to the density of the mantle. At locations without sedimentary cover, the crustal density varies till a far smaller degree with a minor preference for increasing the density.
- Note that the SE rift basins models do not show large increases in crustal density under the sedimentary basins. Here we generally observe a decrease in crustal density compared to the prior model. Note that the degree of fit between the model and observations is comparable to the other models.

4. Parameter Study

4.1. Set-up

To determine the effect of the input parameters on the gravity inversion modelling we performed a parameter study on the sediment and the crustal density related parameters. The investigated parameters and their values are listed in Table 5. In this section we also discuss the differences in results between the forward (No DA), MDA1 and MDA4 models. For the analysis we choose the Zaire basin in the Democratic Republic of Congo as this basin is studied extensively and there are therefore plenty of geological cross-sections available for validation.

Parameter	Abbreviation (Figure)	Lower	Middle	Upper
SedRho (kg/m^3)	"R(***X***)F"	2500 **(A)**	**2600** **(B)**	2700 **(C)**
Phi0 (%)	"R2600F_P0_(***X***)"	36 **(I)**	**41** **(B)**	46 **(J)**
Zscale (m)	"R2600F_ZS_(***X***)"	2500 **(G)**	**3000** **(B)**	3500 **(H)**
PhiBase (%)	"R2600F_PB_(***X***)"	**0** **(B)**	5 **(K)**	10 **(L)**
CrustRhoDA ± (%)	"R2600F_RDA(***X***)"	15 **(M)**	**20** **(B)**	25 **(N)**
CrustRhoDA var range (cells)	"R2600F_RDAVar(***X***)"	15 **(O)**	**20** **(B)**	25 **(P)**
SedDepthDA ± (%)	"R2600F_SDA(***X***)"	80 **(Q)**	**100** **(B)**	120 **(R)**
SedDepthDa var range (cells)	"R2600F_SDAVar(***X***)"	**5** **(B)**	10 **(S)**	15 **(T)**
Runs in Ensemble	"R2600F_R(***X***)"	2500 **(E)**	**3000** **(B)**	3500 **(F)**
Arbitrary Sed depth (m)	"R2600F_SD(***X***)"		1500 **(D)**	

Tabel 5: Parameters, parameter variation ranges and figure annotation/abbreviation codes used in the parameter study. The "X" in bold in the abbreviation column indicates the respective number shown in the "Lower", "Middle" and "Upper" columns. The letters in bold in these columns, indicate the deviating input parameters of the results shown in Figure 24 and 25. The default values are indicated by the underlined values and the letter "B".

4.2. Results

The results of the parameter study are shown in figures 24-25. Figure 24 shows the gravity anomaly in mGal for the model derived from gravity inversion using MDA1 and 3000 runs along the y-axis and the observed gravity values from satellite data along the x-axis. Figure 25 shows the sediment depth in meters of the Zaire basin. The individual scales are shown next to the respective plots, where red indicates deeper values and blue indicates shallower values.

4.2.1. Effect of different DA input settings

In the model-observation plots for the MDA1 3000 run models, we observe that the overall trend between the modelled and observation values is relatively similar for each plot. Some plots, like Figure 24C-D and 24R show marginally better fits compared to the other plots. The outliers in each plot are all located around the same mGal value, with roughly similar misfits between the observations and the modelled gravity anomaly values.

Considering the sediment thickness maps obtained from the parameter study (Figure 25), we observe that all parameter runs show similar overall shapes of the Zaire basin. The basin is composed of a larger deeper part in the North-East with fragmented deeper spots located often in the central part of the basin and a smaller part in the South-West, connected via a local high. The exception to this is the run with the arbitrary sediment depth, Figure 25D. The sediment thickness map obtained from this parameter run shows a seemingly random thickness pattern with median values of approximately 1400 meters and maximum and minimum values approaching 2000 and 630 meters respectively. The maximum sediment thickness of Figure 25A-C, E-J, M and Q-R, ranges from 6700 to approximately 7200 meters. Runs K, L, N, O, P, S show maximum thicknesses ranging from 6000 to 6500 meters. Run T appears to deviate the strongest from the other runs (baring D), with a maximum thickness close to 4000 meters and the deepest parts being located at the edges of the basin. Also, some maps show more equal sediment thicknesses for the whole basin whereas other runs show more fragmented thicker and thinner parts composing the basin.

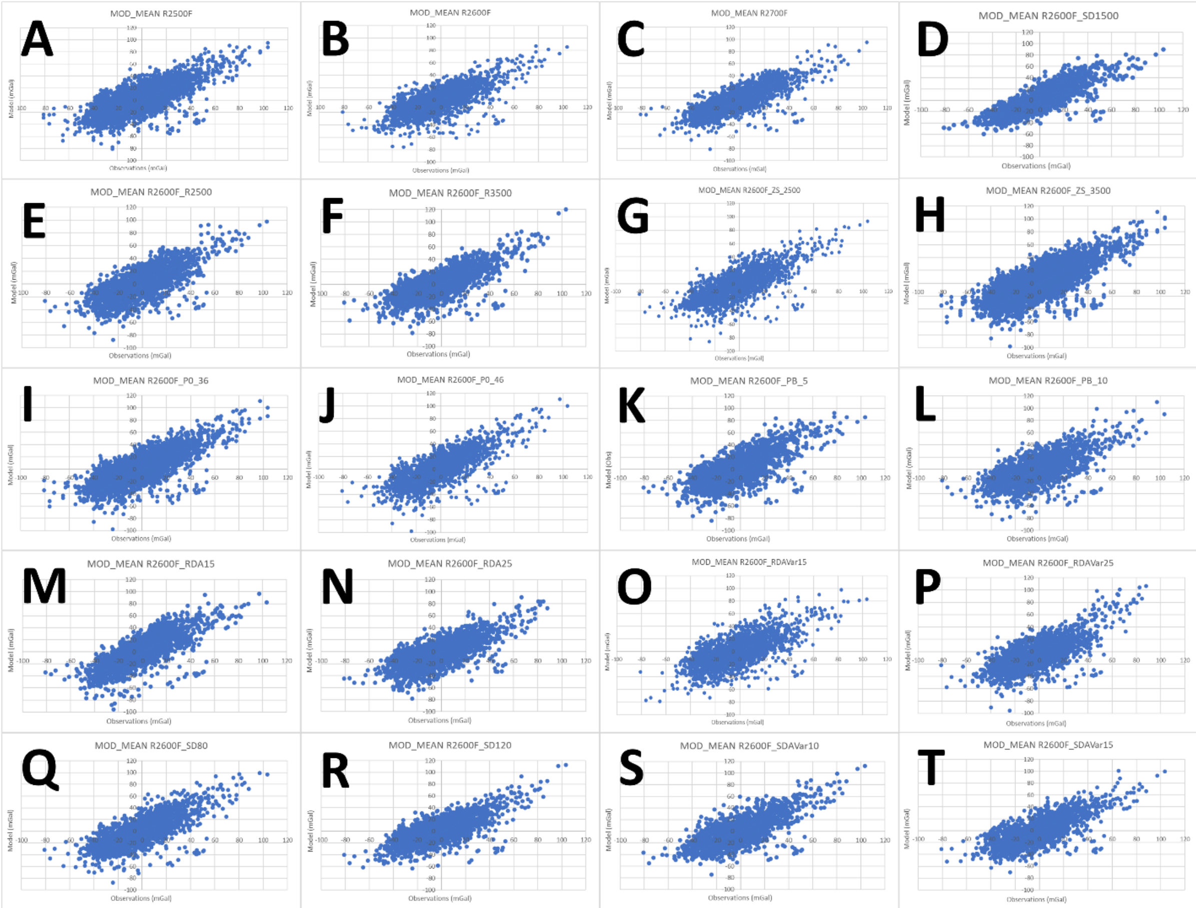

Figure 24: Gravity anomaly observations versus modelled gravity anomalies for the different parameter study runs. The letters from the different runs are explained in table 5.

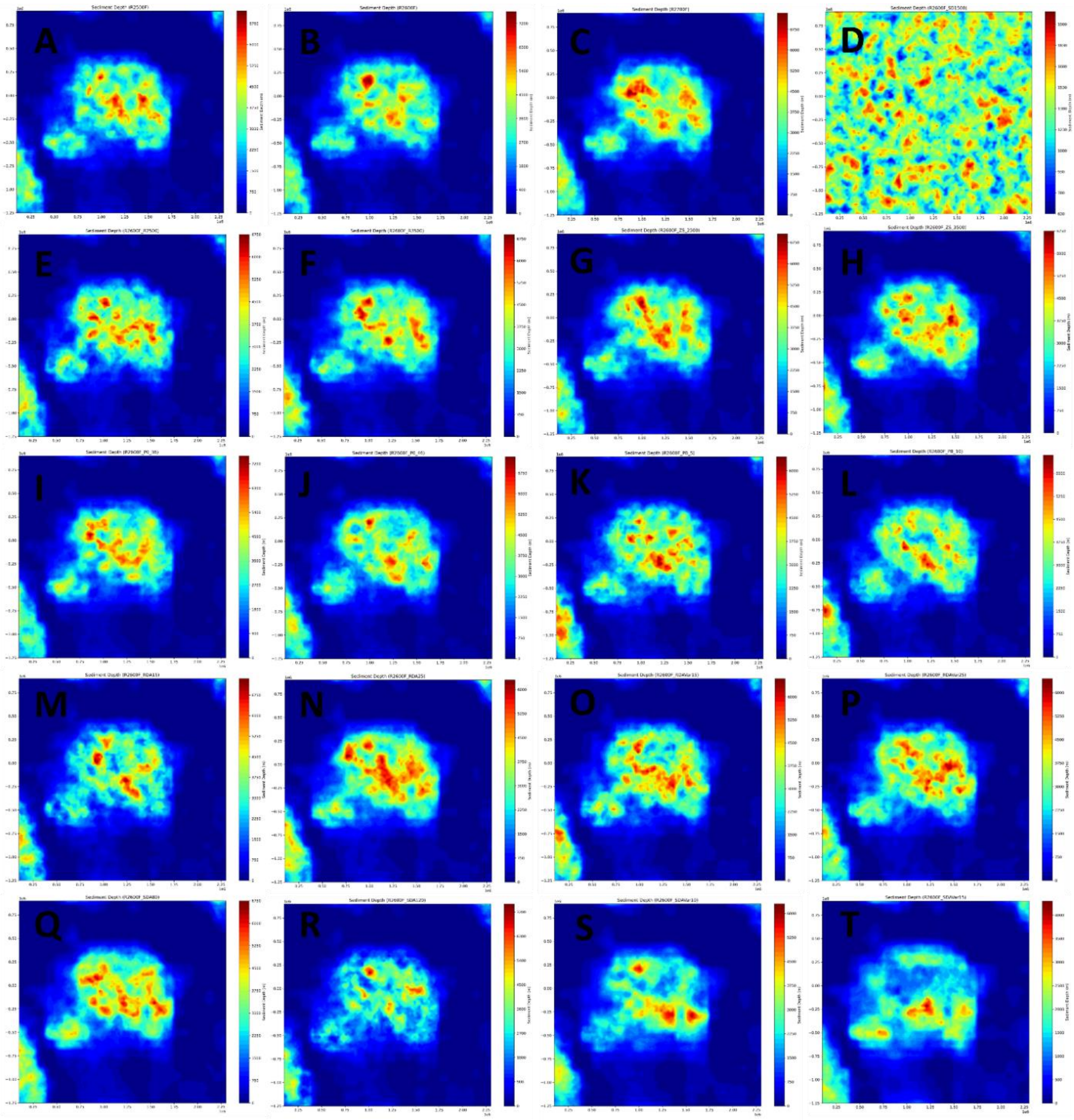

Figure 25: Sediment thickness maps of the Zaire basin derived from the parameter study gravity inversion modelling. The letters from the different runs are explained in table 5.

4.2.2. Effect of MDA types

Figure 26 shows the fit between the gravity signal observations and the gravity response at the top (A1-C1) and the respective sediment depths at the bottom (A2-C2) of the different multiple data assimilation models for the Zaire basin.

From Figure 26A1-2, we can observe that there is a very rough trend between the prior model gravity anomalies and the observed gravity anomalies. However, the point cloud is very wide with some points exceeding the six standard deviation limit. The resulting sediment depth map (prior model from Laske & Masters) is coarse in resolution and the deepest parts of the basin (NW & SE) approaches nine kilometres in depth.

Figure 26B1-2, shows a decently good fit between the observations and the MDA1 model gravity anomalies. However, while some data still deviates from this trend, the residuals do not approach the six standard deviation limit. The resulting sediment thickness map shows a good resolution, and the deepest parts of the basin are more distributed in the NW and centre part of the basins. These parts reach depths of around 7200 meters.

Figure 26C1-2, shows a good fit between the observations and the MDA4 model gravity anomalies. A cluster of data, located around the 20-60 mGal range, still deviate from this trend. The resulting sediment thickness map shows a good resolution, where the deepest parts of the basin cluster more strongly around the centre of the basin with some parts exceeding six kilometres in depth.

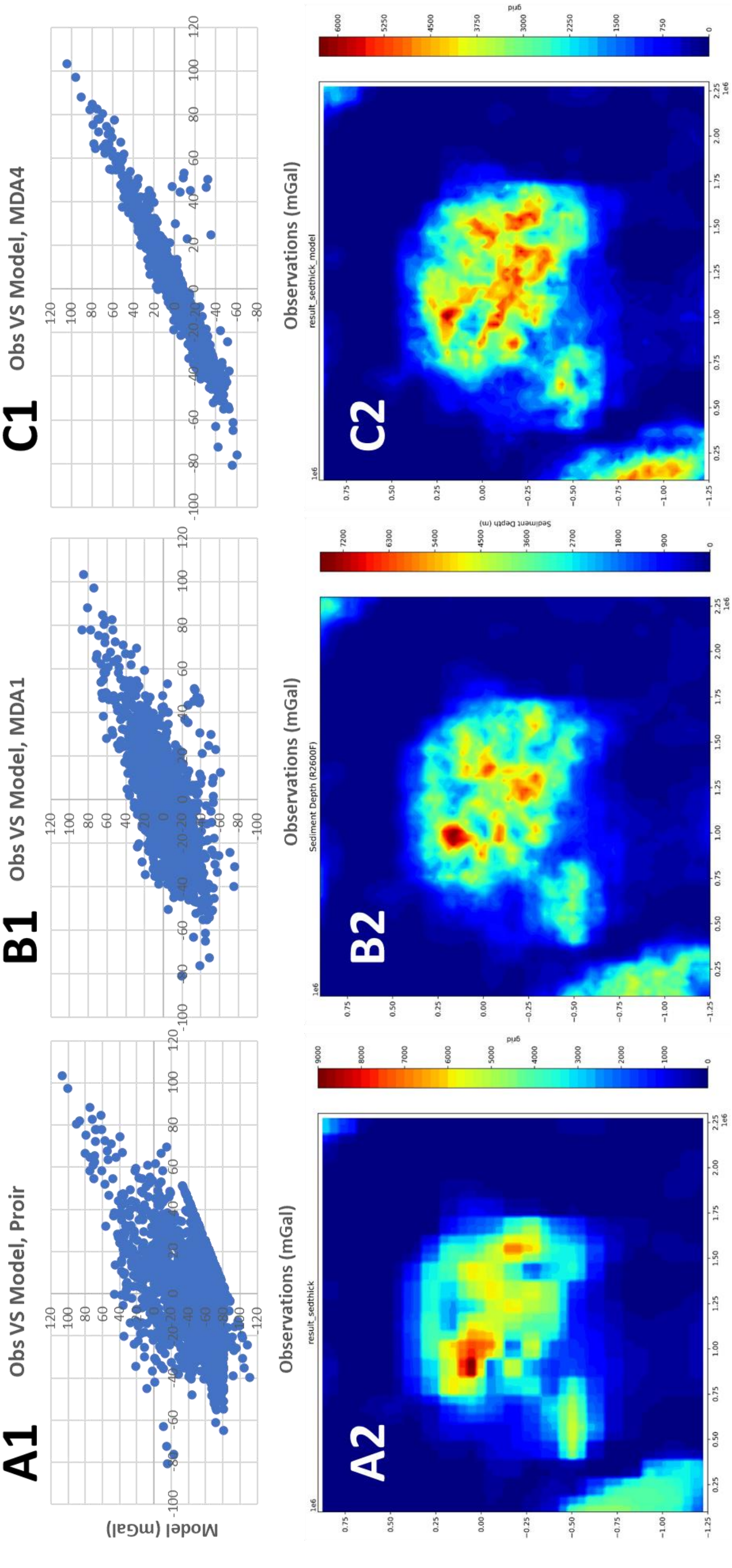

Figure 26: Observation versus modelled gravity anomaly plots on top (1a-1c), and the sediment thickness results for the respective number of MDA (2a-2c). From left to right: No MDA, MDA1, MDA4.

5. Discussion

5.1. Porosity-Depth

- *Poro-depth estimates based on sediment age*

From Figure 14, we observe that measurements from Cretaceous to recent, are abundant enough to observe trends and make interpretations. These measurements show a relatively clear porosity reduction with depth as can be expected from Athy's law. Measurements originating from older sediments are not as abundant and also don't show a clear porosity-depth trend.

Based on these observations, you could speculate that the younger reservoirs experienced relatively similar porosity reductions with depth despite their locations. If assumed to be true, this suggest that a similar amount of burial anomaly is experienced by all sediments of this age. Additionally, given the extrapolated surface porosities of these sediments, estimated to be in between 30% and 40%, it could be argued that little to no burial anomaly took place on average on sediments with these ages. Because of the absence of sufficient measurements on older sediments, it is not possible to make comparable inferences about these older reservoirs.

- *Differences between basins*

Figure 27 shows the porosity-depth relationships (full lines) vs the typical clay-rich and clay-poor sandstones (BT1 model, Limberger et al., 2017) (dashed lines). The figure is divided in two plots to better distinguish between individual curves.

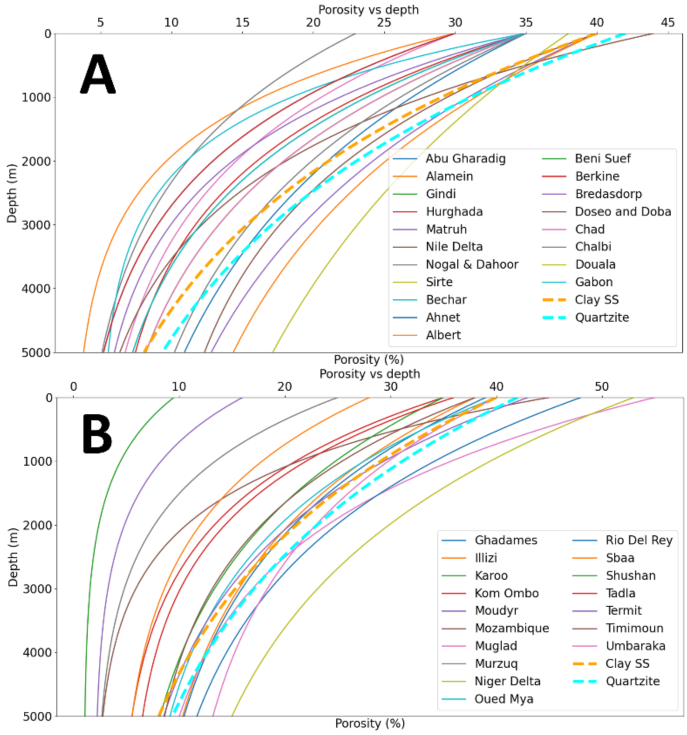

Figure 27: Constructed porosity-depth relationships (full lines) and standard clay-rich and clay-poor sandstones porosity-depth curves (dashed lines) (B1T model, Limberger et al., 2017).

From Figure 27, we can observe that the majority of the porosity-depth relationships deviate from the standard sandstone curves (Limberger et al., 2017). Because of the assumptions underlaying this analysis, we will be assigning each of the curves to one of three categories based on how much each curve deviates from the standard sandstone curves. Note that for this approach, we are only interested in the deviation in the negative direction as this could be interpreted as a burial anomaly. Category one represents curves that show weak or minor deviations from the standard, category two represents curves that deviate more strongly, and the last category represents the curves that deviate the strongest from the standard curves. These three categories are assigned a burial anomaly chance, which ranges from low to medium to high depending on their deviation from the standard curves. The results of this classification are shown in Table 6.

Tabel 6: Burial anomaly chance categorization based on the constructed Athy-curves.

Basin Name	Deviation	Burial Anomaly Chance
Sirte, Douala, Doseo, Doba, Nile Delta, Matruh, Albert, Abu Gharadig, Gindi, Chad, Chalbi, Ghadames, Illizi, Muglad, Niger Delta, Oued Mya, Rio Del Rey, Shushan, Termit, Timimoun, Umbaraka	Weak	Low
Bredasdorp, Hurghada, Beni Suef, Gabon, Kom Ombo, Sbaa, Tadla	Medium	Medium
Nogal, Dahoor, Alamein, Bechar, Ahnet, Berkine, Moudyr, Mozambique , Murzuq	Strong	High

- *Literature validation*

In the following section, we compare our burial anomaly estimates with the publicly available burial history data for different basins, to validate our methods and results.

- **Central rift basins**

Figure 28 shows the burial histories of the Central African Rift basins based on different wells (Morakinyo et al., 2021). These results show uplift events recorded in the Central African Rift basins at the end of the Cretaceous and Paleogene. However, these results also show that the reservoir rocks are located currently at their deepest point in their burial history. This would suggest that there is no burial anomaly present in these basins. This interpretation is in line with our analysis of the porosity-depth data which suggests that the presence of a burial anomaly is low for the Doba and Doseo basins.

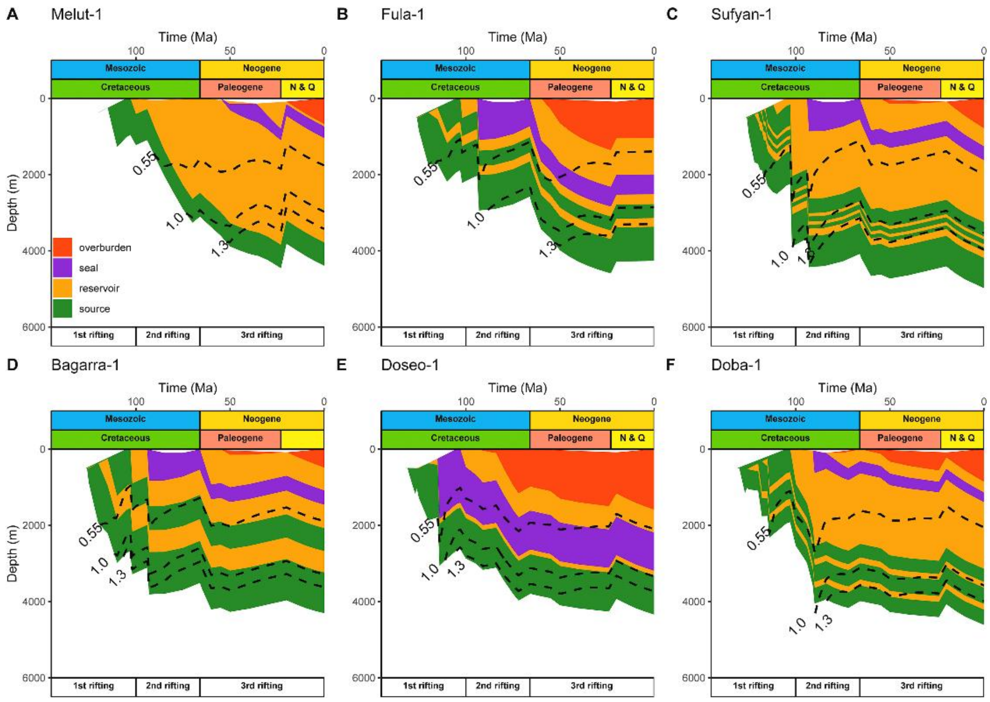

Figure 28: burial histories of the Central African Rift basins based on different wells, from Morakinyo et al., 2021.

- ### Chad

Multiple wells (Mbeji-1 and Murshe-1, Kanadi-1, Masu-1 not shown, Figure 29) from the Chad basin show similar burial histories, without evidence for an uplift event (Nwankwo et al., 2014). These results suggest the absence of a burial anomaly in the Chad basin. This interpretation is in line with our analysis of the porosity-depth data suggesting a low chance for the presence of a burial anomaly in the Chad basin.

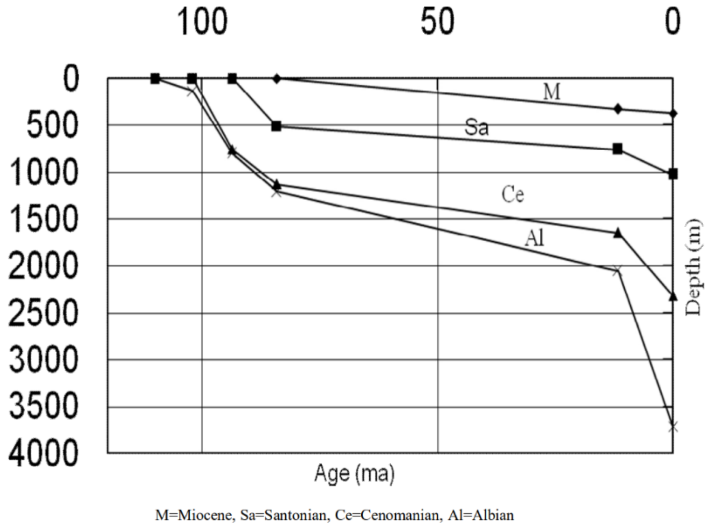

Figure 29: Burial history of the Mbeji-1 well located in the Chad basin, from Nwankwo et al., 2014.

- ### Bongor

Two wells (Baobab C-2, Raphia S-1) (Figure 30) from the Bongor basin that show two phases of uplift/erosion in the Paleogene and the Neogene (Cheng et al., 2022). This suggests a burial anomaly for sediments from the K & R formations, in which the main reservoirs are located (Cheng et al., 2022). We have no direct porosity-depth data from the Bongor basin, yet these results could be an indication for the presence of a burial anomaly in nearby located basins.

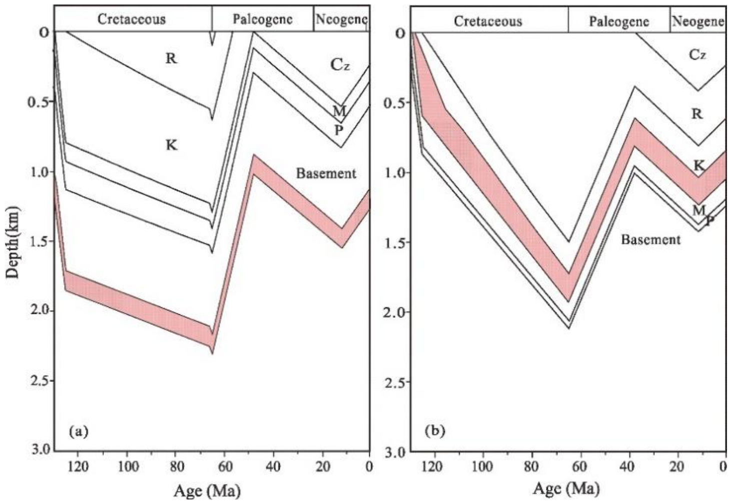

Figure 30: Burial history of the Baobab C-2 and Raphia S-1 wells located in the Bongor basin, from Cheng et al., 2022.

- ### Termit

The burial history derived from the Yogou-1 (and Sokor-1, Goumeri-1 and Faringa-1, not shown) well in the Termit basin (Figure 31) (Harouna et al., 2017) shows no evidence for an uplift event and thus no evidence for the presence of a burial anomaly. These results are in line with our interpretation of the porosity-depth data of the Termit basin.

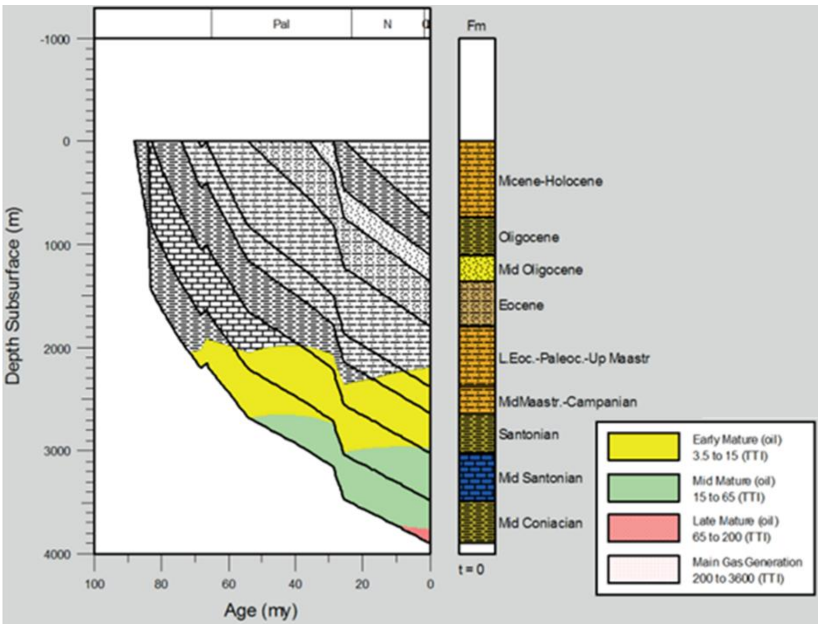

Figure 31: Burial and maturation history of the Yogou well located in the Termit basin, from Harouna et al., 2017.

- **Reggane**

Figure 32 shows the burial history of the RPL-101 well in the Reganne basin (Makhous & Galushkin, 2003). From this figure we can interpret two minor uplift events around approximately 320-300 and 50 Ma. These results can be used as evidence for the presence of a minor burial anomaly. We have no direct data from the Reggane basin, but these results could be an indicator for the presence of a burial anomaly in nearby located basins.

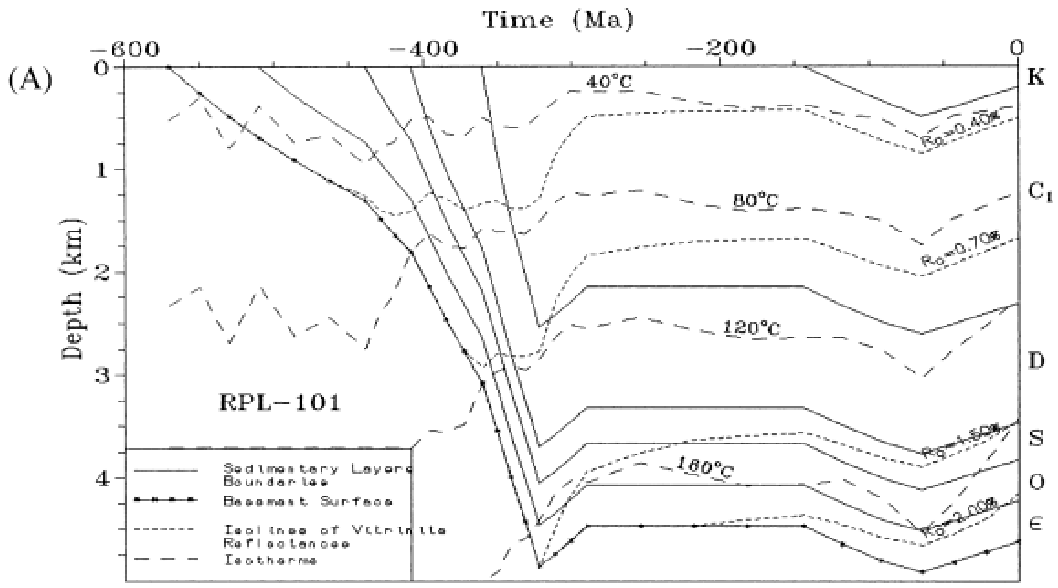

Figure 32: Burial, temperature and maturation history of the RPL-101 well located in the Reggane basin, from Makhous & Galushkin, 2003.

- **Ghadames**

Figure 33 shows two burial history models for the eastern Ghadames basin (Underdown et al., 2007). Both history models show the presence of two uplift/erosion events that in turn, can be used as evidence for the presence of a burial anomaly. However, these findings are in contradiction with our analysis of the porosity-depth data originating from the Ghadames basin suggests which suggests that the chance for the presence of a burial anomaly is low. Without more detailed analysis it is difficult to determine the cause of the discrepancy. A hypothesis could be that the data from the younger sediments is more abundant compared to the data originating from older sediments and might have dominated in constructing the porosity-depth relationship. However, according to the models from Underdown et al. (2007), these younger sediments would still have been subjected to a phase of uplift during the alpine orogeny.

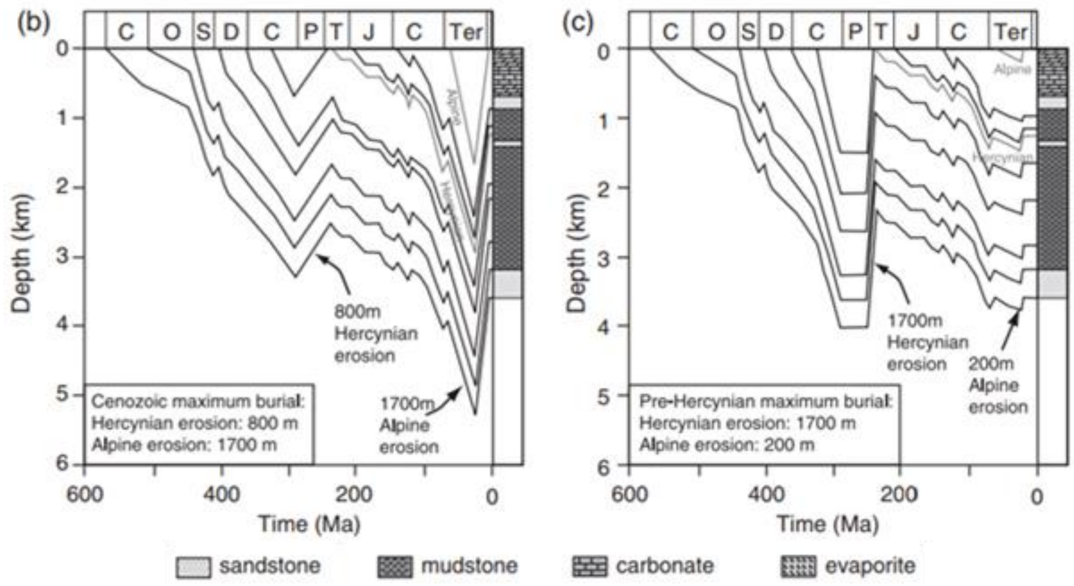

Figure 33: Two burial history models for the Ghadames basin, from Underdown et al. (2007).

- **Shushan**

Figure 34 shows the burial history of the Shushan basin derived from the Khalda-21X well (Dally et al., 2023). From these results we can observe an uplift/erosion event during the onset of the Paleogene. This observation can be used to argue in favour of the presence of a burial anomaly. Our porosity-depth data analysis from the Shushan basin, however, suggests that the presence of a burial anomaly is low. Despite this contradiction, we note that according to the results of Dally et al. (2023), the sediments are located approximately 300 meters (1000 feet) higher than their deepest deposition level. Additionally, the deviation of the porosity-depth curve of the Shushan basin from the sandstone curves is close to the ones from the medium category. We therefore argue that this data is in line with our interpretation of the burial anomaly presence chance.

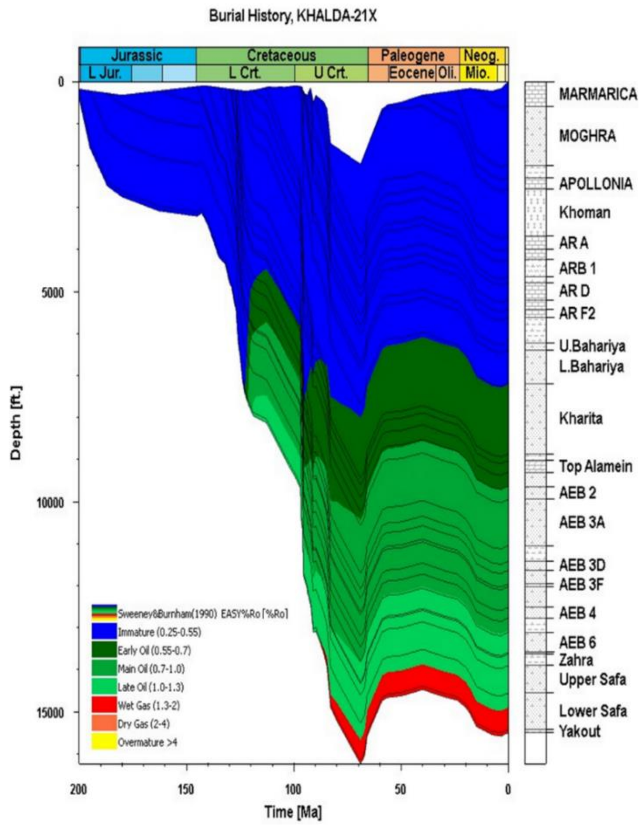

Figure 34: Burial history of the Khalda-21x well located in the Shushan basin, from Dally et al. (2023).

- **Muglad**

Figure 35, shows the burial history of one of the sub-basins in the Muglad basin derived from the Keyi-N1 & Moga-9 wells (Makeen et al., 2016). From these results we can observe several uplift events which could be used as evidence in favour of a burial anomaly. However, note that based on the Keyi N-1 well, the sediments are currently located at their deepest point in their burial history. The sediments in the Moga-9 well are currently approximately 200 meters higher than their deepest location. Our results are therefore in line with the data from the Keyi N-1 well, and slightly contradict the data from the Moga-9 well. It could be that most of the data analysed originates from wells with comparable burial histories as the Keyi N-1 well. However, it is important to note the inter-basin deviations in burial anomaly in the context of this research.

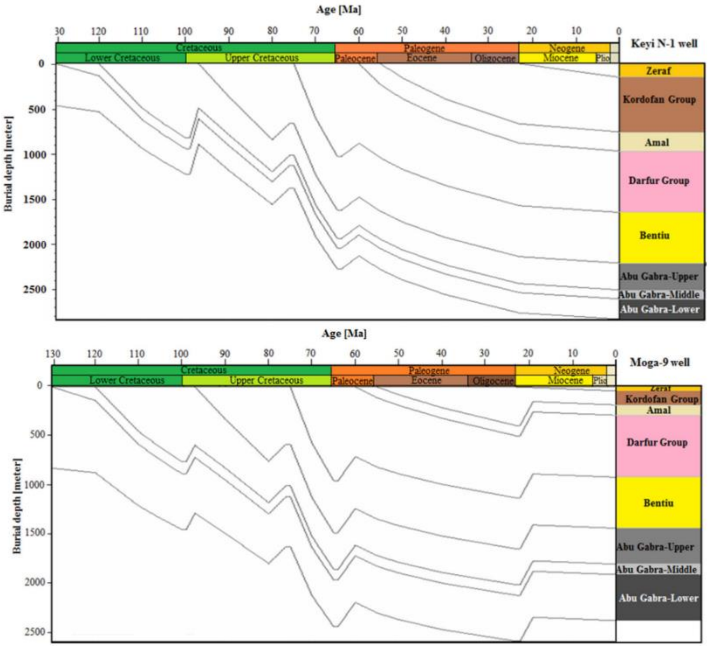

Figure 35: Burial hisotry of the Keyi-N1 and Moga-9 wells located in the Muglad basin, from Makeen et al., 2016.

- **Sirte**

Figure 36 shows a derived burial history curve for the Sirte basin derived from the deepest part of the Hameimat Trough (Ahlbrandt, 2001). These results show no evidence that could be used to support the presence of a burial anomaly. These findings are in line with the results of our burial anomaly analysis.

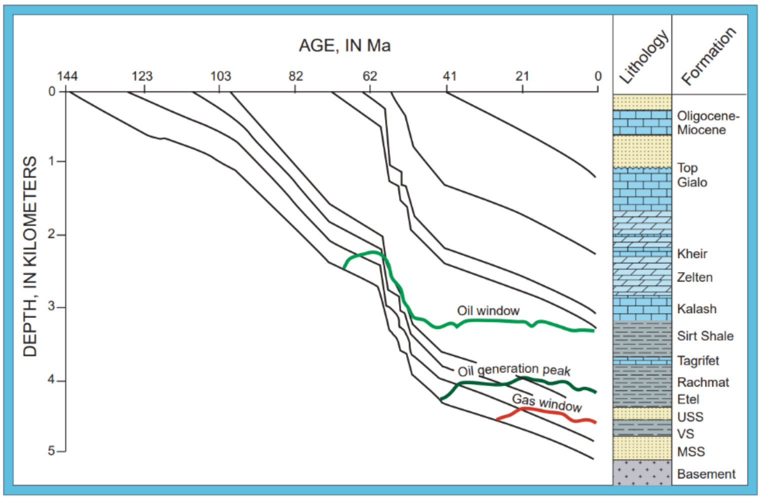

Figure 36: Burial history of the Hameimat Trough in the Sirte basin, from Ahlbrandt, 2001.

- **Murzuq**

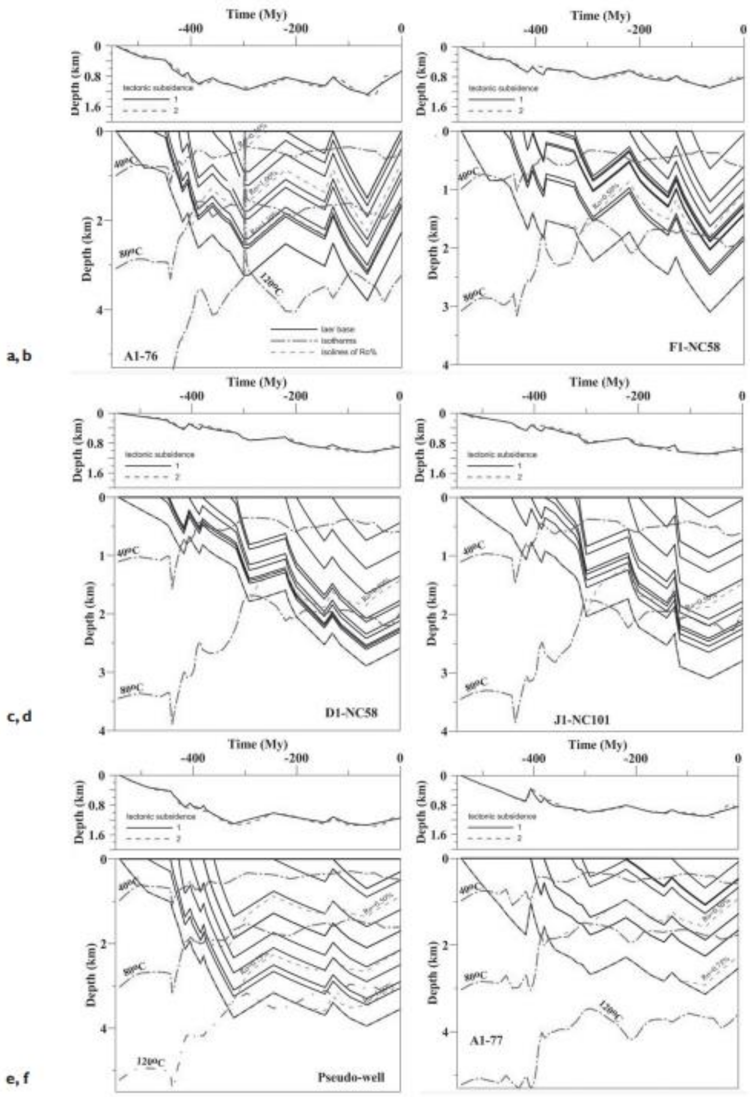

Figure 37: Burial and thermal history of multiple wells (a: AI-76, b: FI-NC58, c: DI-NC58, D: JI-NC101, f: AI-77 and e: pseudo-well), located in the Murzuq basin, from Galushkin et al., 2014.

Figure 37 shows the burial history of multiple wells (AI-76, FI-NC58, DI-NC58, JI-NC101, AI-77 and a pseudo-well), in the Murzuq basin (Galushkin et al., 2014). From these results we can observe that there have been multiple uplift/erosion events. Especially the uplift event from approximately 60 Ma to recent suggests the presence of a significant burial anomaly in the Murzuq basin. These findings support our results of the burial anomaly analysis, where we found a strong deviation from the standard curves suggesting a high chance for a burial anomaly.

- **Nogal**

Figure 38 shows the Burial history of the Nogal basin based on the Nogal-1 well (and the Kalis-1 well, not shown) (Ali & Lee, 2019). These results show a large uplift/erosion event during the middle Cretaceous and a smaller one during the Paleogene. These results could be used as evidence in favour of the presence of a burial anomaly in the Nogal basin. However, the sediments are currently located at their deepest location during their burial history. Our analysis suggests that the chance of the presence of a burial anomaly is high, which would be supported by the large uplift event during the Cretaceous.

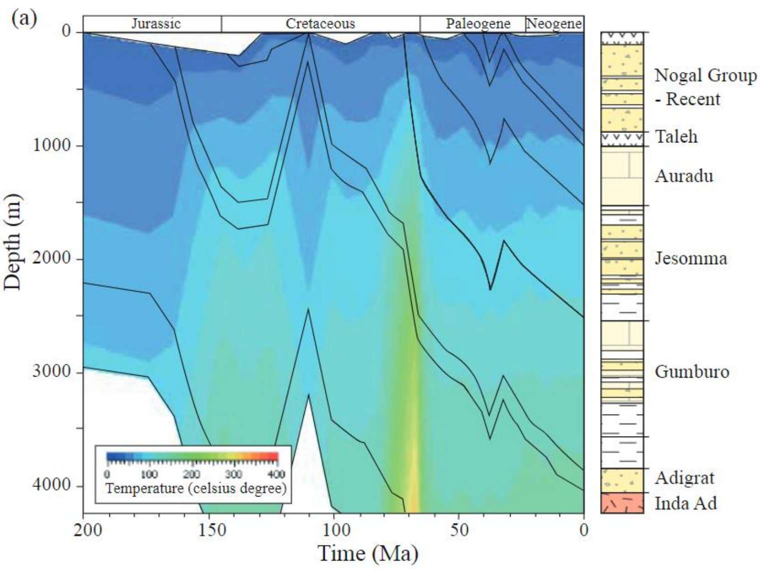

Figure 38: Burial and thermal history of the Nogal-1 well located in the Nogal basin, from Ali & Lee, 2019.

- **Abu Gharadig**

Figure 39 shows the burial history of the SPYGLASS-1X and the AG-24 wells located in the Abu Gharadig basin (Salama et al., 2021). From these results we can observe no clear evidence that could support the presence of a burial anomaly in the Abu Gharadig basin. These results are supported by our findings from the porosity-depth analysis.

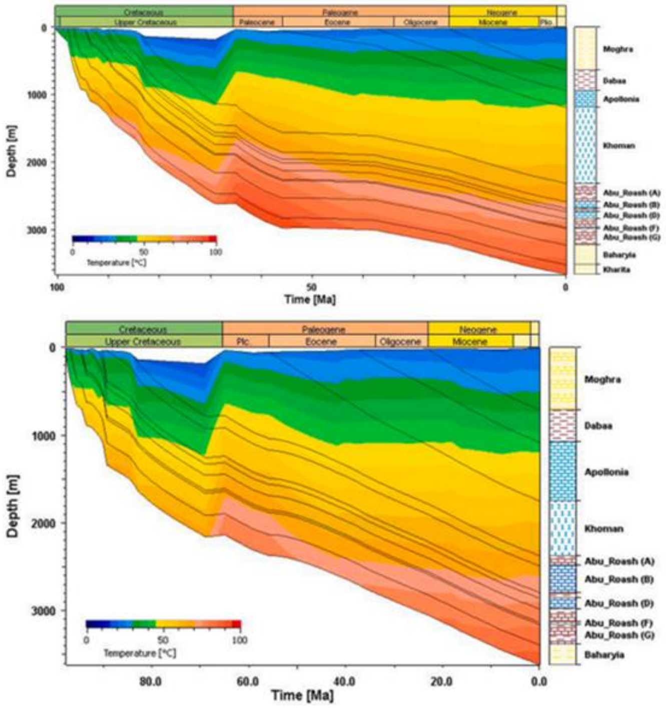

Figure 39: Burial and thermal history of the SPYGLASS-1X AG-24 wells (top and bottom respectively), located in the Abu Gharadig basin, from Salama et al., 2021.

- **Niger Delta**

Figure 40, shows the burial history of the Niger Delta based on the Pologbene 1 well (Other wells not shown show similar trajectories) (Ojo et al., 2012). These results show no evidence that can be used to argue in favour of the presence of a burial anomaly in the Niger Delta. These findings support the results from our analysis.

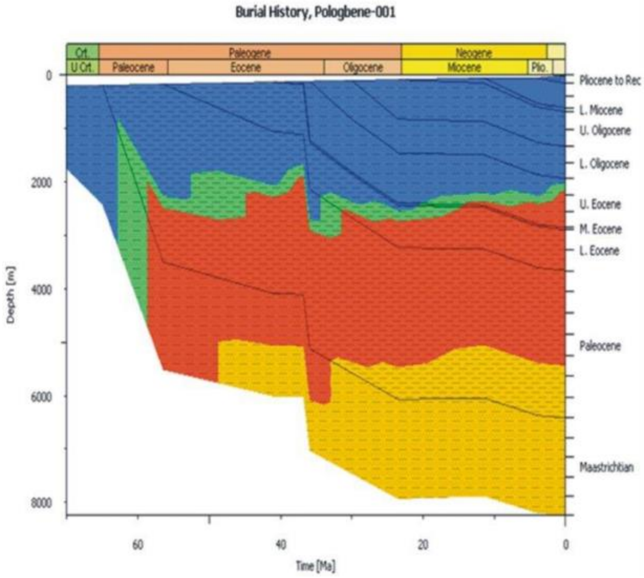

Figure 40: Burial and hydrocarbon zones of the Pologbene 1 well, located in the Niger Delta, from Ojo et al., 2012.

- **Nile Delta**

Figure 41 shows the burial anomaly of the Nile Delta based on the EL Qara 2 and Abu Madi 2 wells (Ramadan, 1990). These results show no evidence that could be used to argue in favour of the presence of a burial anomaly in the Nile Delta. These results are in line with the results from our analysis.

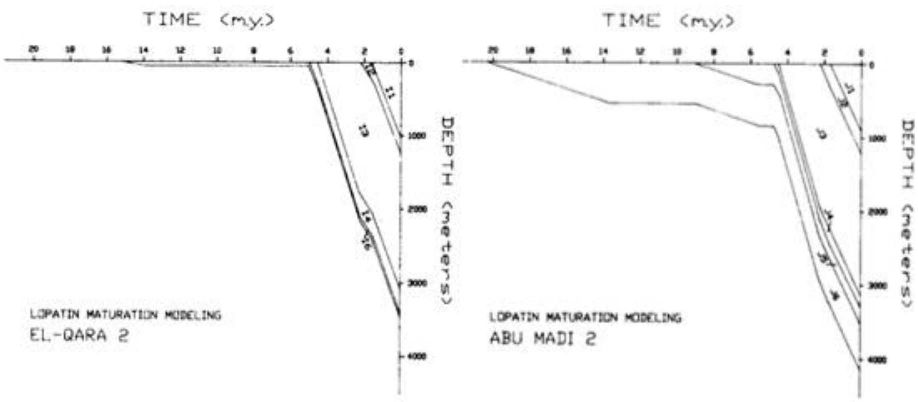

Figure 41: Burial history of the El Qara 2 and Abu Madi 2 wells located in the Nile delta, from Ramadan, 1990.

- *Burial anomaly derived from Athy-Curves*

The comparison between the constructed Athy curves and the “standard” curves from the B1T model (Limberger et al., 2017), are not meant to determine the true depth these sediments have been buried at. However, this approach allows us to give an indication of how much, in a relative sense, burial anomaly occurred at a given sedimentary basin. In order to derive the true amount of burial anomaly that occurred, more research is required.

When comparing the estimated burial anomaly chance indicator with burial depth studies in the literature, we observe that our analysis results are largely supported by the findings from the literature. These results show that estimating a relative burial anomaly based on Porosity-depth measurements yields acceptable results. However, as briefly mentioned in the “Muglad” sub-section, different parts of the basin could have experienced slightly different burial histories. Therefore, it is still important to consider inter-basin differences when performing this kind of analysis.

- *Potential burial anomalies at lower depths*

Sediments located deeper than the measurement depth, could theoretically have been subjected to a larger burial anomaly than the layers above. Therefore, caution is advised for extrapolating porosity values to depths deeper than the measurement depths, as these values could be (significantly) lower than expected. This could occur when a basin is subjected to at least two phases of subsidence with sedimentation separated by a phase of uplift in between.

In the instance of multiple reservoirs with different burial histories, it could mean that the constructed porosity-depth relationship for a particular basin is an average of two different relationships. However, the data observed is insufficient to clearly distinguish such effects if they are present.

- *Method reasoning/justification*

There are two reasons for constructing Porosity-depth relationships based on porosity data originating from reservoir rocks. The first is to determine if the available Porosity-depth measurements could indicate the presence of a burial anomaly in a basin. The second reason is to constrain reasonable porosity-depth relationship estimates that can extrapolate reservoir porosity values to different depths.

In the context of geothermal energy, it is important to determine if there is evidence for the presence of a burial anomaly as these general indicate reduced porosity values which in turn could indicate reduced permeability values, thus indicating a lower geothermal potential of a basin than expected. The second reason is important as in most cases, the reservoir geometry and reservoir depth are poorly constrained. Given that these reservoir parameters are not studied in detail for some areas, it would be beneficial for our numerical analysis to be able to project “hypothetical” aquifers at different depths to determine aquiver depth ranges where geothermal exploitation would still be beneficial. This approach, therefore, provides constraints on the feasibility of geothermal energy exploitation at a given depths. This narrows down the region of interest for future local studies that focus on more precise mapping of the geothermal energy potential of a given basin.

- *Data scarcity*

One of the key underlying limitations of this research is the relative scarce amount of data on which the analysis is based. As mentioned in the previous work of Hofstra (2022), the geoscientific data quality, coverage and availability is very inhomogeneous for different countries in Africa. The porosity-depth measurements are no exception. The analysis is based on the publicly available data, that undoubtably, is incomplete. In order to extrapolate and be able to say as much as possible, within reason, about the geothermal potential of a given basin, we had to make the assumptions described in the methods section. It is very likely that local governments and private oil and gas companies are in the possession of data that could either support or contradict our results. Despite this limitation, our analysis should be considered as the best possible porosity-depth estimation based on the available data.

However, as shown in Figure 15, large parts of Northwest, South-central and East Africa don't have sufficient data to construct local porosity-depth relationships. This means that the Athy-parameter values assigned to these regions is based on the continental average of all constructed porosity-depth relationships. Therefore, one should be critical when assessing these values given that the majority of the basins are unique in terms of their age, type and formation history. In most places, these values should be considered as placeholders that should be updated when new information becomes available.

- *Assumptions and inherent conclusion*

It is important to note that these porosity-depth curves do not represent the "true" porosity-depth relationship of the sedimentary basin. This is because the estimations are based on the relatively permeable reservoir rocks and do not account for other (less porous) layers in the stratigraphy. For this reason, the reservoir porosity-depth relationship will likely be an overestimation of the true porosity-depth relationship over the whole basin. This will have consequences for the gravity response of the subsurface, as higher porosity rocks have lower overall densities compared to their less porous counterparts and will therefore have a lower gravitational response. This mass deficit in turn could be compensated by higher densities in the upper crustal basement rocks and/or by decreasing the sediment-basement depth. This subsequently would result in an underestimation of the sediment thickness of a particular basin and therefore could result in an underestimate of the geothermal resource potential.

Furthermore, it's important to be critical about the Athy-parameters chosen for the given data points available. Most of these curves are based on data of a single reservoir (study). The depths of the measurements from these studies tent to be limited to depth ranges smaller than several hundred meters. Thus, we have to acknowledge that the curves represent the best guess of the porosity-depth relationship based on the available reservoir data.

For the porosity-depth relationships constructed based on multiple different reservoirs (i.e. Doba, Doseo, Ghadames, Illizi), the previously mentioned notes also hold true. In addition, it is also important to acknowledge that the lithologies of the reservoirs are likely not identical. For minor changes in lithologies however, i.e. clay-rich vs clay-poor sandstone, the Porosity-depth relationship does not change significantly (B1T, Limberger et al., 2017). However, the difference between typical clastic shales and typical sandstones are considerable (Figure 42) (B1T, Limberger et al., 2017).

Given that the majority of the clastic reservoirs considered are sandstones, in addition to the scarcity of and relatively large errors of the data, we decided to describe the differences between porosity-depth relationships with an emphasis on extra burial depth (burial anomaly) rather than significant lithological changes. However, by comparing our estimates with typical values from the B1T model (Limberger et al., 2017), it could be possible to speculate on the "purity" of the sandstone reservoirs studied. Arguably, it would be difficult to distinguish the lithological component from the burial anomaly component from these graphs, especially given the data scarcity.

Input parameters sediments

	Rock Type	Rock Type
SELECT rock type	Clastic_Sediments_Shale	Clastic_Sediments_Sandstone
	Lithology	**Lithology**
SELECT lithology	typical	quartzite,typical
SELECTED rock type	Clastic_Sediments_Shale	Clastic_Sediments_Sandstone
SELECTED lithology	typical	quartzite,typical

	parameter	case a	case b
Rock matrix conductivity at 20 °C[3]	λ_{RMv20}	1.64	6.15
Anisotropy factor[3]	a_{λ}	1.6	1.08
Specific heat capacity (not used)[3]	Cp	860	890
Thermal sorting factor[3]	f	1.38	1
Density rock[3]	ρ_{sed}	2700	2640
Uranium content[3]	U	3.7	0.6
Thorium content[3]	Th	12	1.8
Potassium content[3]	K	2.7	0.9
Radiogenic heat production[3]	A_{sed}	2.03	0.36
Depositional porosity[3]	ϕ(0)	70	42
Athy depth factor[3]	k athy z	0.83	0.3
Athy pressure factor[3]	k athy P	0.09613	0.02726
Density water[3]	ρ_{water}	1078	1078

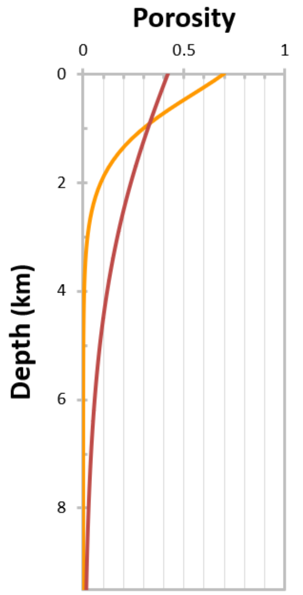

Figure 42: Porosity-depth relationships for typical shales (case a left) and typical sandstones (right). From B1T model (Limberger et al., 2017)

- *Omittance of limestone data*

Limestone porosity-depth relationships are generally more complex compared to clastic cases due to differences in their chemical stability and more complex grain shapes compared to clastic sediments (Ehrenberg & Nadeau, 2005). For this reason, we choose to not include carbonate reservoir data. This, however, does not mean that carbonate reservoirs are not suitable for geothermal energy exploitation. To the contrary, deep carbonate reservoirs might be some of the most important geothermal resources worldwide (e.g. Montanari et al., 2017; Homuth et al., 2015; Pasquale et al., 2014; Mohammadi et al., 2010; Gousmania et al., 2006; Simsek, 2003; Minissale and Duchi, 1988).

We conclude that our workflow of using Athy curves to describe porosity-depth relationships is not suitable for carbonate reservoirs and we therefore choose to omit this data. However, creating a workflow for determining of the geothermal energy potential of carbonate reservoirs, would be a very good idea for future research.

- *Does Porosity-depth data support the assumption of identical reservoir parameters?*

From Figure 27, we can observe that there is much difference between the estimated porosity-depth relationships of the sedimentary basins of Africa. At the surface and 3000 meters depth, the porosity ranges from approximately 25 to 45% and 2 to 25% respectively. Given that porosity is closely related to permeability (via for example the Kozeny-Carman equation; Kozeny (1927), Carman (1937)) and thus transmissivity, it is an important indicator for determining the (economic) feasibility of a geothermal energy system. The geothermal energy prospects for the low end of this range are not favourable whereas the prospects for the high end of this range are very promising.

Despite all assumptions and considering the fact the parts of Africa are not directly included in this analysis, we can conclude that assuming identical reservoir parameters for geothermal potential modelling is not supported by the available porosity-depth data.

Whilst it seems appealing to assume average reservoir parameter values, disregarding the issue of determining what a representative average value would be, this inherently will lead to overestimations at one place and underestimation at other places. Due to the financially driven incentives of geothermal energy exploitation, the development of geothermal systems hinges on threshold go/no-go values for reservoir parameters. If due to these under or overestimations these threshold values are or are not met, opportunities could be missed or be explored despite their economic infeasibility.

5.2. Gravity inversion

5.2.1. Sediment thickness maps

- Laske & Masters (2013)

Figure 43 shows the sediment thickness map of all the sub area inversion results stitched together onto the input sediment thickness map (left) and the combined sediment thickness input map based on the onshore results of Laske & Masters (2013) and the offshore results of Straume et al., (2019) (right).

From this Figure, we can observe that the onshore resolution of the sediment thickness map has increased significantly compared to the results of Laske & Masters (2013). Consequently, our results show more details and variations within the boundaries of a basin. Note that the offshore resolution of the inversion results is representative for the resolution of the input sediment thickness map rather than the highest resolution map of Straume et al., (2019). As stated previously, the maximum thickness of the inversion results is smaller than the sediment thickness derived by Laske & Masters (2013). Another clear addition of our results is the information on the geometry of basins in the East-African rift zone. These basins are generally too small to be shown in the results of Laske & Masters (2013) due to the resolution size (111km^2).

The differences between our results and the results of Laske & Masters (2013) are likely related to both the assumptions made in our inversion modeling and the fact that Laske & Masters (2013) inversion modeling is based on seismic wave velocities rather than the inferred density differences. Using seismic wave velocities allows for the differentiation between rock compositions with comparable densities. This is relevant for the sediment basement transition because the density of sediments that are buried close to the basement rocks might approach the upper crustal density values of the underlying basement. These rocks are therefore difficult to distinguish on the basis of density alone. This might therefore be the reason as to why the sediment thicknesses of Laske & Masters (2013) are deeper overall.

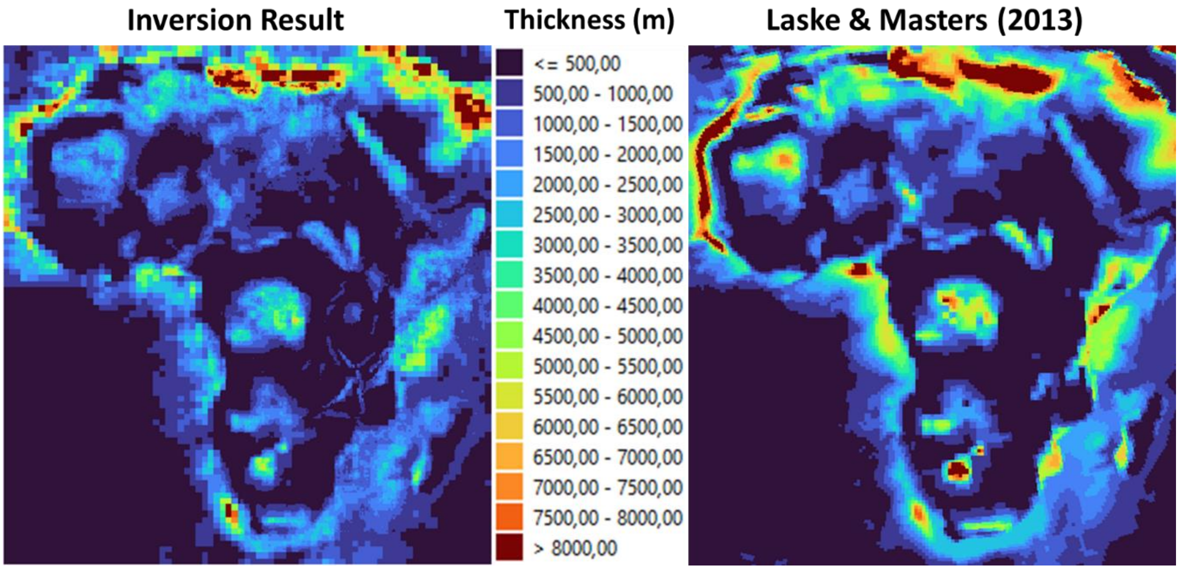

Figure 43: Stitched sediment thickness inversion results (left) Vs the sediment thickness results from Laske & Masters (2013) (right). Note that the "," is the decimal separator and should be read as ".".

- Cross-section validation

In this section, we compare our sediment thickness modelling results to publicly available cross-sections, to be able to validate our modelling results. Given the simplified nature of the model, and the overall continental scale of this research, we only evaluate larger scale geometries and features as basin geometry and sediment thickness rather than individual fault expressions.

- **Bongor & Doseo**

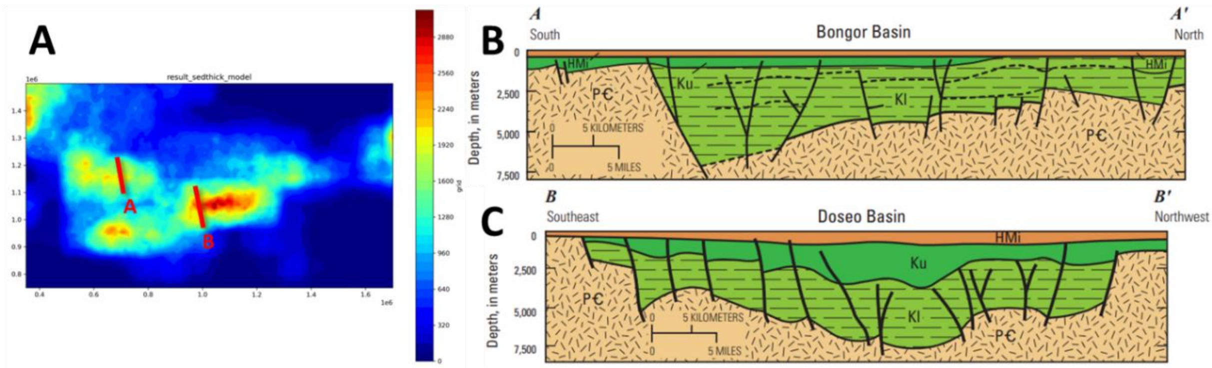

Figure 44A: Sediment thickness map of the Central African Rift zone sub-area (i.e. Bongor, Doba, Doseo). The red lines indicate the locations of the cross-sections shown in panels B and C (A and B respectively). B/C: Seismic based cross-sections for the Bongor and Doseo basins respectively, from Brownfield et al., 2011.

Figure 44A, shows the sediment thickness map of the Central African Rift zone sub-area model. Figure 44B/C, shows the geological cross-sections for the Bongor and Doseo basins respectively (Brownfield et al., 2011). If we compare our results to the cross-sections from Brownfield et al. (2011), we observe that we derive significantly lower sediment thicknesses for these basins. Our results show maximum thicknesses that exceed 2500 meters in the central part of the Doseo basin, whereas Brownfield et al. (2011), derives thicknesses approaching 7500 meters. However, in the context of our simplified model, we find comparable basin geometries. Note that our derived sediment thickness is very comparable to the sediment thickness of the prior model based on the work of Laske & Masters (2013). This discrepancy could thus potentially be explained by "errors" in the prior model due to its lower resolution origin.

- **East Niger**

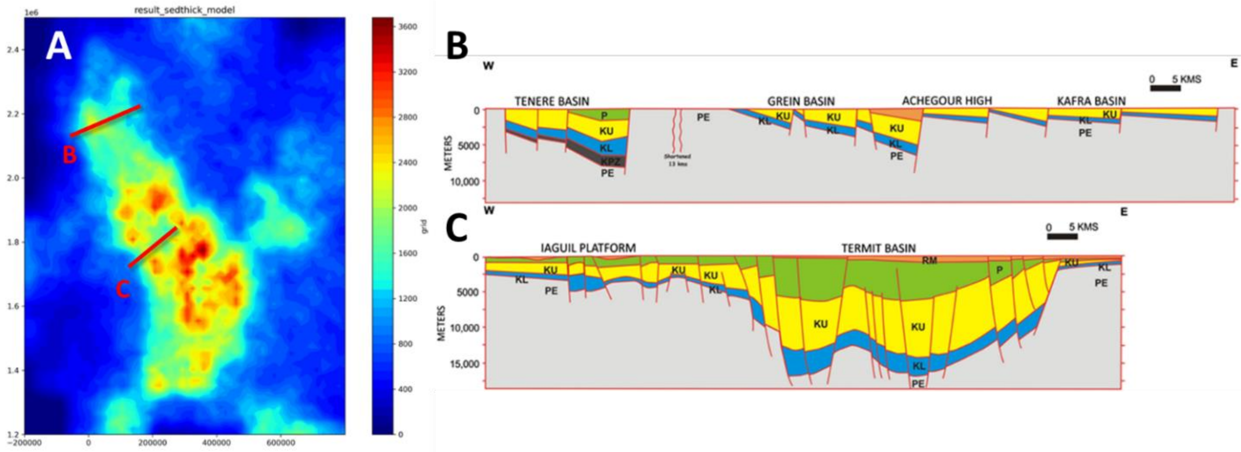

Figure 45A: Sediment thickness map of the Termit/East Niger sub-area (i.e. Termit, Tenere, Grein, Kafra). The red lines indicate the locations of the cross-sections shown in panels B and C. B/C: Seismic based cross-sections for the East Niger basins, from Ahmed et al., 2020.

Figure 45A, shows the sediment thickness map of the East Niger/Termit sub-area model. Figure 45B/C, shows the geological cross-sections of the East Niger basins (Ahmed et al., 2020). If we compare our results with the cross-sections of Ahmed et al. (2020), we observe that we derive significantly lower sediment thicknesses. We derive a maximum thickness of approximately 3600 meters in the central part of the Termit basin, which is a five-fold decrease compared to the maximum thickness derived by Ahmed et al. (2020). Additionally, our maximum thickness is also approximately a two-fold decrease compared to the thicknesses of the prior model based on the work of Laske & Masters (2013). Furthermore, the basin geometry derived also deviates strongly from the geometry described by the cross-sections. The deviations in geometry could partly be attributed to poor geological constrains due to the poor resolution of the prior model, whereas the deviations in sediment thicknesses could also be attributed to density assumptions and our simplified model.

- **Horn of Africa**

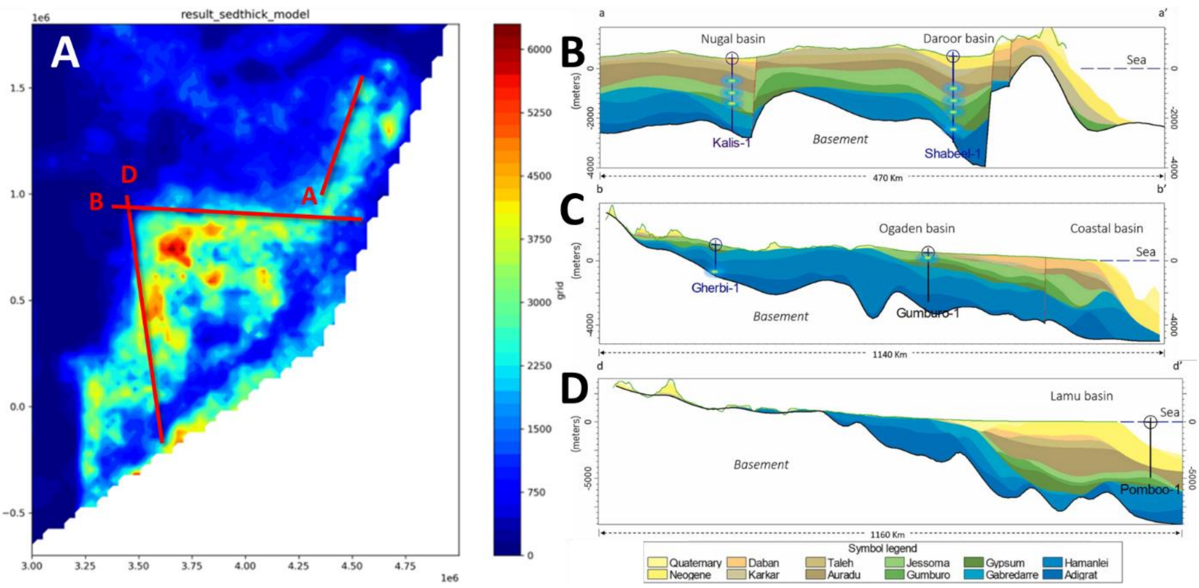

Figure 46A: Sediment thickness map of the Horn of Africa sub-area (i.e. Nugal, Daroor, Ogaden, Lamu). The red lines indicate the locations of the cross-sections shown in panels B-D (B=A, C=B, D=D). B-D: Modelled cross-sections based on wells logs for the basins in the Horn of Africa, from Quiroga et al., 2022.

Figure 46A, shows the sediment thickness map of the Horn of Africa sub-area model. Figure 46B-D, shows the geological cross-sections of the basins in the Horn of Africa (Quiroga et al., 2022). If we compare our results to the cross-sections of Quiroga et al. (2022), we approximately derive similar sediment thicknesses for all three cross-sections. However, the onshore-offshore transition zone is the exception. Here we observe an overall sediment thickness decrease that is not present in the cross-sections. Additionally, we have to note that derived maximum thicknesses are significantly smaller compared to the prior model based on the work of Laske & Masters (2013). If we compare the derived basin geometries with the cross-sections, we observe both similarities as medium deviations. Overall, given the simplifications and assumptions of our model, we argue that the cross-sections of Quiroga et al. (2022), do not contradict our results. The onshore-offshore transition zone discrepancies are likely, to be related to our difficulty in modelling the offshore (more on this in the section 5.2.3.).

- **Illumeden**

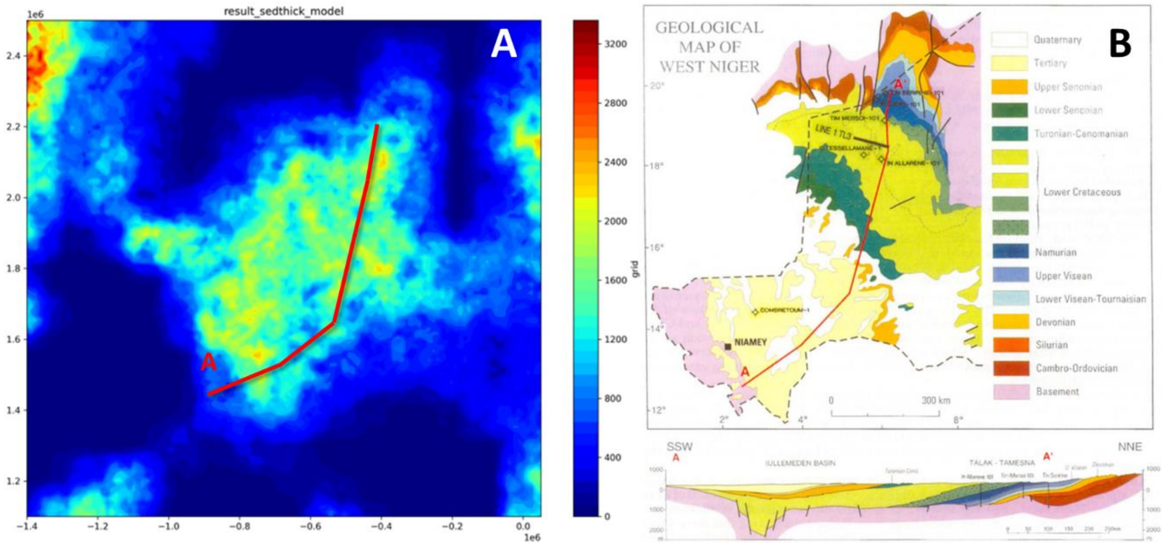

Figure 47A: Sediment thickness map of the Illumeden sub-area. The red line indicates the location of the cross-section shown in B. B: geological map of West Niger and geological cross-section of the Illumeden basin (top and bottom respectively), from Zanguina et al., 1998.

Figure 47A, shows the sediment thickness map of the Illumeden sub-area model. Figure 47B, shows the geological map and cross-sections of the Illumeden basins (Zanguina et al., 1998). If we compare our results to the cross-section of Zanguina et al. (1998), we derive marginally larger sediment thicknesses along the cross-section line. Their average thickness exceeds approximately 1000-1200 meters with a maximum thickness of approximately 2000 meters. We find average thicknesses around 1600 meters, exceeding 2000 meters in some places. These thicknesses are in the same range as the ones from the prior model. The geometry of our model is very similar and does therefor not contradict the results of Zanguina et al., 1998.

- **Muglad & Melut**

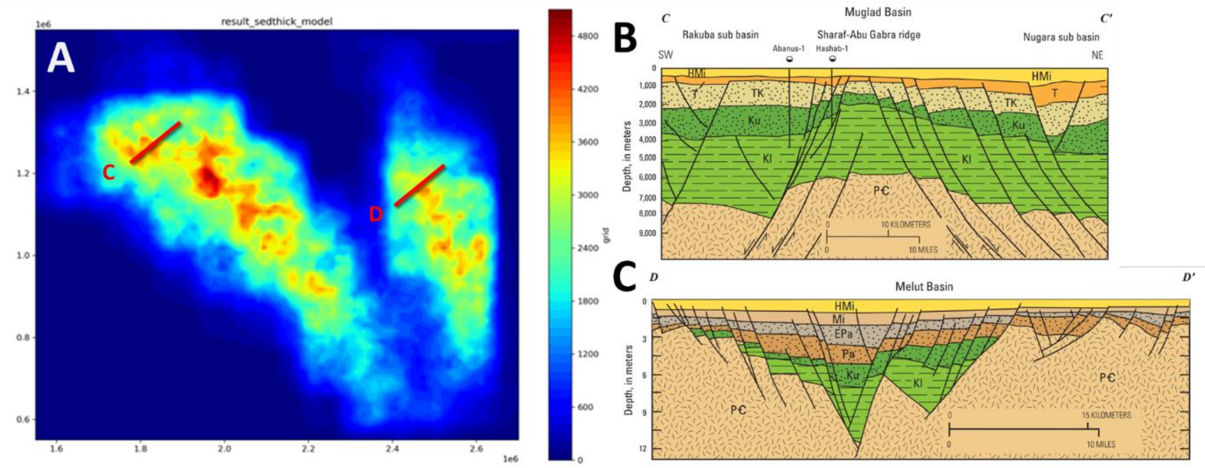

Figure 48A: Sediment thickness map of the Muglad & Melut sub-area. The red lines indicate the locations of the cross-sections shown in panels B and C (C and D respectively). B/C: Seismic based cross-sections for the Muglad and Melut basins respectively, from Brownfield et al., 2011.

Figure 48A, shows the sediment thickness map of the Muglad & Melut sub-area model. Figure 48B/C, shows the geological cross-sections for the Muglad and Melut basins respectively (Brownfield et al., 2011). If we compare our results to the cross-sections from Brownfield et al. (2011), we observe that we derive significantly lower sediment thicknesses for these basins. Brownfield et al. (2011), shows thicknesses for both basins that in some places far exceed 6000 meters in depth, whereas we find that the deepest part of the Muglad and Melut basins are approximately 4800 meters and 3800 meters respectively. Note however, that the prior model shows thicknesses that do not exceed 6000 meters, suggesting that there is also discrepancy between Laske & Masters (2013) and Brownfield (2011). Additionally, the derived basins geometry does not show the horst and graben structures that are shown in the cross-sections. The discrepancies in depth could possibly be explained by density assumptions and the simple nature of the model. The geometry differences are in large part likely caused by the relatively poor resolution of the prior model of Laske & Masters (2013).

- **Saharan platform**

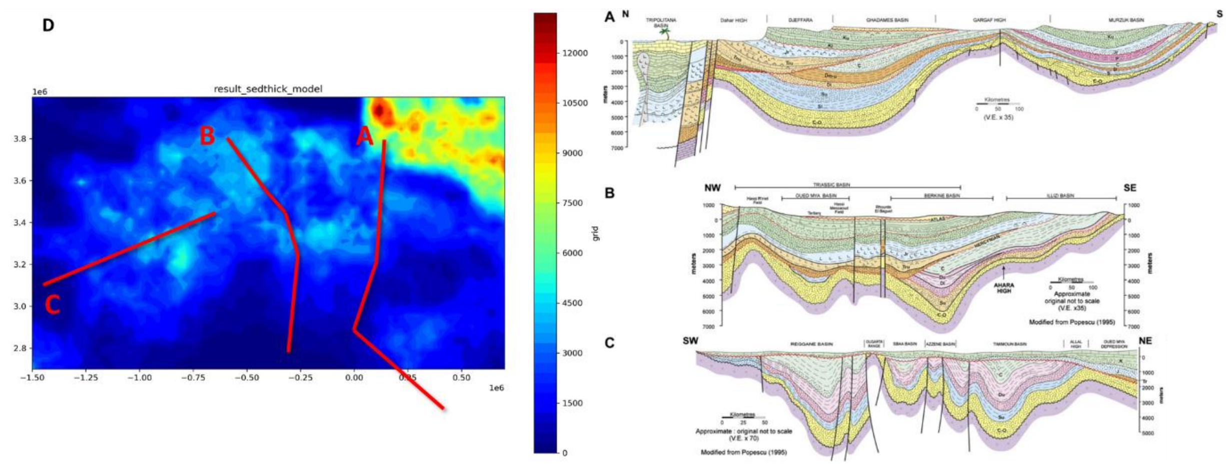

Figure 49A-C: Seismic based geological cross-sections along different parts of the Saharan platform, from Galeazzi et al. 2010. D: Sediment thickness map of the N-Algeria sub-area. The locations of the cross-sections shown in panels A-C are indicated by the red lines.

Figure 49D, shows the sediment thickness map of the N-Algeria sub-area model. Figure 49A-C, shows the geological cross-sections for the different basins in the Saharan platform (Galeazzi et al. 2010). If we compare our results to the cross-sections of Galeazzi et al. (2010), we find that our model shows overall smaller sediment thicknesses along the cross-section lines. At some places this discrepancy is less than 500 meters, but at other places this discrepancy can exceed 1500 meters. The discrepancy between the geometry of our model and the cross-sections varies per cross-section. Cross-section A shows a comparable geometry to our model but the discrepancy between our model and the other cross-sections is much larger. This area is characterised by the large number of basins that are located in close proximity to each other. These individual basin geometries are hard to distinguish in this model, likely due to the relatively loose constrains imposed on the model during the data assimilation part of the inversion modelling. The large sediment thickness of and the modelling problems of the offshore area likely complicate these results. This sub-area is also one of the largest, resulting the loss details and nuances on the smaller scales.

- **Taoudeni**

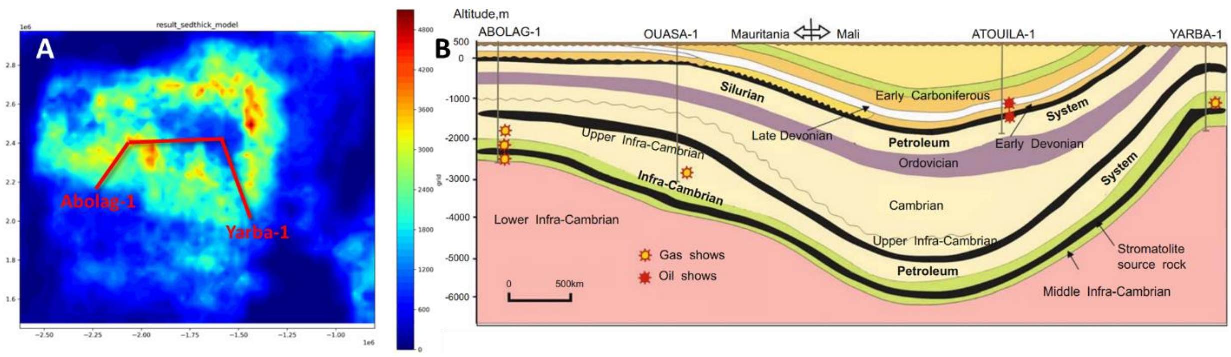

Figure 50A: Sediment thickness map of the Taoudeni basin. The red line indicates the location of the cross-section shown in panel B. The well names shown are meant to illustrate the direction of the cross-section. 49B: shows a geological cross-section of the Tauodeni basin derived from well listed in the figure, from Huang et al., 2008.

Figure 50A, shows the sediment thickness map of the Taoudeni sub-area model. Figure 50B shows the geological cross-section of the Taoudeni basin (Huang et al., 2008). If we compare our results to the cross-section of Huang et al. (2008), we can conclude that both our basin geometry and sediment thickness show large discrepancies along the cross-section line. The small sediment thicknesses in the centre of the basin in our model is one of the largest discrepancies between the two models. It is important to note that this result is also in stark contrast with the geometry and depth of the prior model. Our model appears to have inverted the deep and shallow parts of the basin, in addition to significantly decreasing the overall sediment thickness. It could be that during the inversion modelling, the “wrong” minimalization solution is found. This could potentially be due to relatively lose geological constrains during the modelling process.

- Crustal density

Figure 22 shows the crustal density under the Zaire basin. While the Basin3D interface doesn’t show a clear legend, we can observe that the upper crustal density values under the Zaire basin approach values of the mantle density below. Here we also observe that the upper crustal density values exceed the lower crustal density values. Note that this effect is significantly weaker on the sides of the basin where the sediment thickness is smaller.

The significant increase in upper crustal density is to be expected given the fact that we allowed to upper crustal density to vary whereas the lower crustal and mantle density values remain the same. We have to acknowledge that this result is contrary to what you would expect from the density variation with depth according to the PREM model (Dziewonski & Anderson, 1981). However, this is intentional, given that we are only interested in modelling the basins in Africa rather than the crust and mantle system as a whole. By varying the upper crustal density, we aimed to filter out the long wavelength gravity signals, allowing us to model the short wavelength (basin) signals.

However, when only accounting for the long wavelength structures you would expect that the increase in upper crustal density would be more uniform over the crust rather than to be concentrated under the deepest parts of the basins. These lateral differences in density could potentially be explained by the presence of crustal density heterogeneities or by isostacy effects (Watts, 2001). However, it is unclear if allowing the lower crustal and mantle densities to vary (within reason) in an addition to the upper crustal density, would result in a more homogeneous distribution of these effects throughout the crust. This could potentially also help to partly explain the thinner sediment thicknesses obtained from our modelling compared to the results of Laske & Masters (2013).

When considering the density distribution of the SE rift system sub-areas (Figure 50), we observe that the upper crustal density is significantly lower compared to the density of the lower crust and the mantle. Here we therefore observe that the best fitting solution favoured the overall decrease of the crustal density in instead of the increase observed in the other sub-areas. This suggests that there is a mass excess in the SE rift system with the assumed initial sediment thicknesses. This is likely due to the relatively thin initial sedimentary thickness that is assumed in the prior model. This hypothesis is supported by the seismic cross-sections from Wright et al. (2020) and Tiercelin et al. (2012), that indicate sediment thicknesses significantly larger than 2000 meters for the Tanganyika and Lokichar basins respectively. The inversion algorithm largely compensates this by significantly decreasing the upper crustal densities rather than making large changes in sediment thickness. This might be explained by a larger sensitivity to density variations compared to sediment thickness changes. This might be an unintended bias of the algorithm, but exploring this hypothesis is beyond the scope of this analysis.

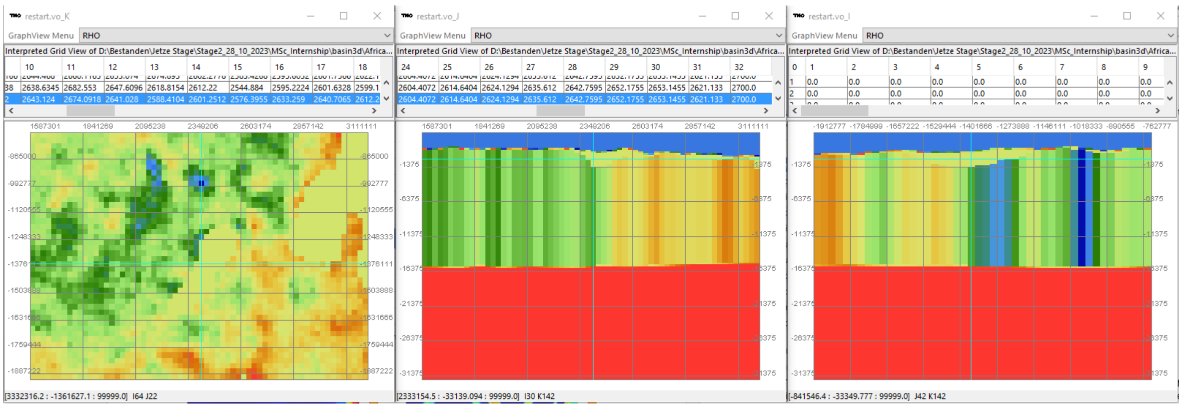

Figure 51: Crustal density distribution SE African rift zone basins. From left to right: Map view, N-S cross-section, E-W cross-section.

5.2.2. Parameter Study

- Sensitivity of input parameters

As seen in Figure 24, changes in input parameters do not significantly change the fit between the observed and the modelled values. This would suggest that the effect of one these input parameters is not very significant in fitting the gravity anomaly observations to the satellite gravity data. The effects of changing these parameters is largely compensated by changes in either sediment thickness and/or upper crustal densities.

However, from Figure 25, we can observe that changing some input parameters does have a noticeable effect on the geometry of the sedimentary basin. The largest change is observed when assigning an arbitrary starting depth to the sedimentary-basement interface (Figure 25D). This is no surprise given that this input parameter changes this starting condition of the prior model, resulting in an optimum end that does not resemble the shape of the Zaire basin. This run highlights the non-uniqueness nature of this geoscientific problem.

The remaining parameter runs can be assigned in two categories based on their respective maximum sediment thickness. Run T can be considered an outlier to these categories. The first category is composed of runs A-C, E-J, M and Q-R, with maximum sediment thicknesses ranging from 6700 to approximately 7200 meters. This category includes run B with the standard settings used in the inversion modelling. We can therefore conclude that changing these parameters does not change the sediment thickness of the Zaire basin very much.

Category two is composed of the remaining runs K, L, N, O , P, S (excluding T), with lower maximum sedimentary thicknesses ranging from 6000 to 6500 meters. From parameter runs K and L, we can observe that increasing the base porosity from 0 to higher values, the program obtains a lower maximum sedimentary thickness compared to the standard results. This outcome is not surprising, given that a higher base porosity results in a lower gravity contribution of the sediments that requires to be compensated by a larger volume of crustal rocks with higher densities.

Increasing the crustal density variation range also decreases the derived maximum sedimentary thickness of the basin. This also suggests that the crustal density is a major component in fitting the observed gravity anomaly with the modelled gravity anomaly.

Surprisingly, either decreasing or increasing the crustal density variation cell range, decreases the maximum sedimentary thickness of the basin. It is not clear why that is the case, these results could potentially be a low and a high-end results of the random path taken by the data assimilation.

However, increasing the sediment thickness variation cell range does decrease the maximum sediment thickness. In the case of parameter run T, this effect is even more significant. It is unclear why changing these parameters effects the results this much.

We can conclude that overall changing these input parameters does not have a significant effect on the fitting of the observations to the modelled gravity anomaly values. However, some parameters as base porosity, crustal density variation range and the crustal density variation and sediment variation cell range seem to have an effect on the obtained sediment thickness of the inversion modelling. The strongest influence on the geometry and depth of the sedimentary thickness is the sediment-basement interface depth.

- Effect of the number of MDA

From Figure 26, we observe that by increasing the number of MDA, the fit between the observed and the modelled gravity anomaly increases significantly. Despite this increase in fit, some outliers of significantly lower modelled values compared to the observed values persists. We also observe that the deepest parts of the basin become shallower and more connected with increasing MDA. The sediment-basement interface thus becomes more smooth with less irregular variation.

These parameter runs show us that the number of MDA is the strongest parameter for obtaining better fitting results. This is not very surprising given that for each extra MDA run, the results are getting closer to an optimum result. Based on these results, we can conclude that using 4MDA yields the best results for these complex problems.

- Input parameter estimates

In this section we want to briefly comment on a few seemingly arbitrary input parameters as the layer model used, the sediment and the DA parameters.

1) Layer model (geometry and parameters)

Our layer models as described in the methods section, is very much a rough simplification of reality. However, given the scope and objectives of this research we argue that these assumptions in geometry are justified. The density values of the mantle and crustal layers is based on the values listed in Hantschel & Kauerauf (2009). These values are in line with the Earth crustal model 1, created from the analysis performed by Mooney et al. (2023). The findings from Reguzzoni & Sampietro (2015) based on satellite data, also support the density values used in this analysis.

2) Sediment parameters

The assumed surface porosity of 41%, is on the high-end for the derived Athy-curves based on porosity-depth measurements. However, based on the B1T model (Limberger et al., 2017), this value is in between the value of clay-rich sandstones (40%) and the value for clay-poor sandstones (42%). Additionally, from the parameter study we concluded that changes in surface porosity do not significantly impact the inversion modelling results.

The sediments are assumed to have an initial bulk density of 2600 kg/m^3, this value is relatively low compared to the range of density values listed for sandstones in Hantschel & Kauerauf (2009). However, the density values of shale listed in Hantschel & Kauerauf (2009), are generally lower than 2600 kg/m^3. As we assumed that the sediments are a mixture of clastic sandstones and shales, we argue that this value is justified. Furthermore, in the parameter study, we concluded that changes in sediment density only result in minor changes in the inversion modelling outcome.

In our modelling, we assumed that the porosity of the sediments would be reduced to the base porosity of 0 at the depth of 3000 meters. This assumption is not support by our results from the porosity-depth relationships. However, we decided to do this to compensate for the apparent mass deficit of our model as observed from the decreased sediment thicknesses compared to the results from Laske & Masters (2013) and the relatively high upper crustal density values. Modelling a more accurate mantle and crustal layer model is time-intensive and arguably beyond the scope of this research and we therefore choose to compensate using these parameters. The parameter study results also suggest that higher base porosities result in significantly lower sediment thicknesses compared to both the default modelling run in addition to the results of Laske & Masters (2013).

3) DA parameters

During the data assimilation we allow for the sediment thickness to be reduced to 10 percent and to be increased to 200 percent of its initial value. Additionally, we allow the upper crustal density to vary ± 20%. This results in upper crustal density values that range from 2160 to 3240 kg/m^3, which for the high end is in the range of possibilities according to the results of Mooney et al. (2023) and Reguzzoni & Sampietro (2015). The lower end of this is far too low compared to the overlying sediments with an estimated density of 2600 kg/m^3, whereas the upper limit approaches mantle density values. Our results, however, show that the upper crustal density values often significantly trend towards the high end of this spectrum, under the sedimentary basin locations. This suggests that our model contains a mass deficit under the sedimentary basins.

5.2.3. Assumptions & Limitations

- Off-shore modelling errors

During the modelling of passive margin basins and basin located close to the onshore-offshore transition, we observed that the model datapoints located at the offshore and the onshore transition zone, showed significantly large residuals when comparing to the observation data. This discrepancy between the modelled values and the observed gravity anomaly values often exceeds the six standard deviation limit imposed by the program (Figure 51-52). We therefore choose to exclude these measurements for modelling the onshore basins of Africa. This decision is also based on the fact that exploited geothermal heat cannot be transported feasibly over long distances due to the significant heat loss during transport. Offshore geothermal prospects are generally considered not be profitable and are therefore not modelled in this study. However, assuming that the gravity signal is of equal quality for both the onshore and the offshore, we must conclude that our model for the offshore is not very accurate. Given that most of the residuals that exceed the six standard deviations limit in the negative domain, we can conclude that the offshore model most likely contains a mass deficit. This can possibly be explained by the simplification of our model, where we do not differentiate between continental and oceanic crust in terms of geological properties. And given that the oceanic crust is thinner than the continental crust, this will result in a mass deficit in the offshore area. This simplification is unlikely be a problem given that we are not interested in creating a new sediment thickness map for the offshore given that the resolution of these sediment thickness maps is already detailed (Straume et al., 2019). Also, potential problems that could arise for the basins located near the offshore due to this simplification are likely long wavelength signals that are compensated for by the variation in upper crustal density values.

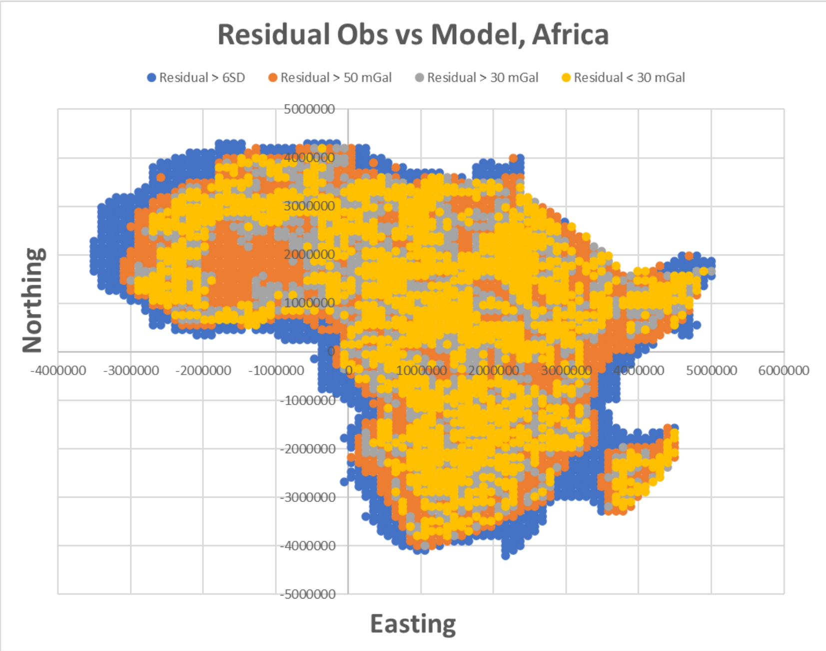

Figure 51: Residual gravity anomaly of the MDA1 continental Africa sub-area run.

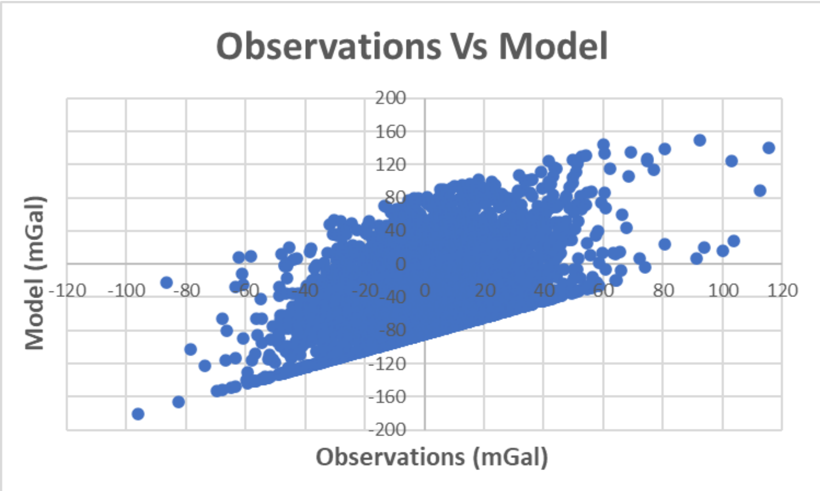

Figure 52: Gravity anomaly data plotted modelled values (y-axis) vs the observation values (x-axis).

- Projection and resampling errors

During the preprocessing of the data, we had to reproject the geospatial data from latitude/longitude coordinates to UTM projections in order for Basin3D to be able to read the input ascii-files. During the reprojecting of geospatial data, the number and location of the datapoints is changed. The new values that are assigned to these datapoints can be obtained using different averaging techniques. Consequently, this does mean that the original data is altered slightly which could introduce errors in the data. However, given the scope of our analysis, the simplification of our model and the limited number of reprojections, these introduced errors are relatively small and can therefore be ignored.

Something else to consider is that perfectly projecting a rectangular shape onto a sphere is difficult. However, converting data from a latitude/longitude projection to a UTM-zone projection does essentially do this. The projection is centred around a N-S line with minor distortion when using a transverse Mercator projection. This distortion increases with increasing distance from this middle line (Bertici et al., 2014). For smaller UTM zones, that are suitable for the projection of smaller areas, these distortions remain minor. However, considering that we attempt to project entire continental Africa, which covers multiple different UTM-zones onto different hemispheres, we can assume that the distortion in the data is considerable. In our analysis, we choose the UTM 33N projection as this projection results in the least amount of distortion overall. These distortions will affect the visualisation of the results rather than the calculation of said results.

- Overfitting

As shown in the parameter study on the number of MDA used in the inversion modelling, we observed that increasing the amount of MDA yield better fitting results. However, one should be careful with increasing the MDA beyond a particular amount. This is due to the concept of overfitting which is common for minimization algorithms used in inversion modelling (Oldenburg & Li, 2005). This problem arises from imperfect observation data and the simplification of often complex modelling problems. Both are very much present in basin modelling and geosciences as a whole.

The inversion fitting algorithm aims to fit the modelled values as closely as possible to the observed data constrained by parameters and their respective variation ranges. However, the observation data has errors/induced noise due to the measurement equipment. This results in the fitting of the noise in the data past a certain amount of multiple data assimilations.

Additionally, the simplification of the model also introduces a limit on how accurate the reality can be modelled. By isolating the values that you want to model you have to do concessions on other contributing parameters. It, therefore, does not make sense strive for a marginally better fit after a certain amount of MDA, as the results will start to deviate again from reality to better fit the simplified model.

Both difficulties are present in our inversion modelling of a simplified geometry of the sedimentary basins of Africa. Aside from the error in the satellite data, we have to acknowledge the simplified crustal model that we use in our inversion modelling. For example, the multiple sedimentary layers with unique geometries and other geological parameters that compose a sedimentary basin are averaged into one layer in our model. This assumption disregards potential gravity signal variations within a basin resulting in underestimations in one place and overestimations in other places.

Given the errors in observation data and the simplified nature of the model, we conclude that using a higher number of MDA than 4 will likely result in the overfitting of the data. It could be argued that the results of the MDA4 inversion runs could potentially already have been subjected to overfitting. However, this statement is hard to verify without more statistical analysis which is beyond the scope of this project.

6. Conclusions

6.1. This study

In this MSc thesis project as part of the GAA, we improved upon the new basin model and its database for the sedimentary basins of Africa (Hofstra, 2022). We did this by expanding the data-quality based classification and by incorporating more precise, observation-based porosity-depth measurements for the sedimentary basins of Africa. Based on this improved database, we estimated porosity-depth relationships for the sedimentary basins of Africa, in order to be able to extrapolate reservoir properties to deeper and shallower levels. These results are subsequently validated by burial history literature and provide constrains on the identical reservoir parameter assumptions made by previous studies. These results are subsequently used in the modelling of the geothermal energy potential of Africa by the colleagues of TNO.

Furthermore, using an inversion modelling workflow, we created a sediment thickness map for continental Africa with a resolution of 25km. These results are of a higher resolution compared to the currently highest resolution and publicly available data from Laske & Masters (2013). Our results provide constrains on the sediment thicknesses of the basins in Africa, which is important information required for low-enthalpy geothermal energy potential modelling. These modelling results are validated by seismic and geological cross-sections, to evaluate their respective geological accuracy. The sensitivity of the modelling parameters is evaluated via a detailed parameter study, which highlights the most influential parameters for the inversion modelling of sedimentary basins.

The efforts of this study and the GAA as a whole, are an important first step in creating a continental scale database for Africa on the topic of geothermal energy, in addition to providing a first order geothermal energy potential resource estimation. Despite the limitations and assumptions made in this analysis, the results provide a good starting point for future geothermal exploration endeavours in continental Africa.

6.2. Improvements & Future Work

The results of this research are part of the first order estimation of geothermal energy resources of the sedimentary basins of Africa as part of the larger GAA project. These results should therefore, be considered as best possible estimates given the limitations and assumptions made in this analysis. However, it is apparent that much work still needs to be done to accurately determine the geothermal potential of the sedimentary basins of Africa. We therefore like to give some suggestions on how our analysis and therefore our results can be validated and be improved upon.

One way of improving the geothermal resource estimates would be by incorporating more Porosity-depth data for different reservoirs at different depths in the Athy-curve estimations. Preferably, in basins with relatively little publicly available data. This could be done by either including previously not accessible datasets in the possession of private companies and governmental institutions, or by obtaining more data via core analysis of new and old drilled cores. Furthermore, special attention should be dedicated to the collection and the development of porosity-depth estimation methods of carbonate reservoir data. Incorporating carbonate reservoir data in this analysis would be a necessary and worthwhile addition. Lastly, incorporating direct permeability measurements rather than porosity data in this analysis would reduce and/or validate one of the key assumptions in deriving geothermal potential estimates from the porosity of reservoir rocks.

In addition to improvements to the reservoir database, the results of the inversion modelling would also benefit from improvements in input data and software in addition to more (local) studies that could validate the results. Currently, the Basin3D code only allows for the depth variation of one layer during the data assimilation. Writing code that could allow for variation of multiple layers could potentially be used to model local variation within the basin improving the modelling of smaller wavelength structures. More specifically, this would allow for more accurate reservoir geometry modelling, reducing geothermal exploitation risk. However, improvements in the prior model that the longer wavelength, could also improve the basin modelling. These improvements could include a better offshore model, higher resolution input data and the incorporation of detailed local maps obtained from gravity inversion to the input data. Lastly, improvements in code efficiency and computing power, could allow for higher resolution models and therefore more accurate resource estimates.

7. Acknowledgements

Special thanks to my supervisors Fred Beekman and Jan-Diederik van Wees for their active guidance, patience, good ideas and overall support throughout this project. In addition, I would like to thank Jan-Diederik van Wees and Job Mos for the technical support during the Basin3D modelling and python programming parts of the project. I also would like to thank Hans Veldkamp for his help on the data formatting and GIS related issues that I encountered during my time at TNO. Marianne van Unen has also been an invaluable partner in constructing the porosity-depth relationships for the sedimentary basins in Africa.

Lastly, I would like to thank the “colleagues” and especially the other interns for making my time at TNO as enjoyable as possible. Without them, some breaks would have been shorter, and parts of the day would have been slightly more productive. However, their presence has been an invaluable part of my experience of working at TNO.

8. References

8.1. Literature

Ahlbrandt, Thomas S. The sirte basin province of Libya: sirte-zelten total petroleum system. Vol. 2002. US Department of the Interior, US Geological Survey, 2001.

Ahmed, Kabir Shola, et al. "Anatomy of Eastern Niger Rift Basin with Specific References of Its Petroleum Systems." International Journal of Geosciences 11.5 (2020): 305-324.

Ali, M. Y., and J. H. Lee. "Petroleum geology of the Nogal Basin and surrounding area, Northern Somalia, Part 2: hydrocarbon potential." Journal of Petroleum Geology 42.3 (2019): 233-260.

Athy, Lawrence Ferdinand. "Density, porosity, and compaction of sedimentary rocks." Aapg Bulletin 14.1 (1930): 1-24.

Balling, Niels, and Svend Saxov. "Low enthalpy geothermal energy resources in Denmark." *pure and applied geophysics* 117 (1978): 205-212.

Barkaoui, A. E., et al. "Progress in understanding the geothermal sedimentary basins in northeastern Morocco." Journal of African Earth Sciences 97 (2014): 1-8.

Bertici, R., et al. "Comparative analysis of Mercator and UTM map projections." Research Journal of Agricultural Science 46.2 (2014).

Bhattacharyya, B. K. "Some general properties of potential fields in space and frequency domain: a review." *Geoexploration* 5.3 (1967): 127-143.

Blakely, Richard J. *Potential theory in gravity and magnetic applications*. Cambridge university press, 1996.

Blom, Nienke. (2018). Inverse theory (chapter 2 of Nienke Blom's PhD thesis).

Brownfield, M.E., Klett, T.R., Schenk, C.J., Charpentier, R.R., Cook, T.A., Pollastro, R.M., and Tennyson, M.E., 2011, Assessment of undiscovered oil and gas resources of the Sud Province, north-central Africa: U.S. Geological Survey Fact Sheet 2011–3029, 4 p.

Caratori Tontini, F., L. Cocchi, and C. Carmisciano. "Rapid 3-D forward model of potential fields with application to the Palinuro Seamount magnetic anomaly (southern Tyrrhenian Sea, Italy)." *Journal of Geophysical Research: Solid Earth* 114.B2 (2009).

P.C. Carman, "Fluid flow through granular beds." Transactions, Institution of Chemical Engineers, London, 15: 150-166, 1937.

Cheng, Dingsheng, et al. "Geochemical characteristics and origins of biodegraded oils in the Bongor Basin (Chad) and their implications for petroleum exploration." Energy Exploration & Exploitation 40.2 (2022): 682-700.

Cooley, James W., and John W. Tukey. "An algorithm for the machine calculation of complex Fourier series." *Mathematics of computation* 19.90 (1965): 297-301.

Dhansay, Taufeeq, et al. "South Africa's geothermal energy hotspots inferred from subsurface temperature and geology." South African Journal of Science 113.11-12 (2017): 1-7.

Dickson, Mary H., and Mario Fanelli. "Geothermal R&D in developing countries: Africa, Asia and the Americas." *Geothermics* 17.5-6 (1988): 815-877.

Dziewonski, Adam M., and Don L. Anderson. "Preliminary reference Earth model." Physics of the earth and planetary interiors 25.4 (1981): 297-356.

Ehrenberg, S. N., and P. H. Nadeau. "Sandstone vs. carbonate petroleum reservoirs: A global perspective on porosity-depth and porosity-permeability relationships." AAPG bulletin 89.4 (2005): 435-445.

El Dally, Nancy H., et al. "3D basin and petroleum systems modeling in Shushan Basin, Western Desert, Egypt." Modeling Earth Systems and Environment 9.2 (2023): 2221-2238.

Elmasry, Ahmed, et al. "Exploration of Geothermal Resources Utilizing Geophysical and Borehole Data in the Abu Gharadig Basin of Egypt’s Northern Western Desert." Pure and Applied Geophysics (2022): 1-18.

Emerick, Alexandre A., and Albert C. Reynolds. "Ensemble smoother with multiple data assimilation." *Computers & Geosciences* 55 (2013): 3-15.

Evenick, Jonathan C. "Glimpses into Earth's history using a revised global sedimentary basin map." Earth-Science Reviews 215 (2021): 103564.

Evensen, Geir. "Sequential data assimilation with a nonlinear quasi-geostrophic model using Monte Carlo methods to forecast error statistics." *Journal of Geophysical Research: Oceans* 99.C5 (1994): 10143-10162.

Finger, N-P., et al. "A Thermo-Compositional Model of the African Cratonic Lithosphere." *Geochemistry, Geophysics, Geosystems* 23.3 (2022): e2021GC010296.

Hannah Ritchie, Lucas Rodés-Guirao, Edouard Mathieu, Marcel Gerber, Esteban Ortiz-Ospina, Joe Hasell and Max Roser (2023) - "Population Growth". Published online at OurWorldInData.org. Retrieved from: 'https://ourworldindata.org/population-growth' [https://ourworldindata.org/population-growth]

Galeazzi, S., et al. "Regional geology and petroleum systems of the Illizi–Berkine area of the Algerian Saharan Platform: An overview." Marine and Petroleum Geology 27.1 (2010): 143-178.

Galushkin, Yu, S. Eloghbi, and M. Sak. "Burial and thermal history modelling of the Murzuq and Ghadames Basins (Libya) using the GALO computer programme." Journal of Petroleum Geology 37.1 (2014): 71-93.

Gousmania, M., et al. "Prospection géoélectrique pour l’étude de l’aquifer thermal des calcaires récifaux, Hmeima-Boujabeur (centre ouest de la Tunisie)." CR Geosciences 338 (2006): 1219-1227.

Hantschel, Thomas, and Armin I. Kauerauf. Fundamentals of basin and petroleum systems modelling. Springer Science & Business Media, 2009.

Harouna, M., J. D. Pigott, and R. P. Philp. "Burial history and thermal maturity evolution of the Termit Basin, Niger." Journal of Petroleum Geology 40.3 (2017): 277-297.

Hollander den, G.P., “Investigation of different forward gravity models and their application for the Dinantian in the Nederlands. Internship report TNO (2017?)

Homuth, S., A. E. Götz, and Ingo Sass. "Reservoir characterization of the Upper Jurassic geothermal target formations (Molasse Basin, Germany): role of thermofacies as exploration tool." Geothermal Energy Science 3.1 (2015): 41-49.

Huang, Zhilong, et al. "Petroleum systems of the Taoudeni basin, West Africa." Petroleum Science 5.1 (2008): 24-30.

IEA (2019), Africa Energy Outlook 2019, IEA, Paris https://www.iea.org/reports/africa-energy-outlook-2019, License: CC BY 4.0

Iglesias, Marco A., Kody JH Law, and Andrew M. Stuart. "Ensemble Kalman methods for inverse problems." Inverse Problems 29.4 (2013): 045001.

IRENA and AfDB (2022), Renewable Energy Market Analysis: Africa and Its Regions, International Renewable Energy Agency and African Development Bank, Abu Dhabi and Abidjan.

Jones, D.J.R. (2022). Trans-African Regional Geo-data for the Energy Transition (TARGET) model. NERC EDS National Geoscience Data Centre. (Dataset). https://doi.org/10.5285/e9ca452b-5cca-4953-b5a4-397c4d622ea5

Klett, Timothy R. Total Petroleum Systems of the Trias/Ghadames Province, Algeria, Tunisia, and Libya--the Tanezzuft-Oued Mya, Tanezzuft-Melrhir, and Tanezzuft-Ghadames. US Department of the Interior, US Geological Survey, 2000.

Kombe, Emmanuel Yeri, and Joseph Muguthu. "Geothermal energy development in East Africa: barriers and strategies." J. Energy Res. Rev 2.1 (2019): 1-6.

Kozeny, Josef. "Ueber kapillare leitung des wassers im boden." Sitzungsberichte der Akademie der Wissenschaften in Wien 136 (1927): 271.

Lashin, Aref. "Review of the geothermal resources of Egypt: 2015-2020." Proceedings World Geothermal Congress. 2020.

Laske, Gabi, et al. "Update on CRUST1. 0—A 1-degree global model of Earth's crust." Geophysical research abstracts. Vol. 15. No. 15. Vienna, Austria: EGU General Assembly, 2013.

Lebbihiat, Nacer, et al. "Geothermal energy use in Algeria: A review on the current status compared to the worldwide, utilization opportunities and countermeasures." Journal of Cleaner Production 302 (2021): 126950.

Lejeune, Jean-Mary, and Jacques Varet. "Low enthalpy geothermal development in France: the situation in early 1981." *Trans.-Geotherm. Resour. Counc.;(United States)* 5.CONF-811015- (1981).

Limberger, Jon, et al. "Geothermal energy in deep aquifers: A global assessment of the resource base for direct heat utilization." Renewable and Sustainable Energy Reviews 82 (2018): 961-975.

Limberger, J., et al. "A public domain model for 1D temperature and rheology construction in basement-sedimentary geothermal exploration: an application to the Spanish Central System and adjacent basins." *Acta Geodaetica et Geophysica* 52 (2017): 269-282.

Limberger, J., et al. "B1T: A public domain model for 1D temperature and rheology construction in basement-sedimentary geothermal exploration."

Majorowicz, J. A., et al. "Topography and the subsurface temperature regime in the Western Canadian Sedimentary Basin: implications for low-enthalpy geothermal energy recovery." *Geothermics* 14.2-3 (1985): 175-187.

Makeen, Yousif M., et al. "Thermal maturity history and petroleum generation modelling for the Lower Cretaceous Abu Gabra Formation in the Fula Sub-basin, Muglad Basin, Sudan." Marine and Petroleum Geology 75 (2016): 310-324.

Makhous, M., and Yu I. Galushkin. "Burial history and thermal evolution of the southern and western Saharan basins: Synthesis and comparison with the eastern and northern Saharan basins." AAPG bulletin 87.11 (2003): 1799-1822.

Makled, Walid A., et al. "Petroleum play of the Lower Cretaceous Alam El Bueib Formation in the El Noor-1X well in the north Western Desert (Egypt): A sequence stratigraphic framework." Marine and Petroleum Geology 116 (2020): 104287.

Minissale, A. A., and V. Duchi. "Geothermometry on fluids circulating in a carbonate reservoir in north-central Italy." Journal of volcanology and Geothermal Research 35.3 (1988): 237-252.

Mohammadi, Z., R. Bagheri, and R. Jahanshahi. "Hydrogeochemistry and geothermometry of Changal thermal springs, Zagros region, Iran." Geothermics 39.3 (2010): 242-249.

Montanari, D., et al. "Geothermal resources within carbonate reservoirs in western Sicily (Italy): A review." Earth-Science Reviews 169 (2017): 180-201.

Mooney, Walter D., et al. "Earth crustal model 1 (ECM1): A 1 x 1 global seismic and density model." Earth-Science Reviews (2023): 104493.

Morakinyo, A. M., A. Y. Mohamed, and S. A. Bowden. "The release of petroleum from Central Africa rift basins over geological time as deduced from petroleum systems modelling." Journal of African Earth Sciences 183 (2021): 104319.

NOAA National Geophysical Data Center. 2009: ETOPO1 1 Arc-Minute Global Relief Model. NOAA National Centers for Environmental Information. Accessed [21-11-2022].

NOAA Technical Memorandum: Amante, C. and B.W. Eakins, 2009. ETOPO1 1 Arc-Minute Global Relief Model: Procedures, Data Sources and Analysis. NOAA Technical Memorandum NESDIS NGDC-24. National Geophysical Data Center, NOAA. doi:10.7289/V5C8276M [21-11-2022].

Nwankwo, Cyril, Anthony Ekine, and Leonard Nwosu. "Burial Analysis and evolution history of Chad basin Nigeria." Nigerian Journal of Physics 25.1 (2014).

Oldenburg, Douglas W., and Yaoguo Li. "Inversion for applied geophysics: A tutorial." Near-surface geophysics (2005): 89-150.

Ojo, O. J., I. Akpabio, and J. Frielingsdorf. "Burial and thermal history modeling and petroleum potential evaluation of the northwestern Niger Delta, Nigeria." Comunicaçõe Geológicas 99.2 (2012).

Pasquale, V., M. Verdoya, and P. Chiozzi. "Heat flow and geothermal resources in northern Italy." Renewable and Sustainable Energy Reviews 36 (2014): 277-285.

Quiroga, Elizabeth, et al. "A 3D geological model of the horn of Africa: New insights for hydrogeological simulations of deep groundwater systems." Journal of Hydrology: Regional Studies 42 (2022): 101166.

Ramadan, Abu El-Ella. "Maturation history of Neogene-Quaternary sediments, Nile delta basin, Egypt." AAPG bulletin 74.1 (1990): 77-84.

Reguzzoni, Mirko, and Daniele Sampietro. "GEMMA: An Earth crustal model based on GOCE satellite data." International Journal of Applied Earth Observation and Geoinformation 35 (2015): 31-43.

Reichle, Rolf H. "Data assimilation methods in the Earth sciences." Advances in water resources 31.11 (2008): 1411-1418.

Rybach, L., and F. C. Jaffe. "Low enthalpy geothermal energy exploration and development in Switzerland." *Trans.-Geotherm. Resour. Counc.;(United States)* 5.CONF-811015- (1981).

Salama, Abdelrahman M., et al. "Source rock evaluation and burial history modeling of Cretaceous rocks at the Khalda Concession of Abu Gharadig Basin, Western Desert, Egypt." Journal of African Earth Sciences 184 (2021): 104372.

Sarhan, Mohammad Abdelfattah. "Geophysical appraisal and oil potential for Rudeis Formation at West Hurghada area, southern Gulf of Suez: detection of stratigraphic trap." Arabian Journal of Geosciences 13.6 (2020): 263.

Simsek, Sakir. "Hydrogeological and isotopic survey of geothermal fields in the Buyuk Menderes graben, Turkey." Geothermics 32.4-6 (2003): 669-678.

Stober, Ingrid, et al. "History of geothermal energy use." Geothermal Energy: From Theoretical Models to Exploration and Development (2013): 15-24.

Straume, Eivind Olavson, et al. "GlobSed: Updated total sediment thickness in the world's oceans." Geochemistry, Geophysics, Geosystems 20.4 (2019): 1756-1772.

Underdown, R., J. Redfern, and F. Lisker. "Constraining the burial history of the Ghadames Basin, North Africa: an integrated analysis using sonic velocities, vitrinite reflectance data and apatite fission track ages." Basin Research 19.4 (2007): 557-578.

United Nations, Department of Economic and Social Affairs, Population Division (2022). World Population Prospects 2022: Data Sources. (UN DESA/POP/2022/DC/NO. 9).

United Nations, Paris Climate Agreement, Conference date: November 2015, Publication date: 29 November 2018. https://unfccc.int/documents/184656

Watts, Anthony Brian. Isostasy and Flexure of the Lithosphere. Cambridge University Press, 2001.

Wright, Lachlan JM, James D. Muirhead, and Christopher A. Scholz. "Spatiotemporal variations in upper crustal extension across the different basement terranes of the Lake Tanganyika Rift, East Africa." Tectonics 39.3 (2020): e2019TC006019.

Zanguina, M., A. Bruneton, and R. Gonnard. "An introduction to the petroleum potential of Niger." Journal of Petroleum Geology 21.1 (1998): 83-103.

8.2. Websites

https://www.nlog.nl/tools, Accessed on January 2024, Geological survey Netherlands (GDN-TNO)

https://www.thermogis.nl/doubletcalc1d, Accessed on January 2024, Geological survey Netherlands (GDN-TNO)

https://sourceforge.net/projects/plotdigitizer/, Accessed on August 2023 → jhuwaldt, Slashdot Media (2020)

Surfer®, 2023, Golden Software, LLC, PO Box 281 Golden, CO 80402-0281 USA: www.goldensoftware.com

QGIS.org, 2023. QGIS Geographic Information System. QGIS Association: http://www.qgis.org

https://www.dinoloket.nl/, Accessed on September 2023, Geologische Dienst Nederland (2023)

https://www.jetbrains.com/pycharm, Accessed on August 2023, JetBrains s.r.o. (2023)

https://neo.gsfc.nasa.gov/, Land & sea surface temperature measurements 2022. Accessed on November 2023. Land surface images by the NASA Earth Observations (NEO) team using data courtesy of the Land Processes Distributed Active Archive Center (LPDAAC) and the MODIS Land Science Team. Sea surface imagery processed by the NASA Earth Observations (NEO) team in collaboration with Gene Feldman and Norman Kuring, NASA OceanColor Group.

9. Appendix

Continental Africa (Low res, sub-area)

- Result observation VS model & Residual

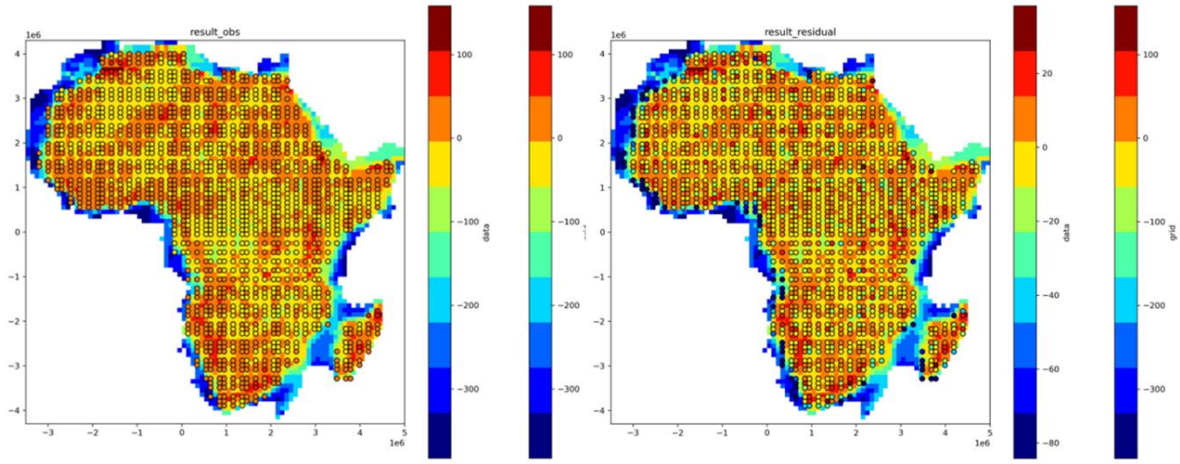

- Obs-Mod plot

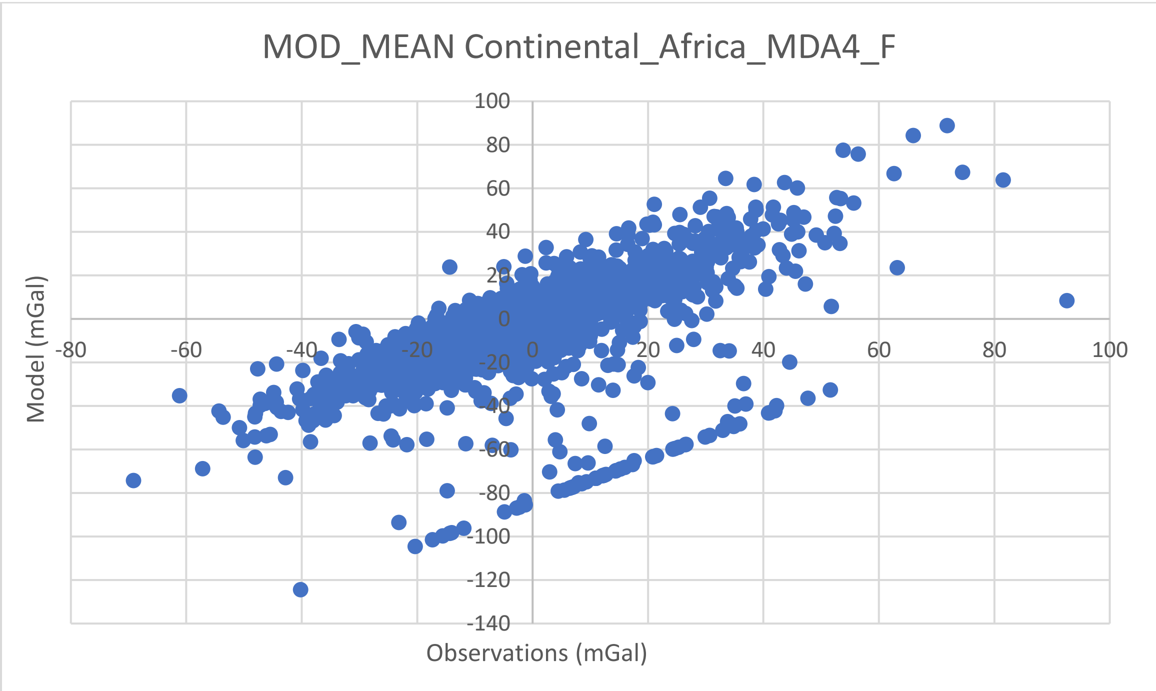

- Result sediment thickness prior & sediment thickness model

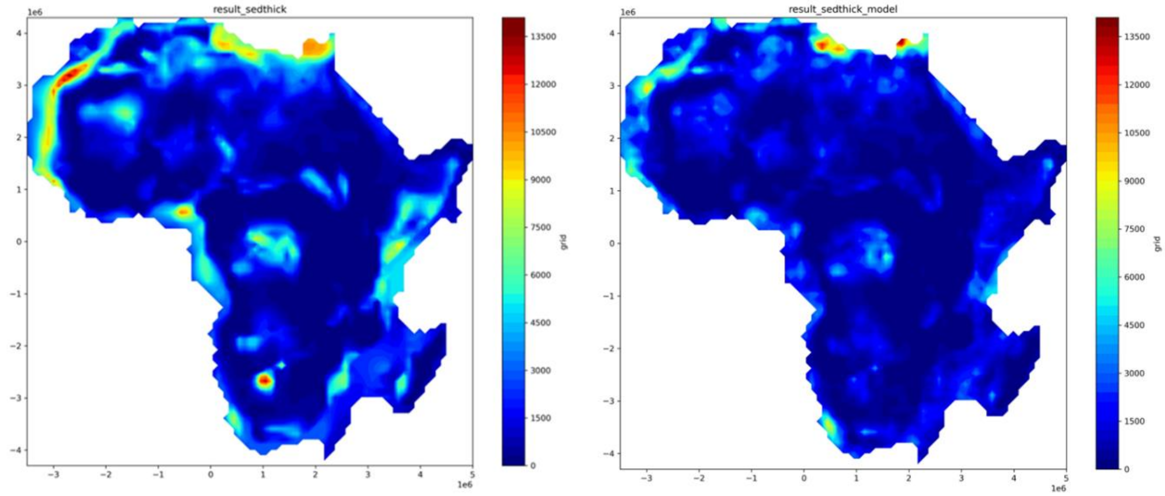

- Crustal density plot

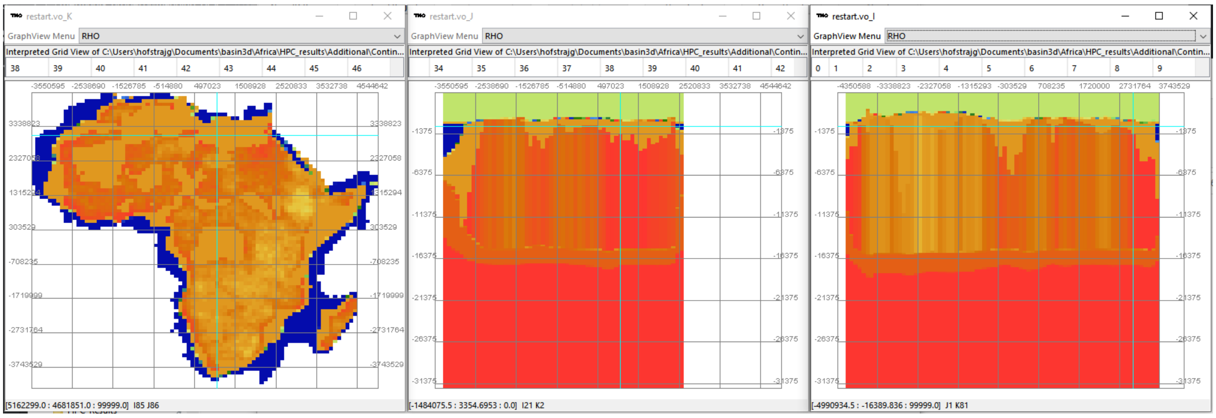

Benue

- Result observation VS model & Residual

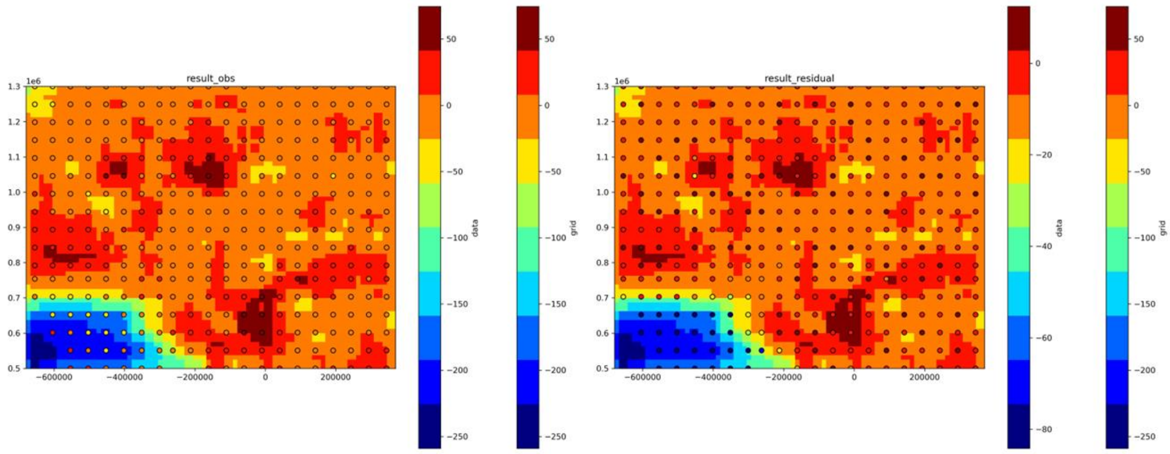

- Obs-Mod plot

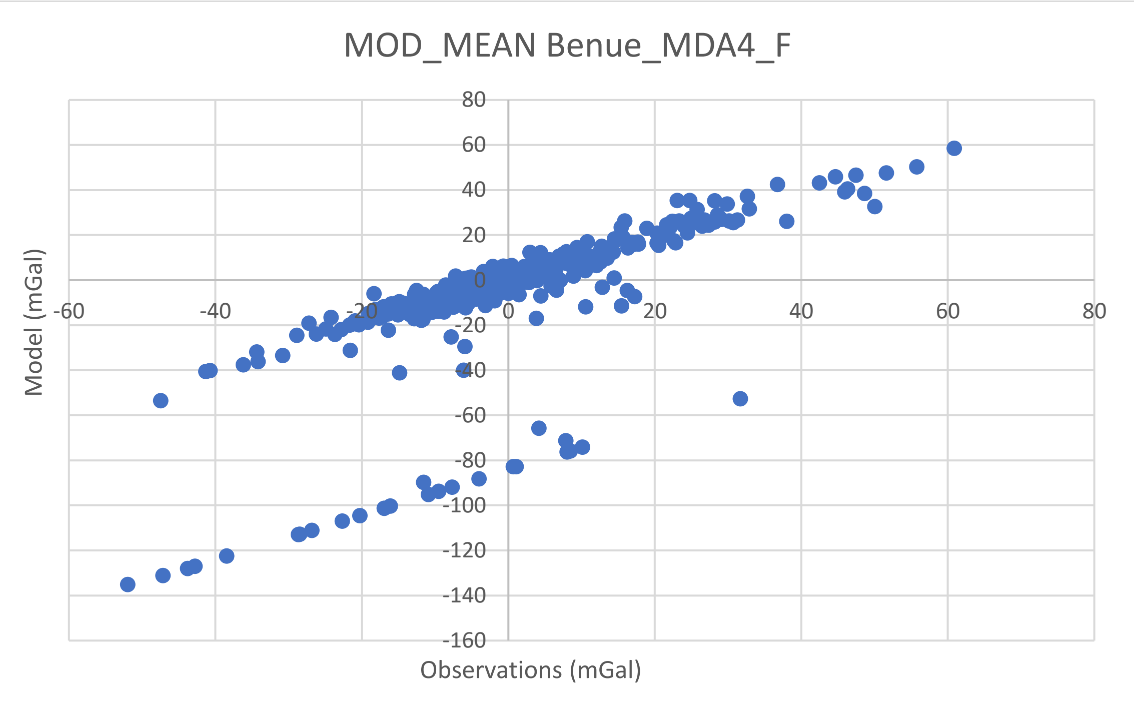

- Result sediment thickness prior & sediment thickness model

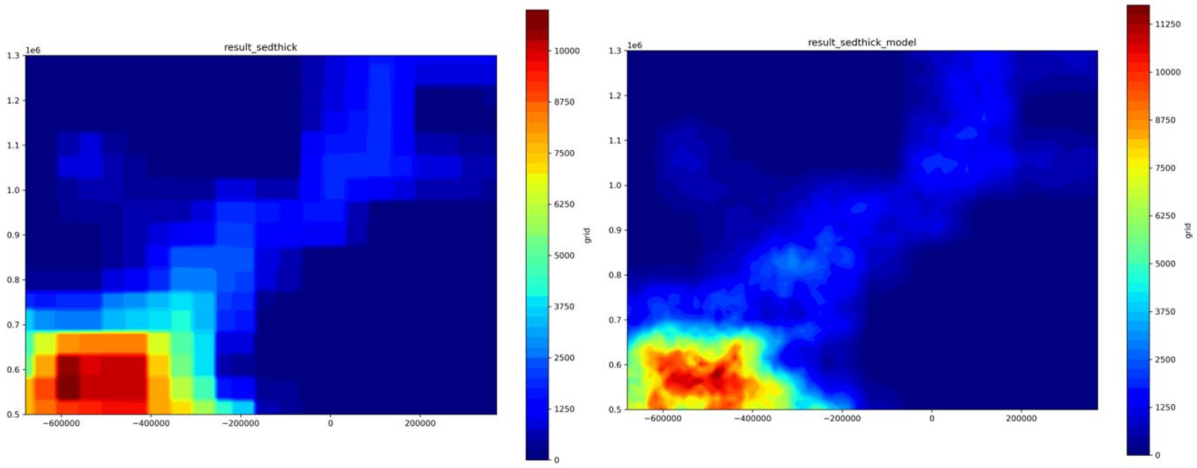

- Crustal density plot

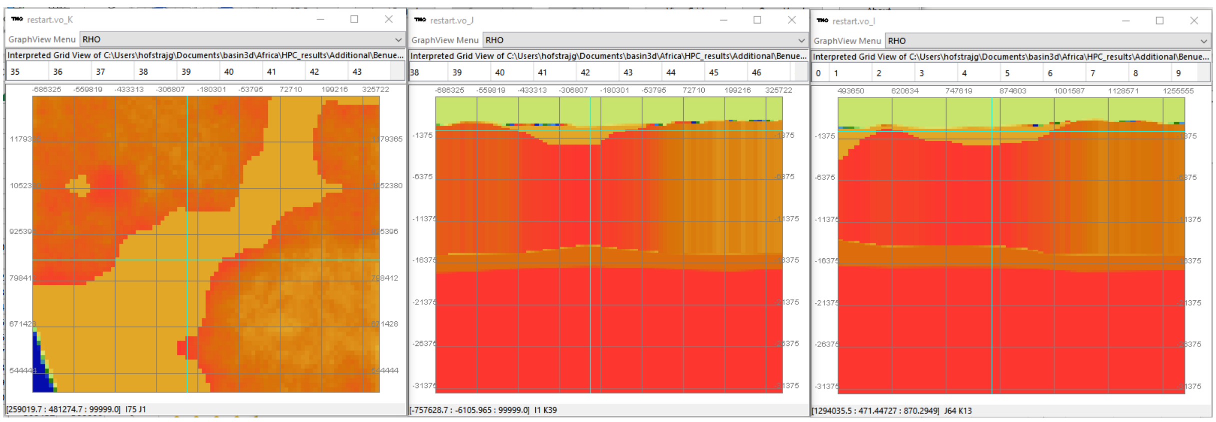

Doba & Doseo

- Result observation VS model & Residual

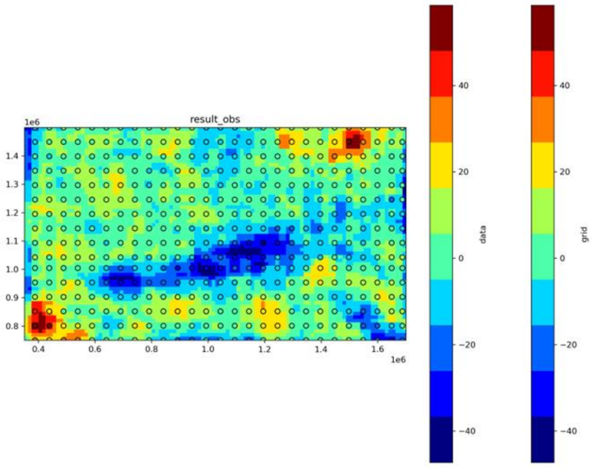

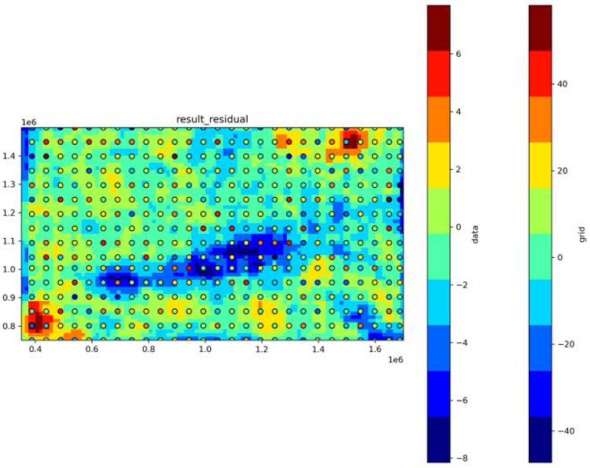

- Obs-Mod plot

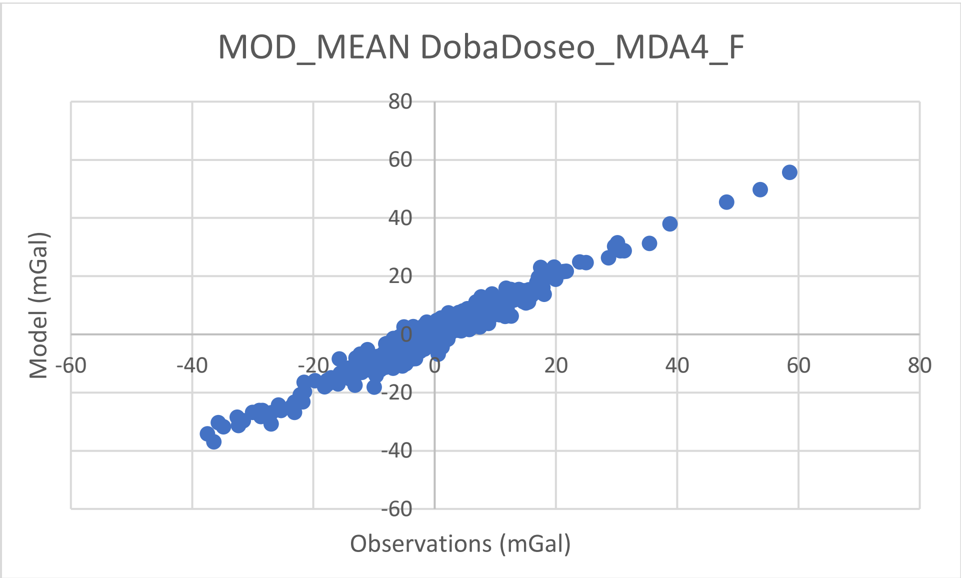

- Result sediment thickness prior & sediment thickness model

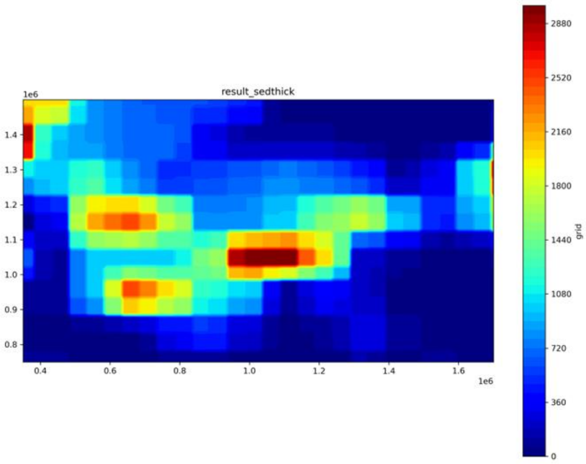

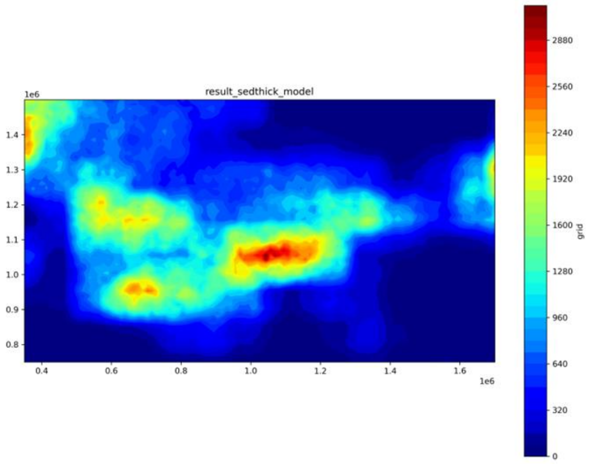

- Crustal density plot

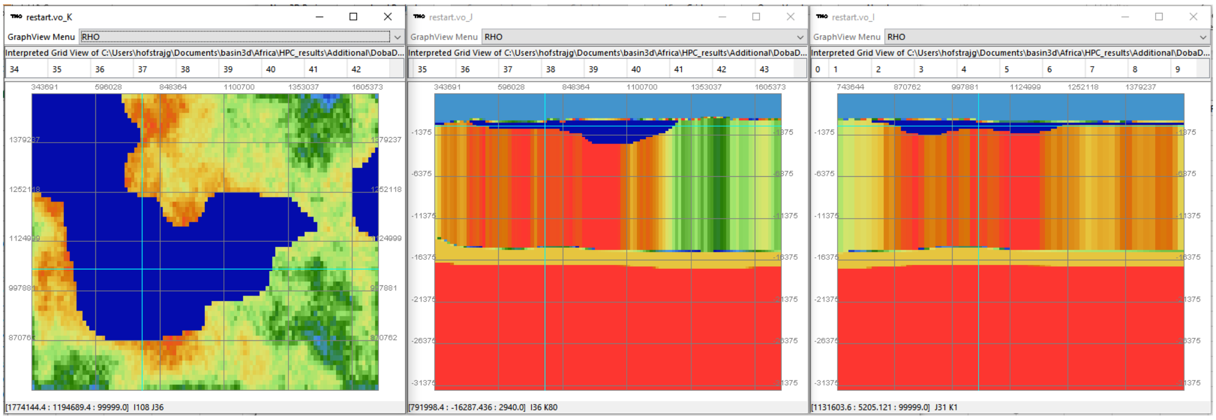

Horn of Africa

- Result observation VS model & Residual

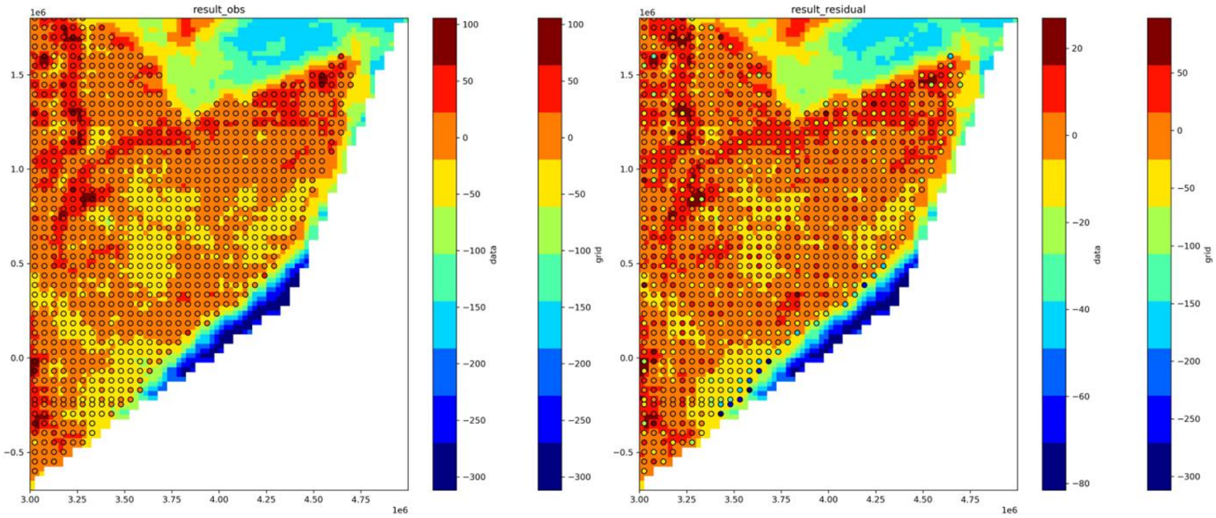

- Obs-Mod plot

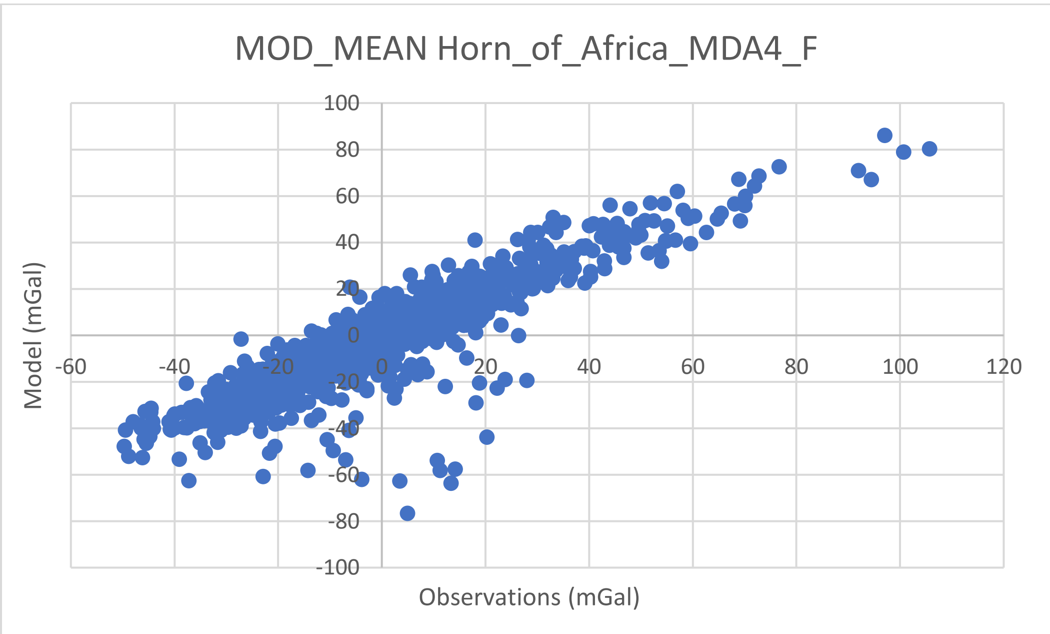

- Result sediment thickness prior & sediment thickness model

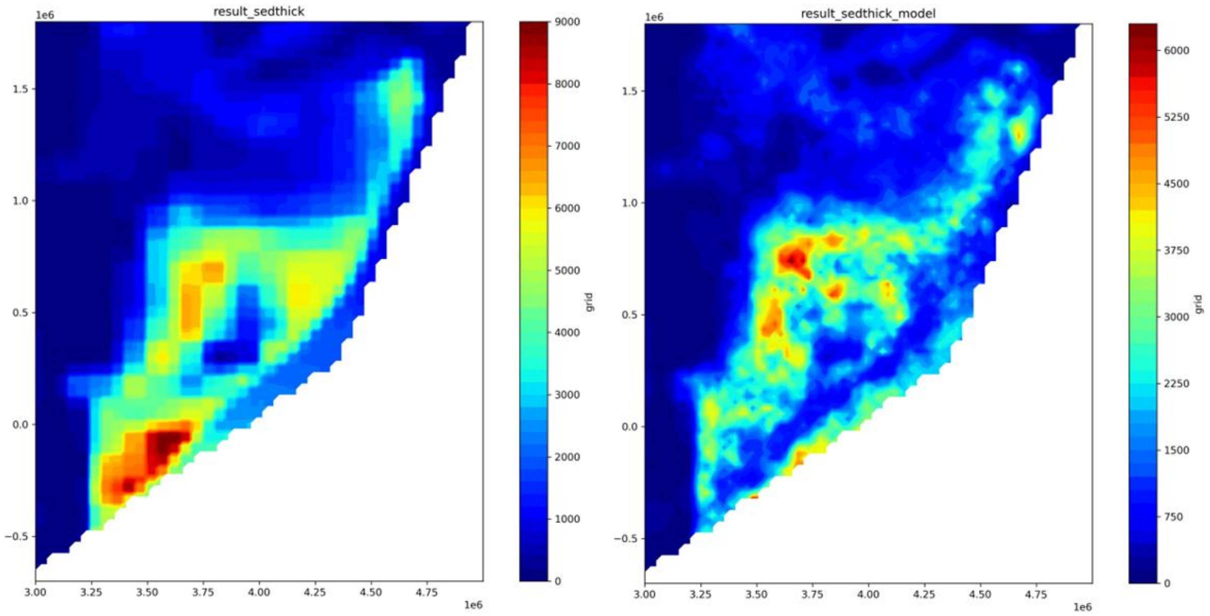

- Crustal density plot

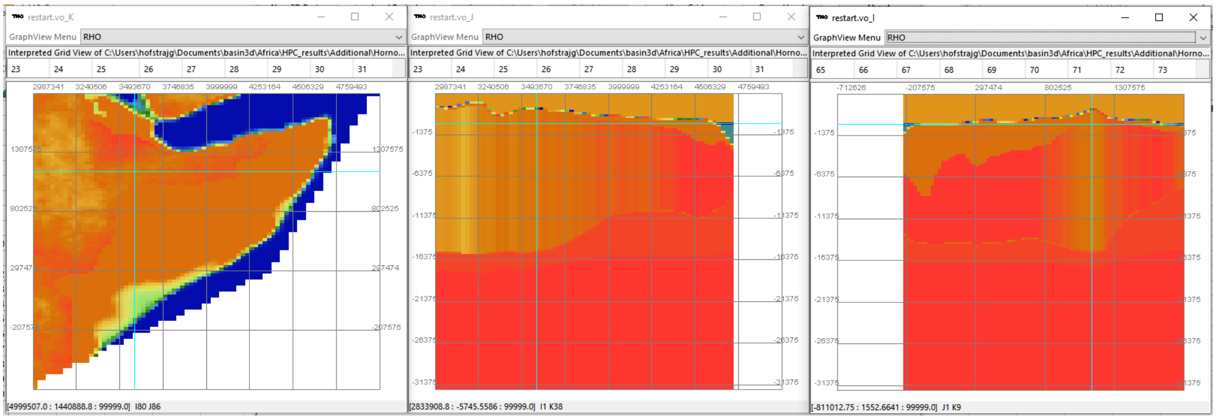

Illumeden

- Result observation VS model & Residual

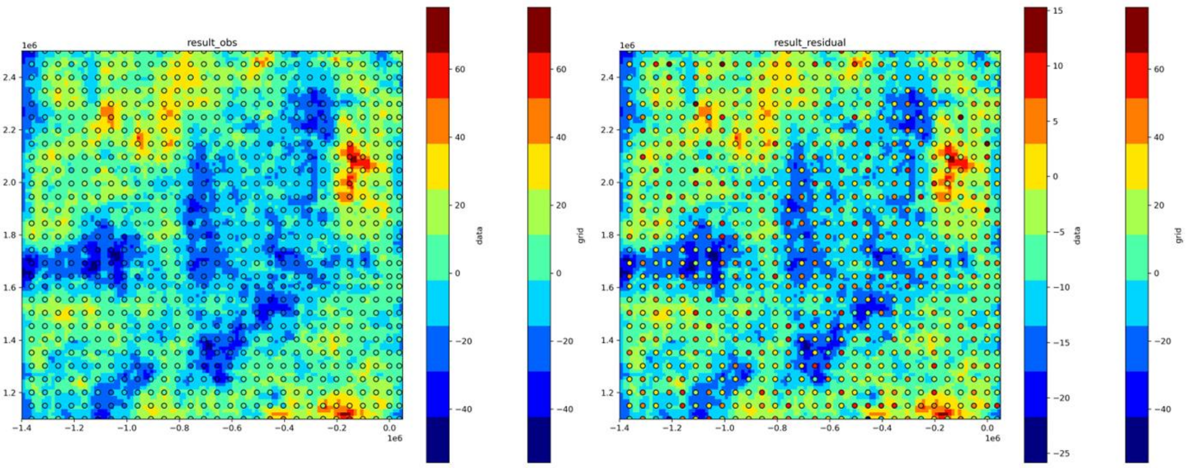

- Obs-Mod plot

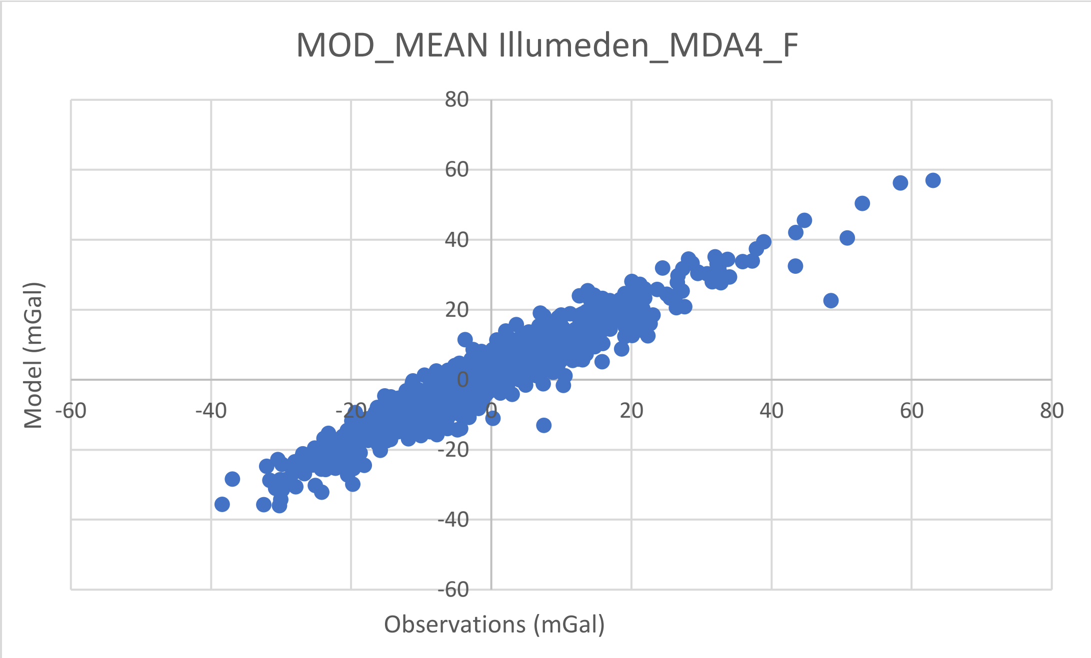

- Result sediment thickness prior & sediment thickness model

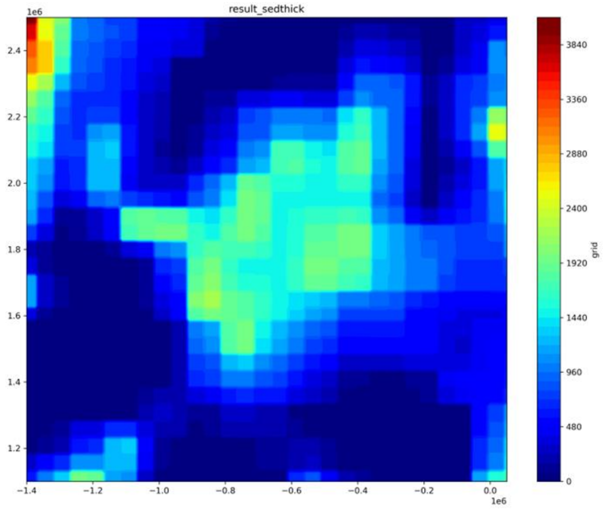

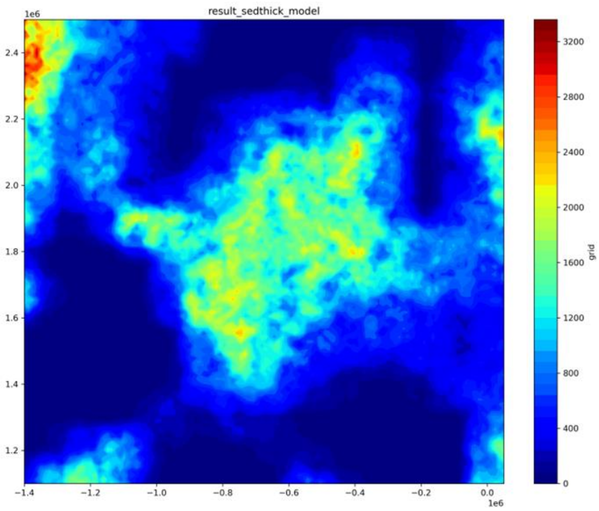

- Crustal density plot

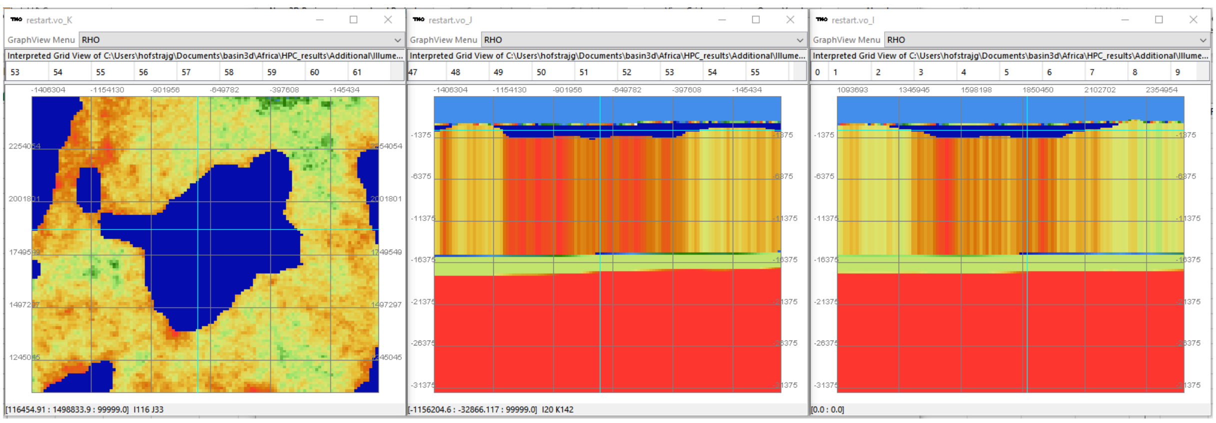

Kalahari

- Result observation VS model & Residual

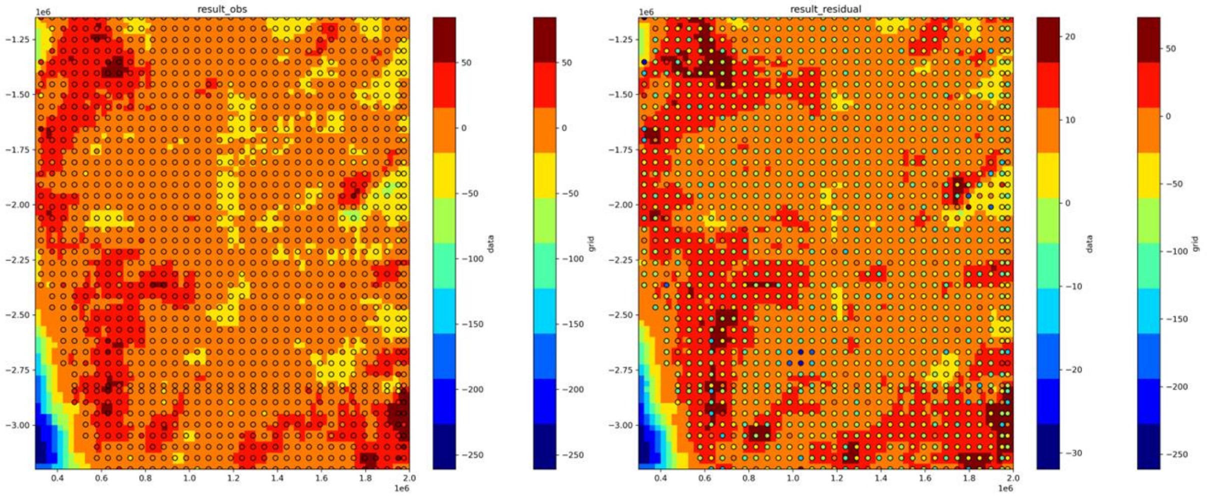

- Obs-Mod plot

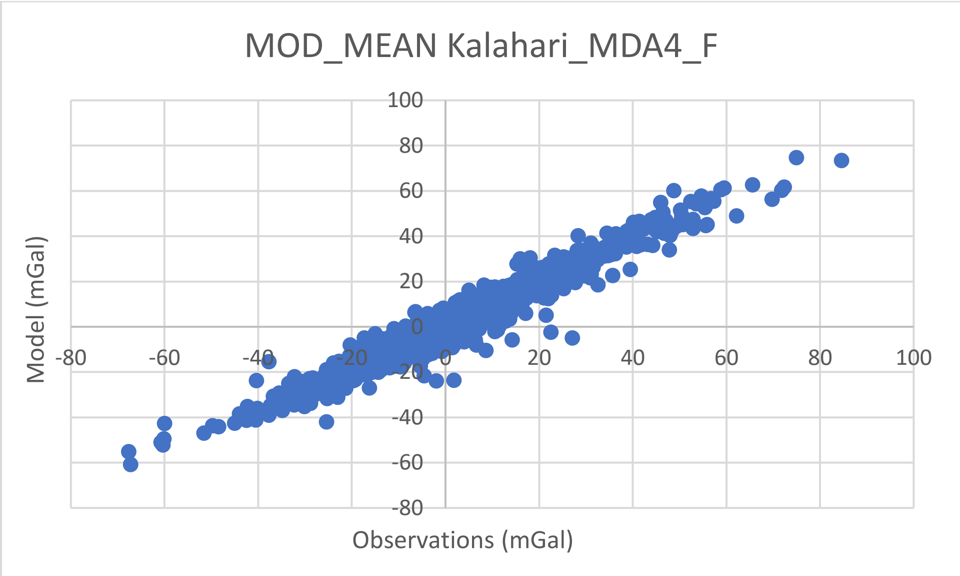

- Result sediment thickness prior & sediment thickness model

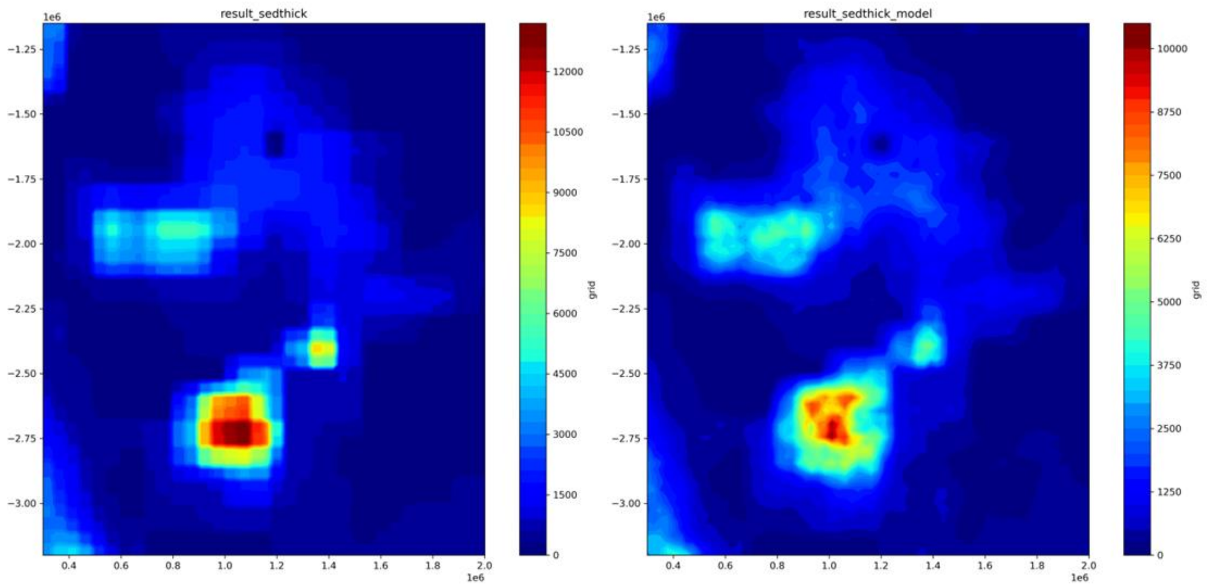

- Crustal density plot

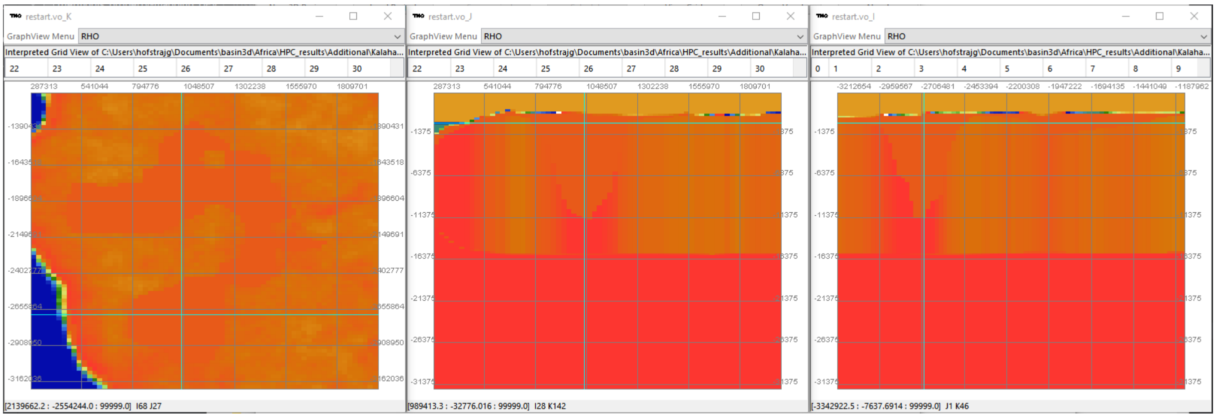

Karoo

- Result observation VS model & Residual

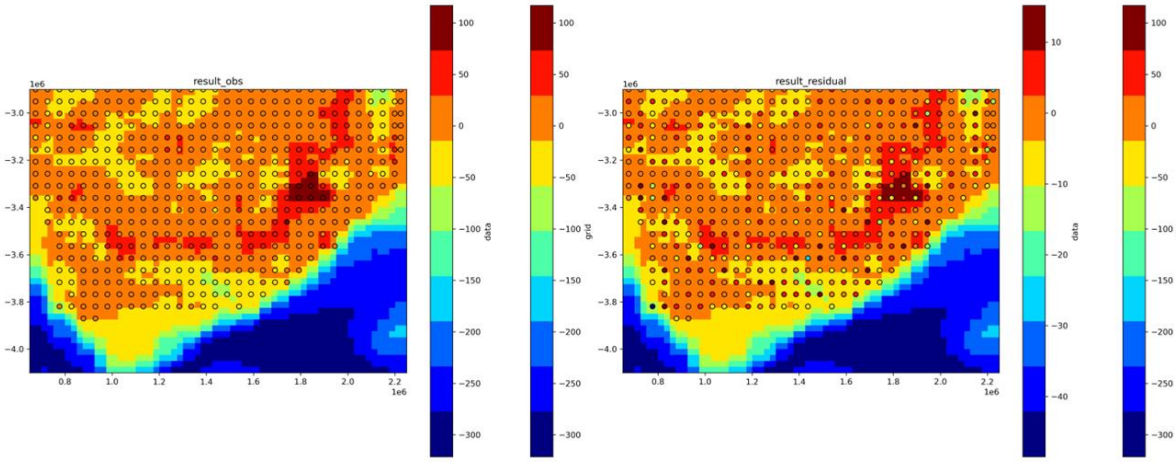

- Obs-Mod plot

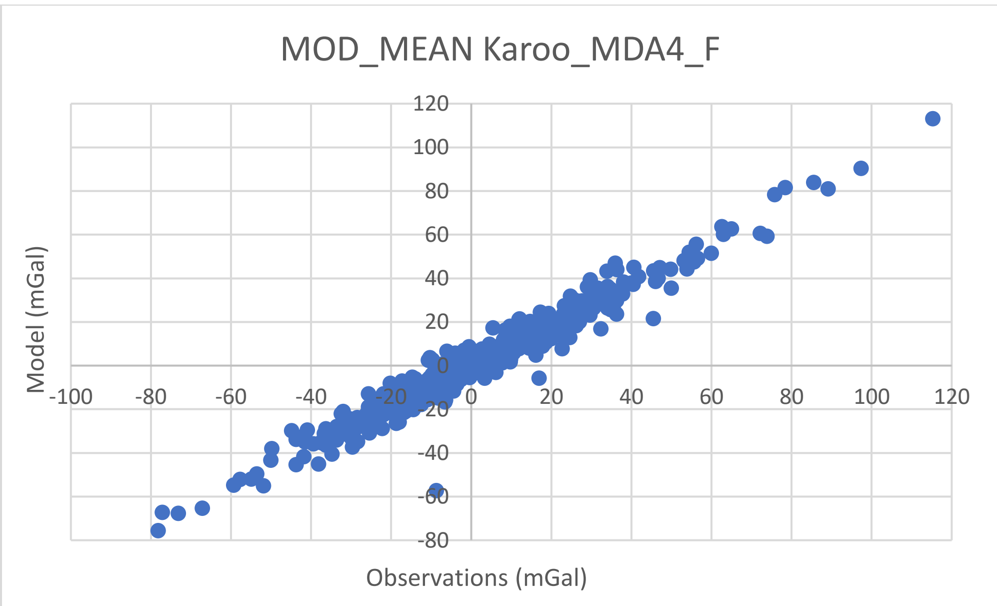

- Result sediment thickness prior & sediment thickness model

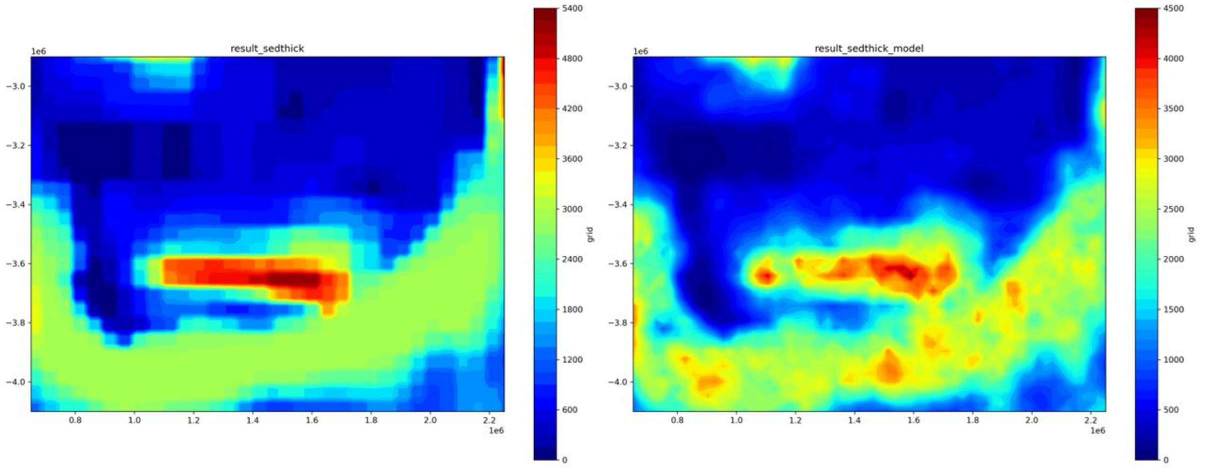

- Crustal density plot

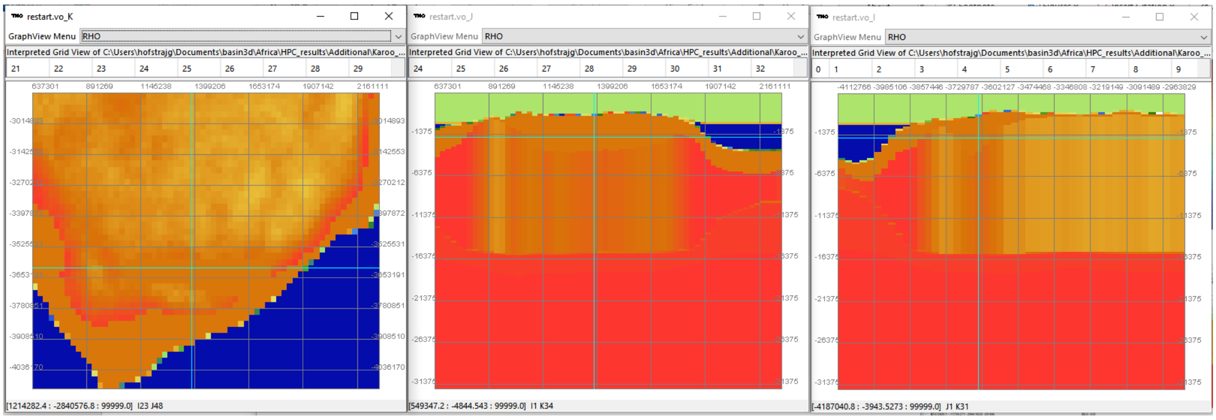

Madagascar

- Result observation VS model & Residual

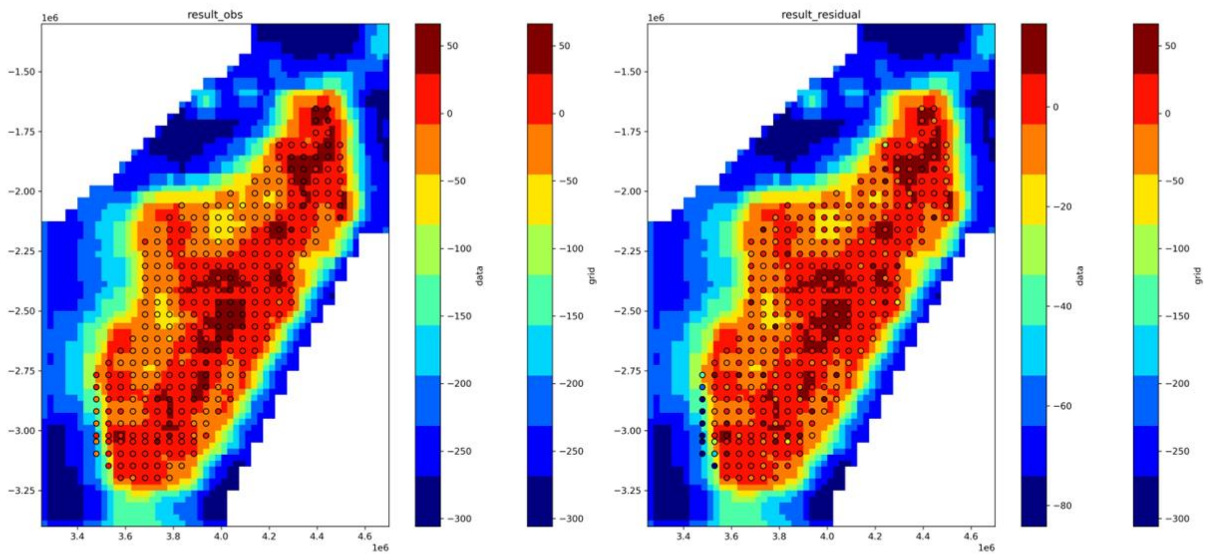

- Obs-Mod plot

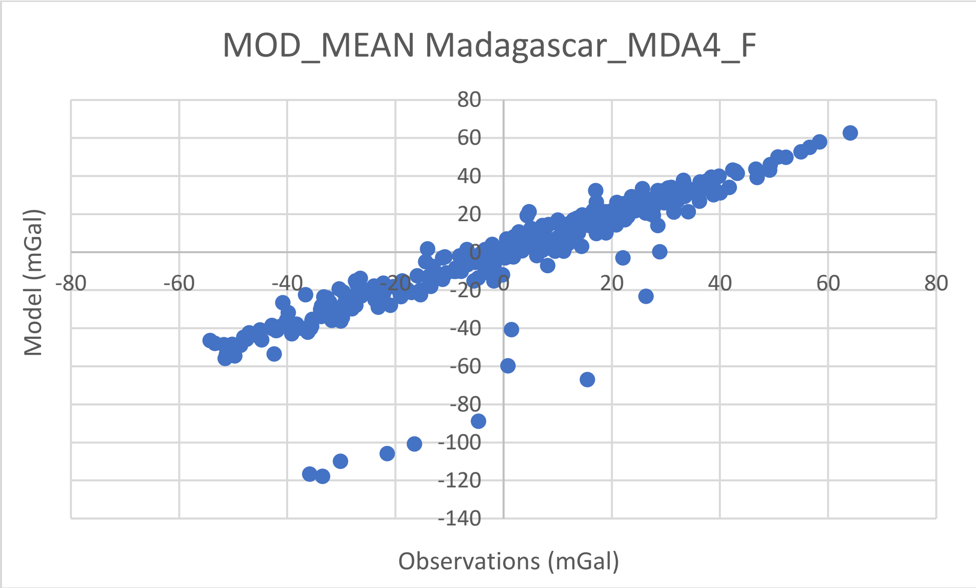

- Result sediment thickness prior & sediment thickness model

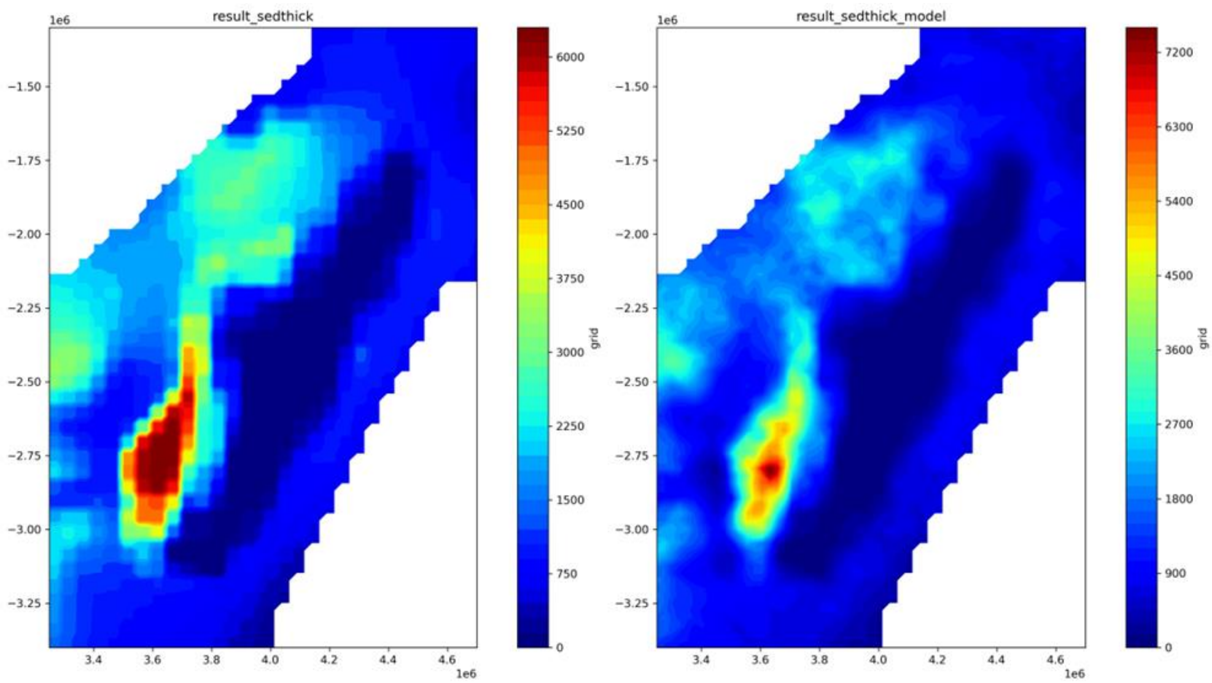

- Crustal density plot

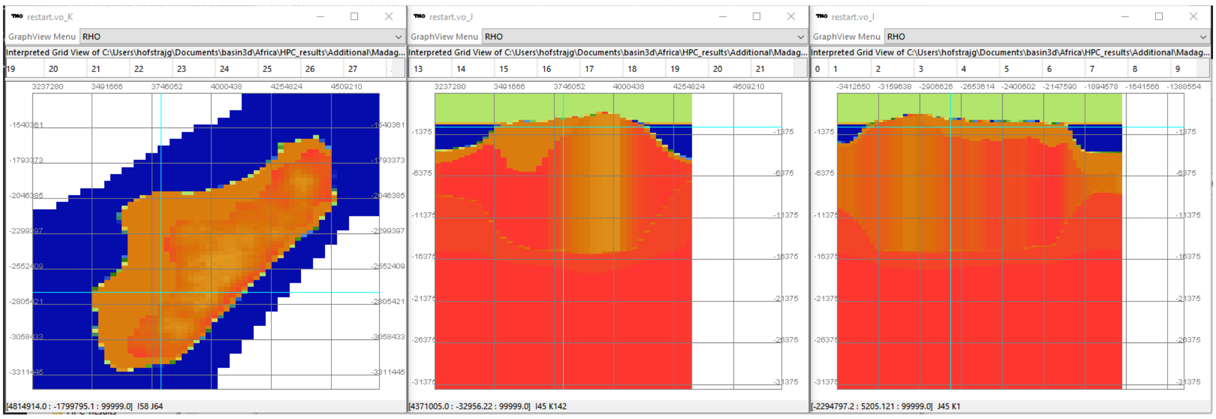

Mozambique

- Result observation VS model & Residual

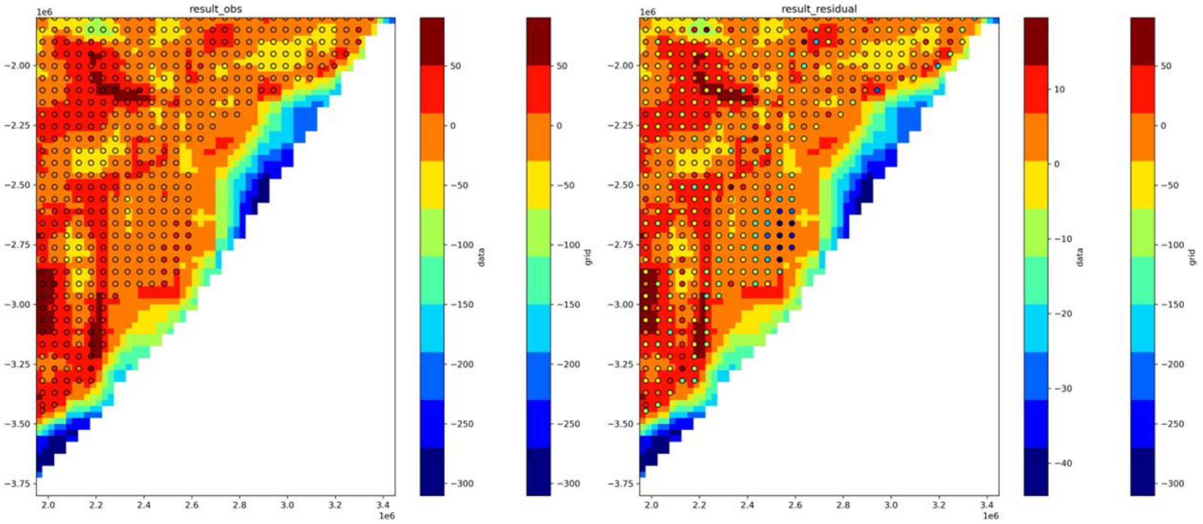

- Obs-Mod plot

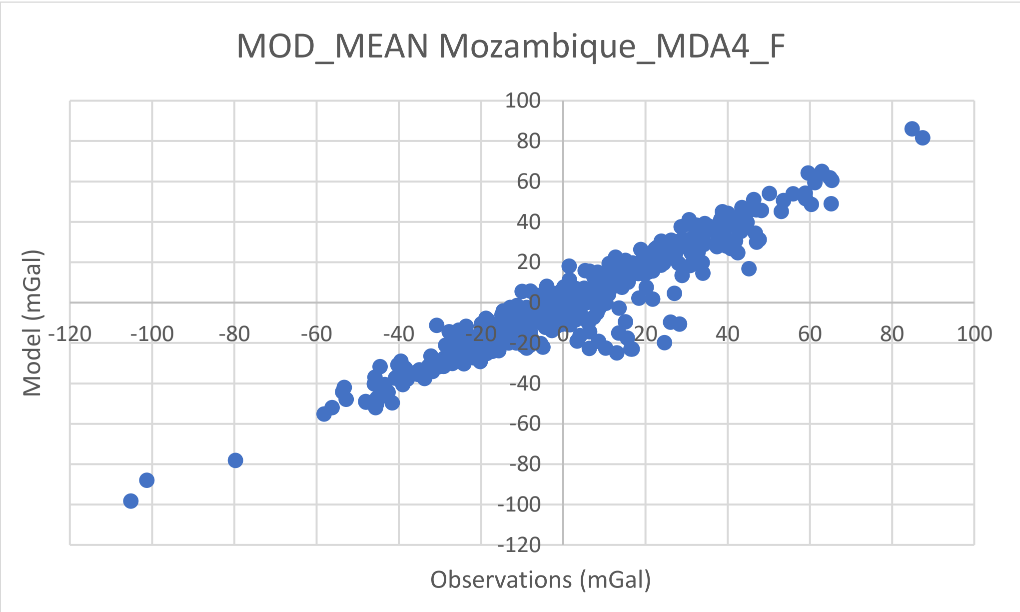

- Result sediment thickness prior & sediment thickness model

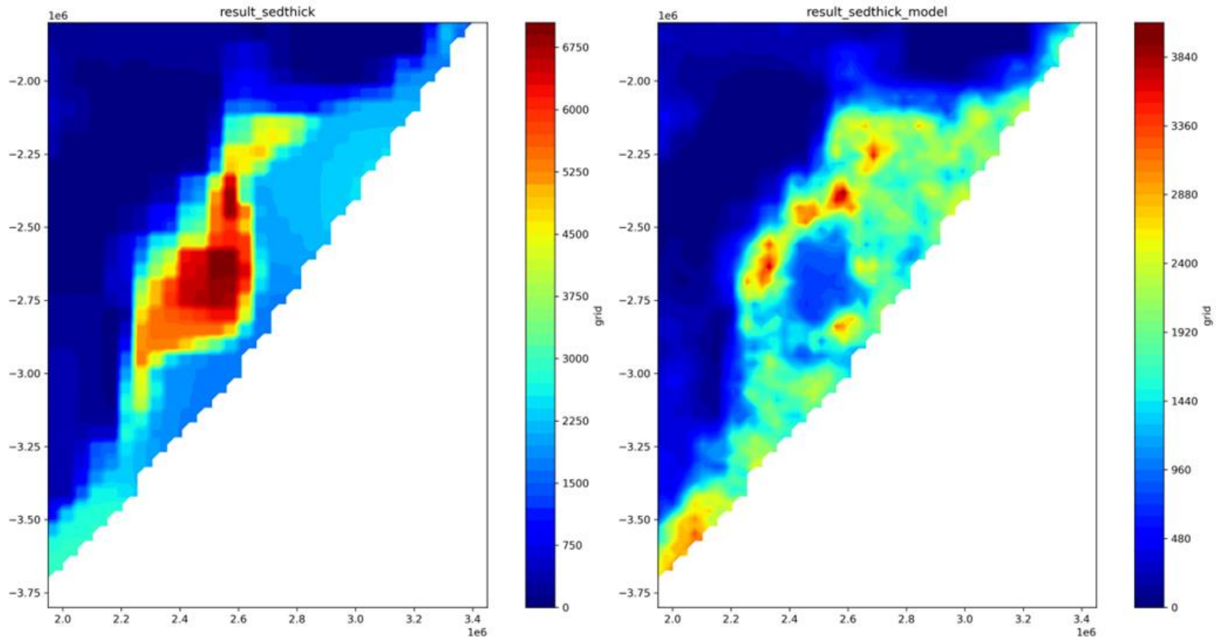

- Crustal density plot

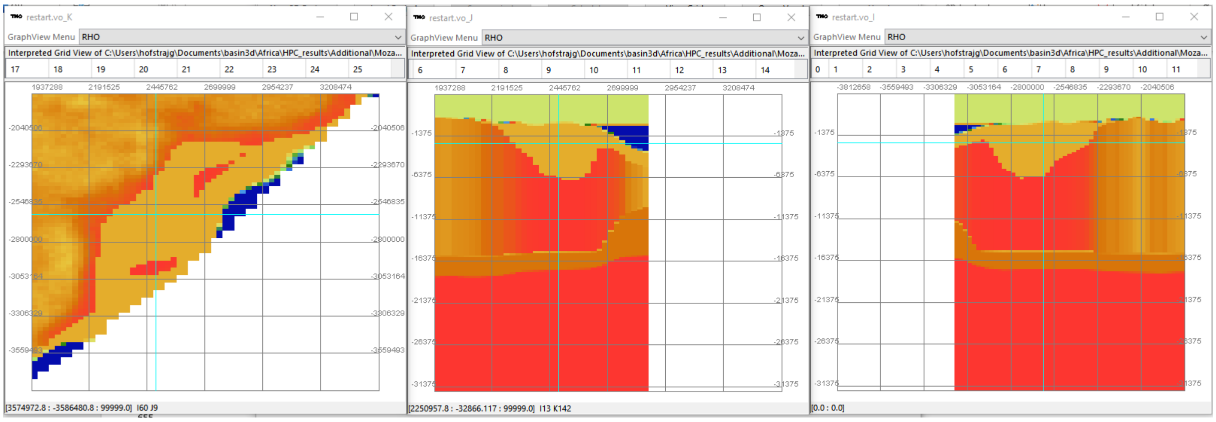

Muglad & Melut

- Result observation VS model & Residual

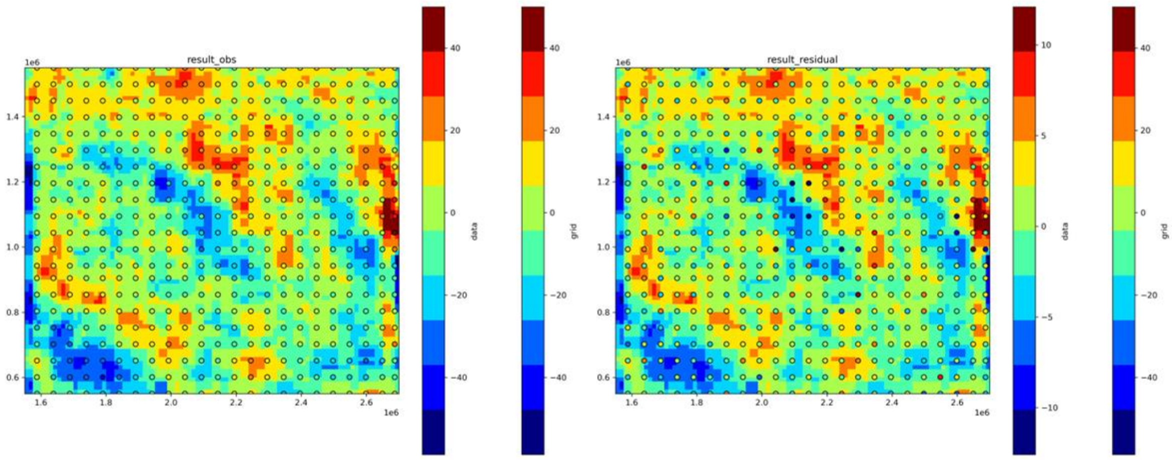

- Obs-Mod plot

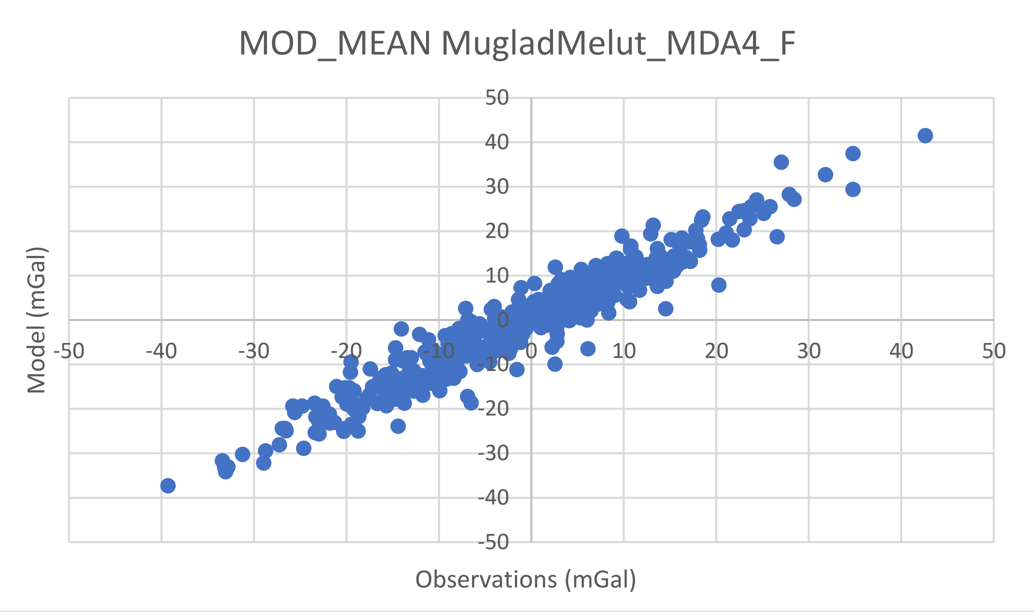

- Result sediment thickness prior & sediment thickness model

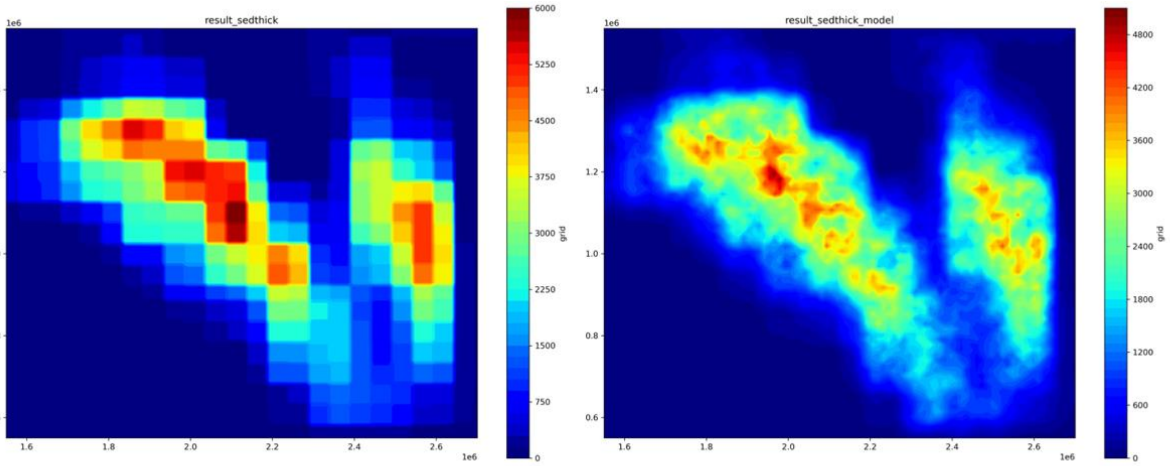

- Crustal density plot

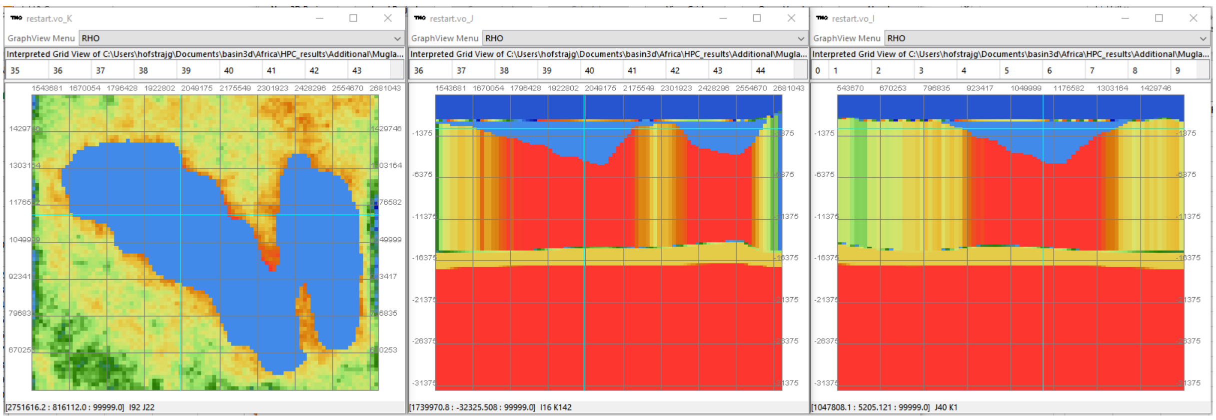

Melut (Higher res)

- Result observation VS model & Residual

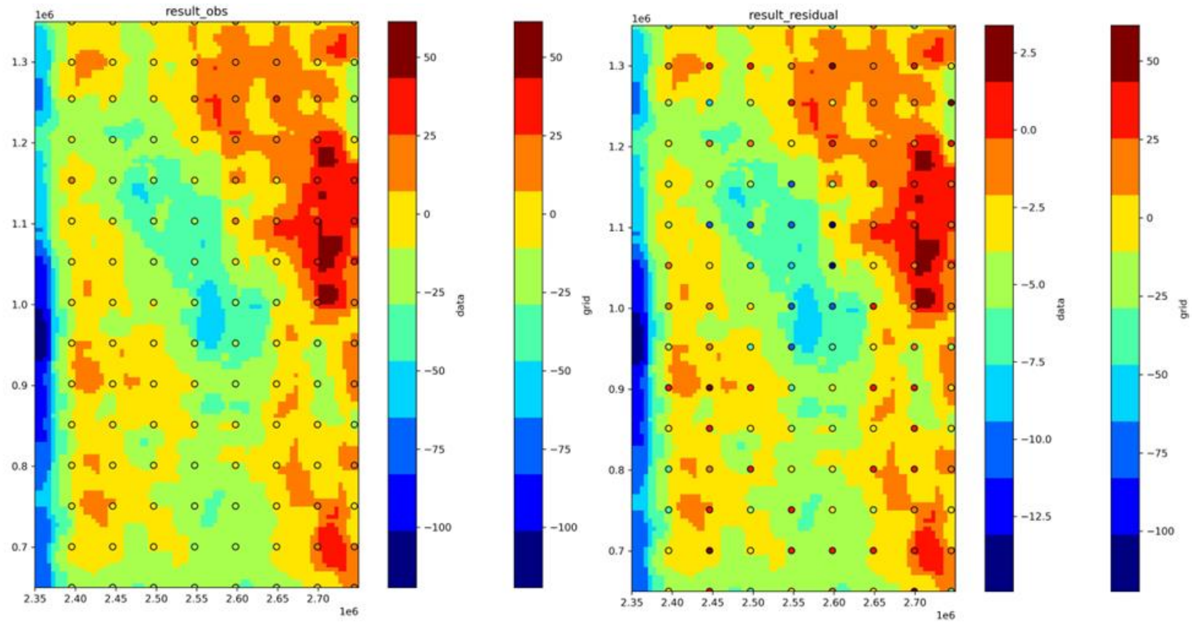

- Obs-Mod plot

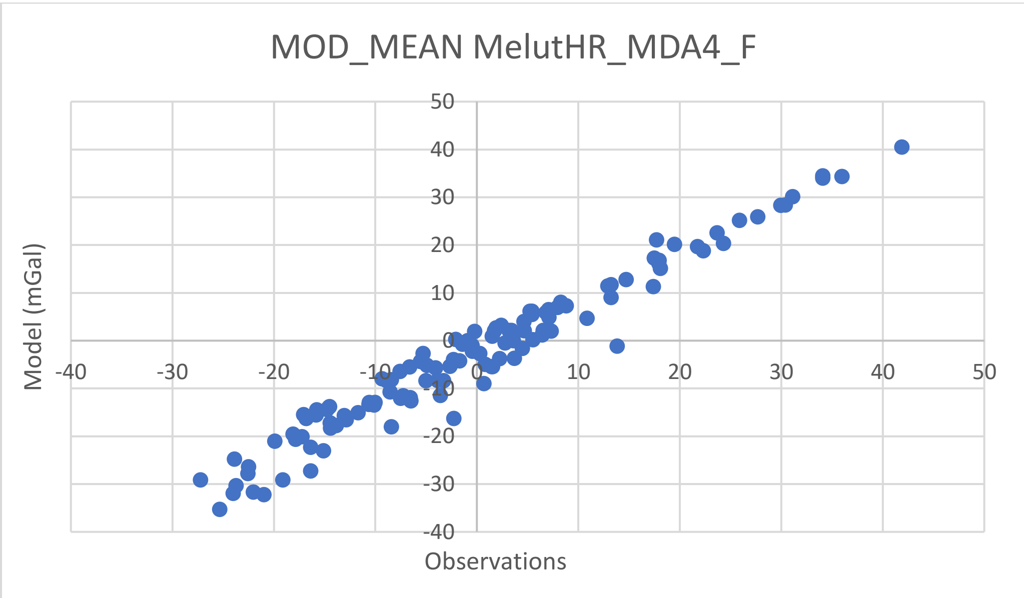

- Result sediment thickness prior & sediment thickness model

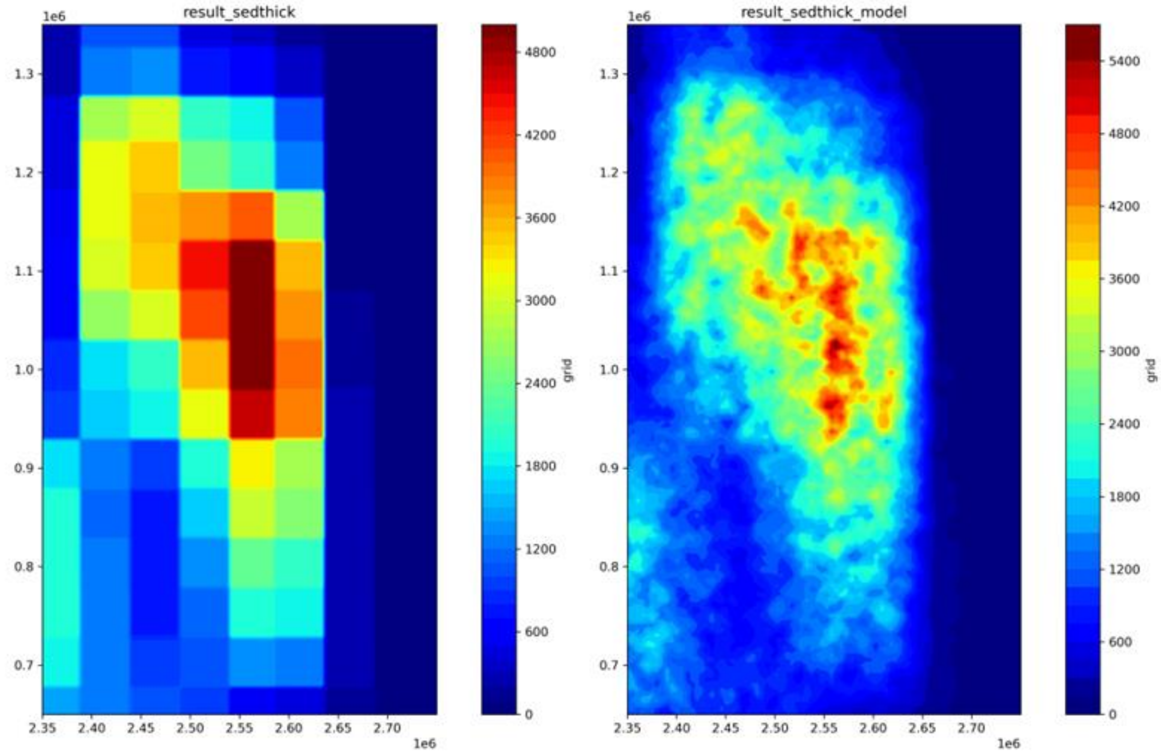

- Crustal density plot

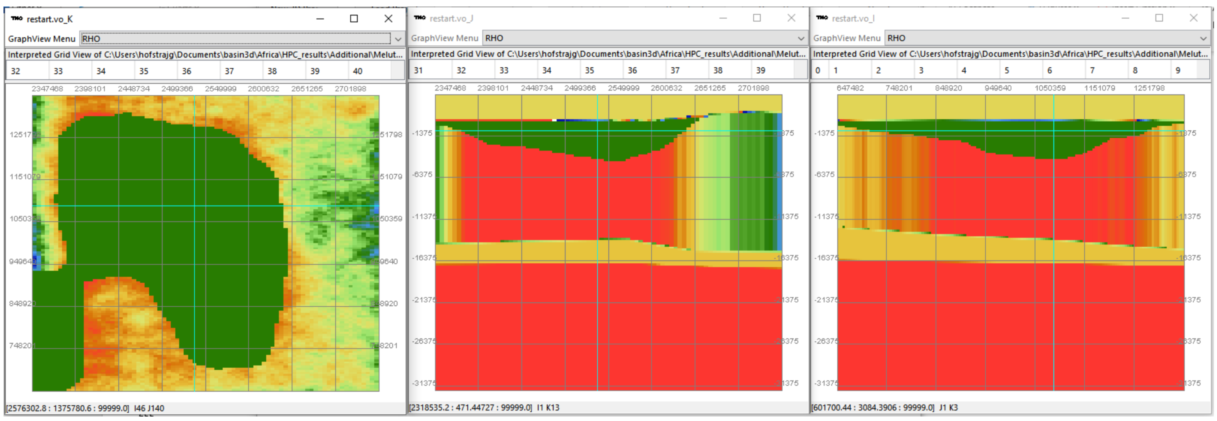

Northern Algeria

- Result observation VS model & Residual

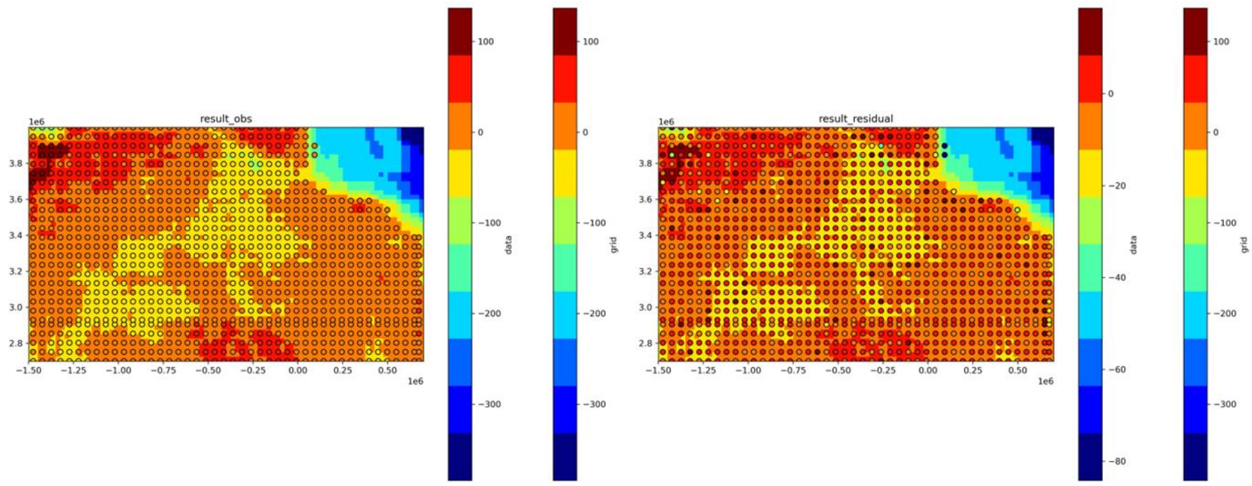

- Obs-Mod plot

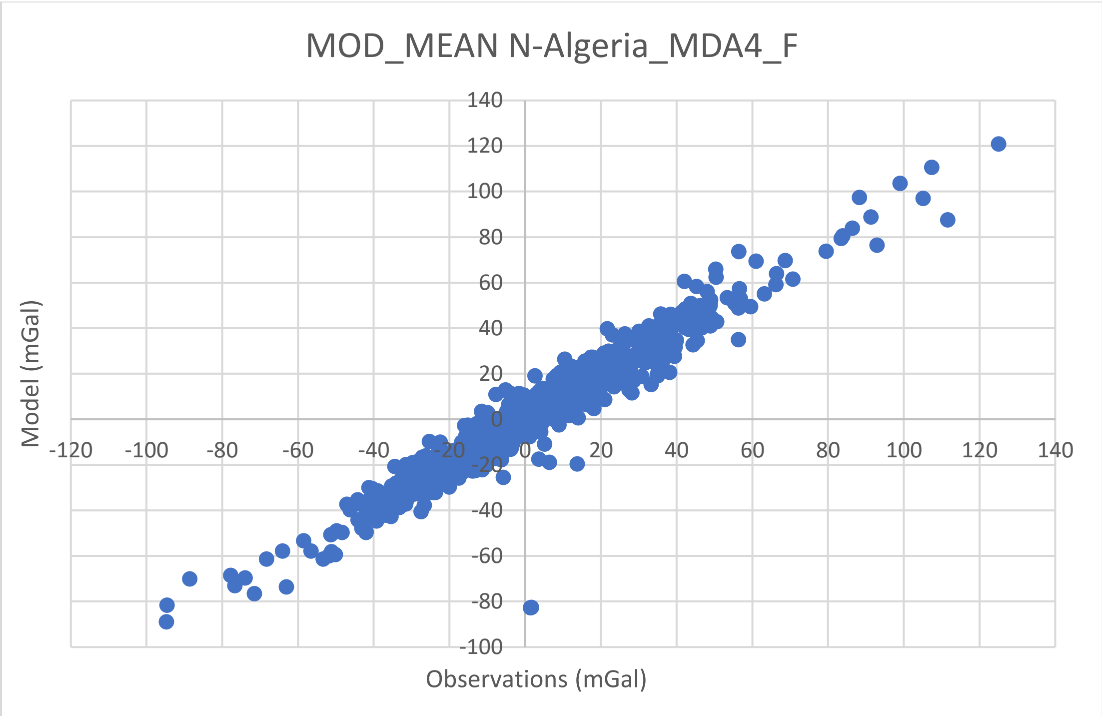

- Result sediment thickness prior & sediment thickness model

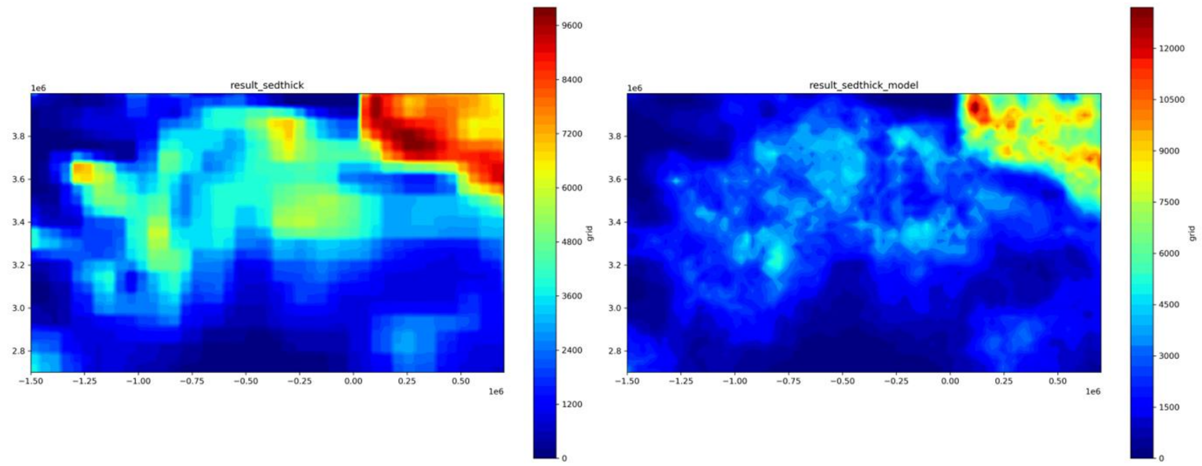

- Crustal density plot

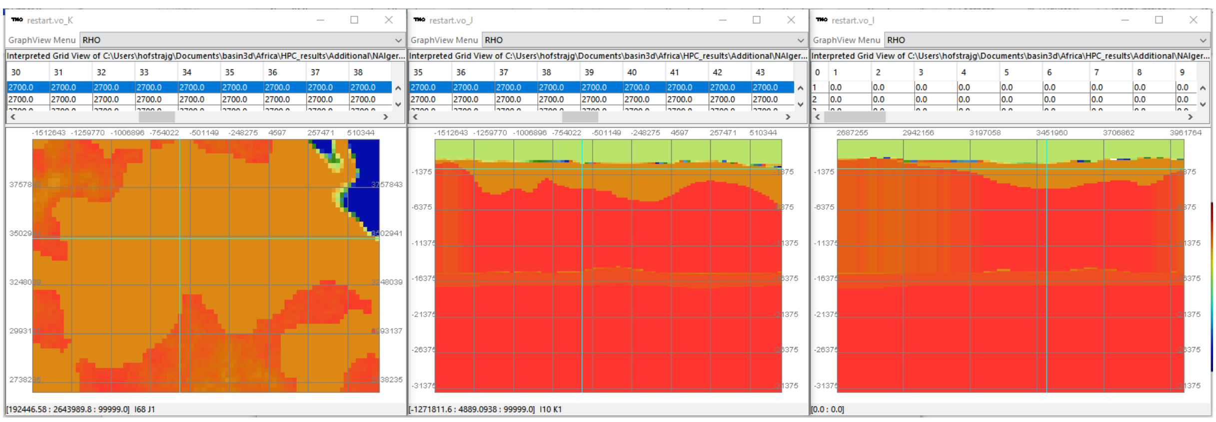

Sirte

- Result observation VS model & Residual

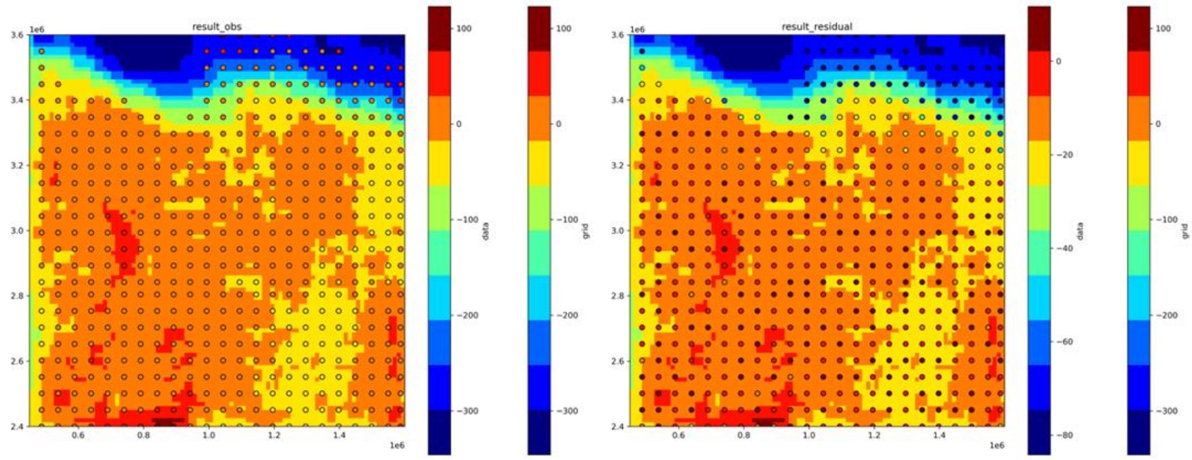

- Obs-Mod plot

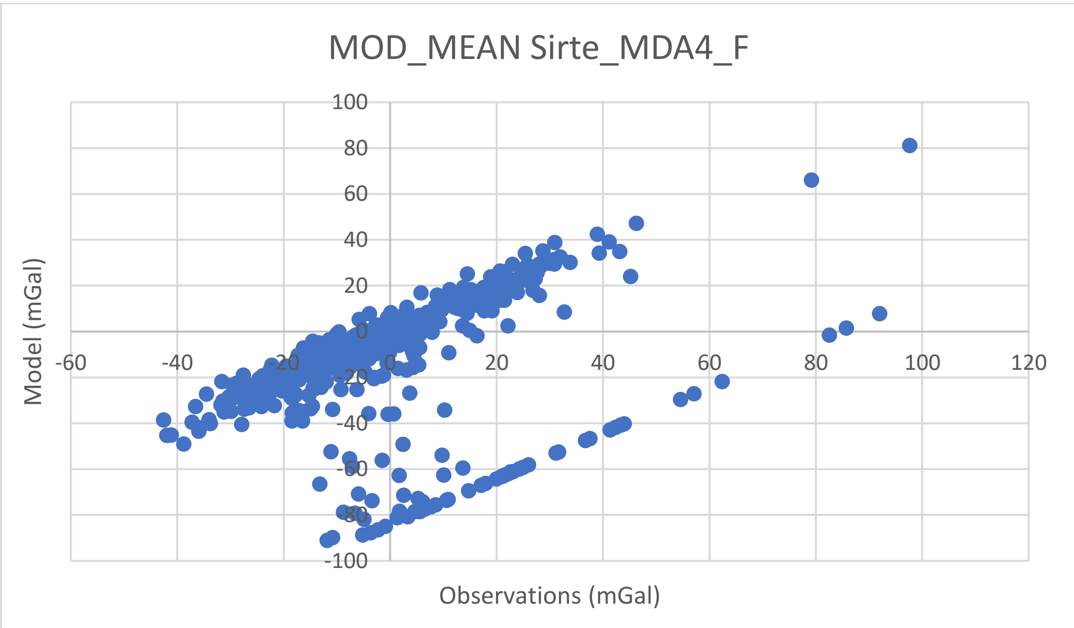

- Result sediment thickness prior & sediment thickness model

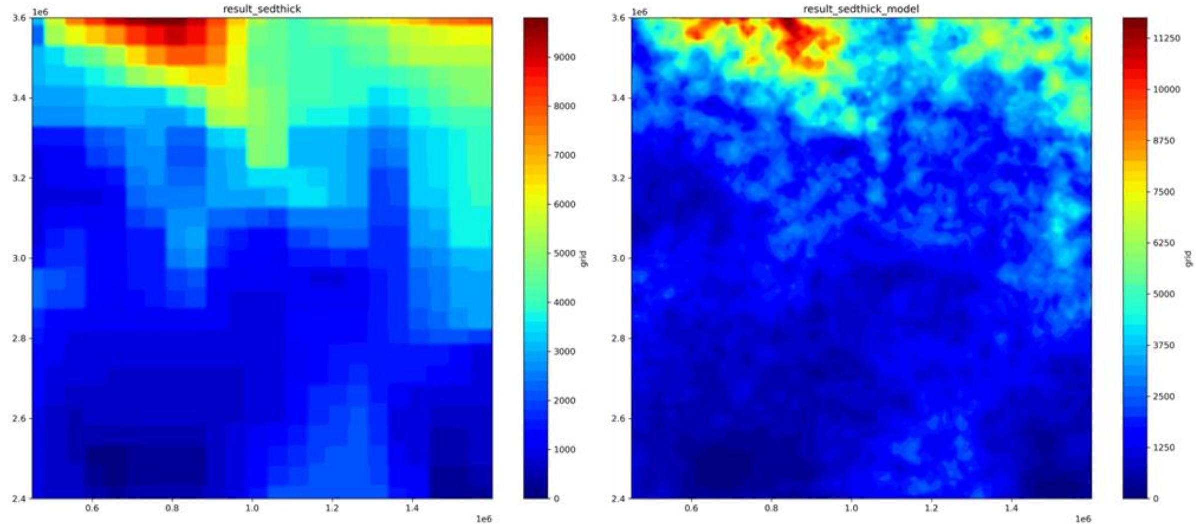

- Crustal density plot

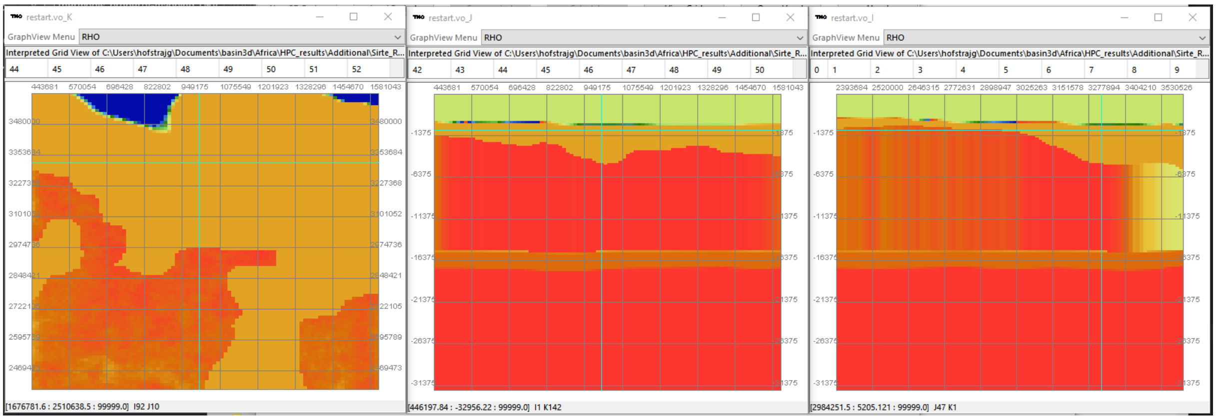

Taodeni

- Result observation VS model & Residual

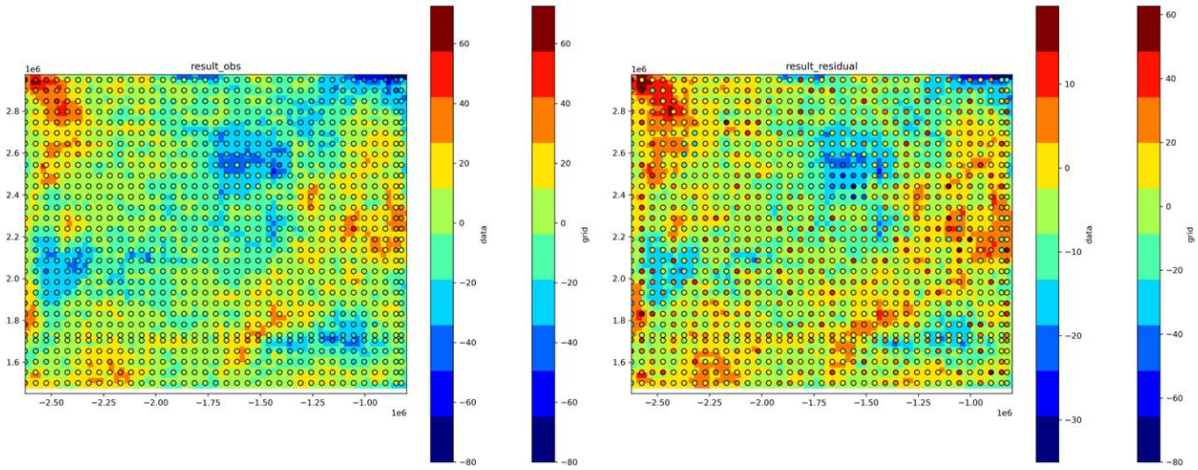

- Obs-Mod plot

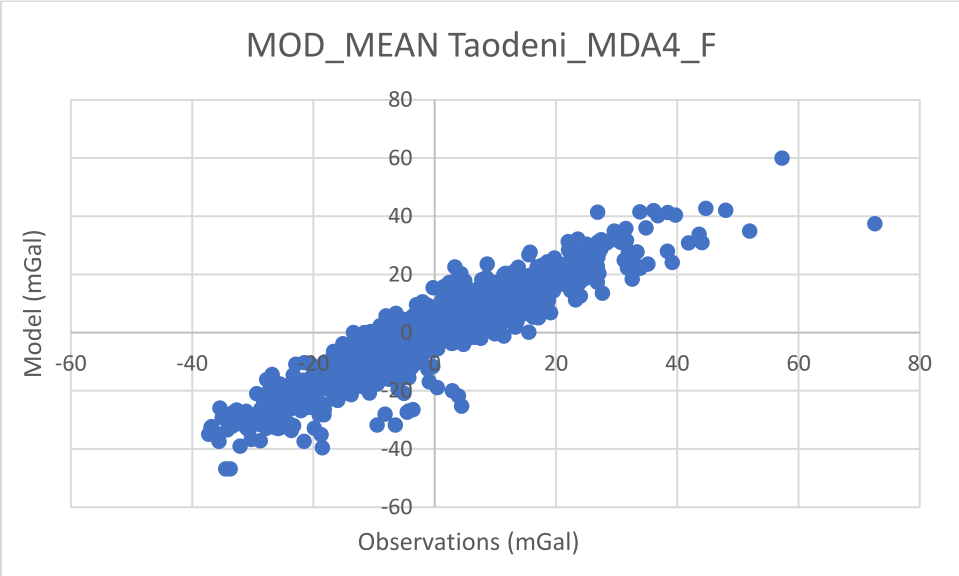

- Result sediment thickness prior & sediment thickness model

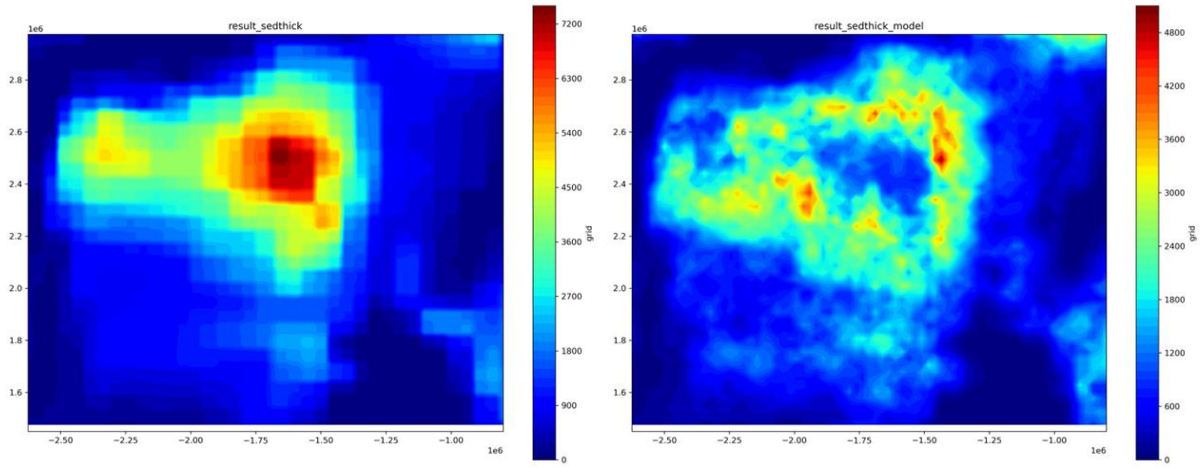

- Crustal density plot

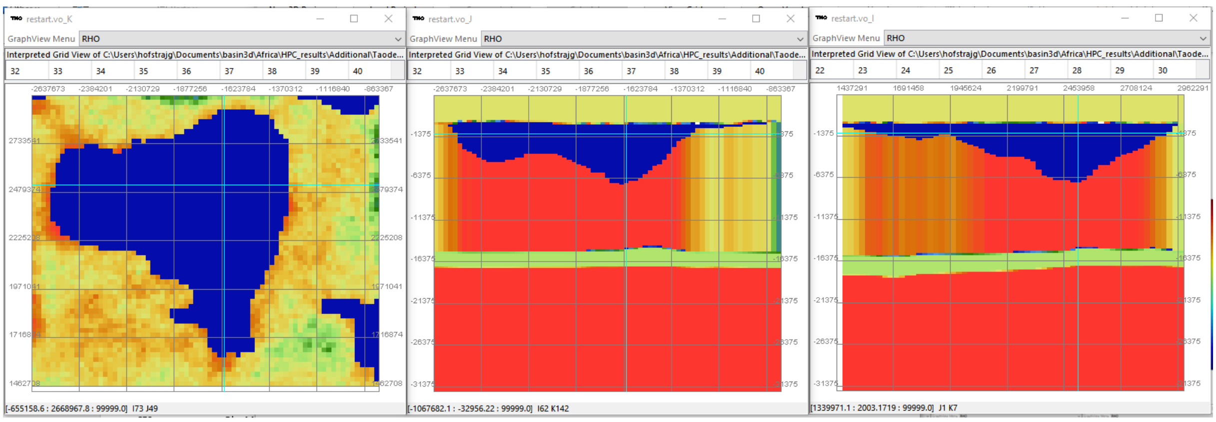

Termit

- Result observation VS model & Residual

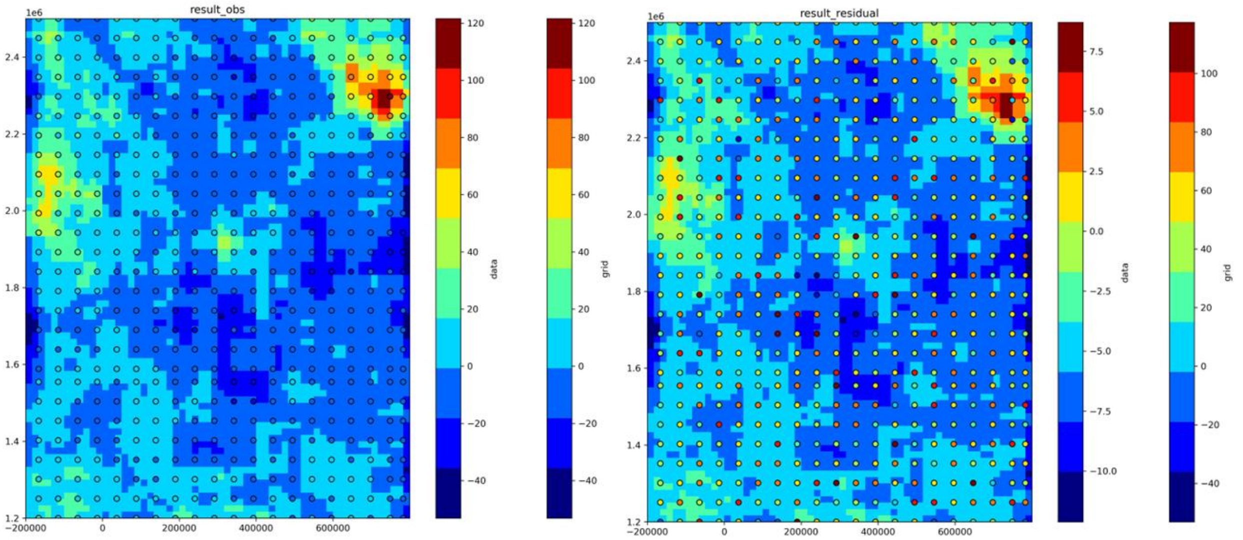

- Obs-Mod plot

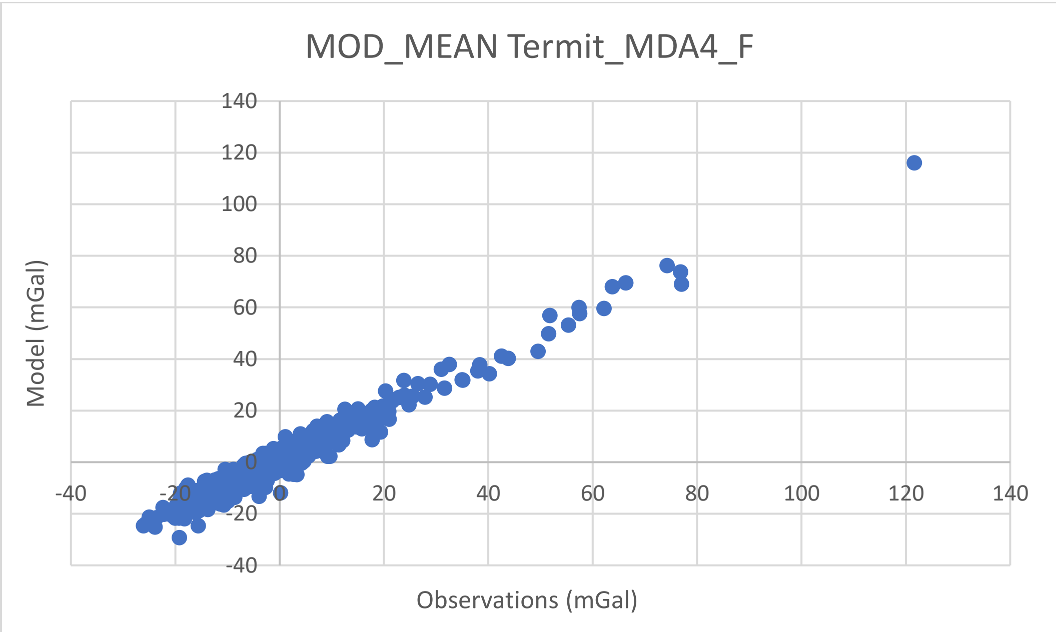

- Result sediment thickness prior & sediment thickness model

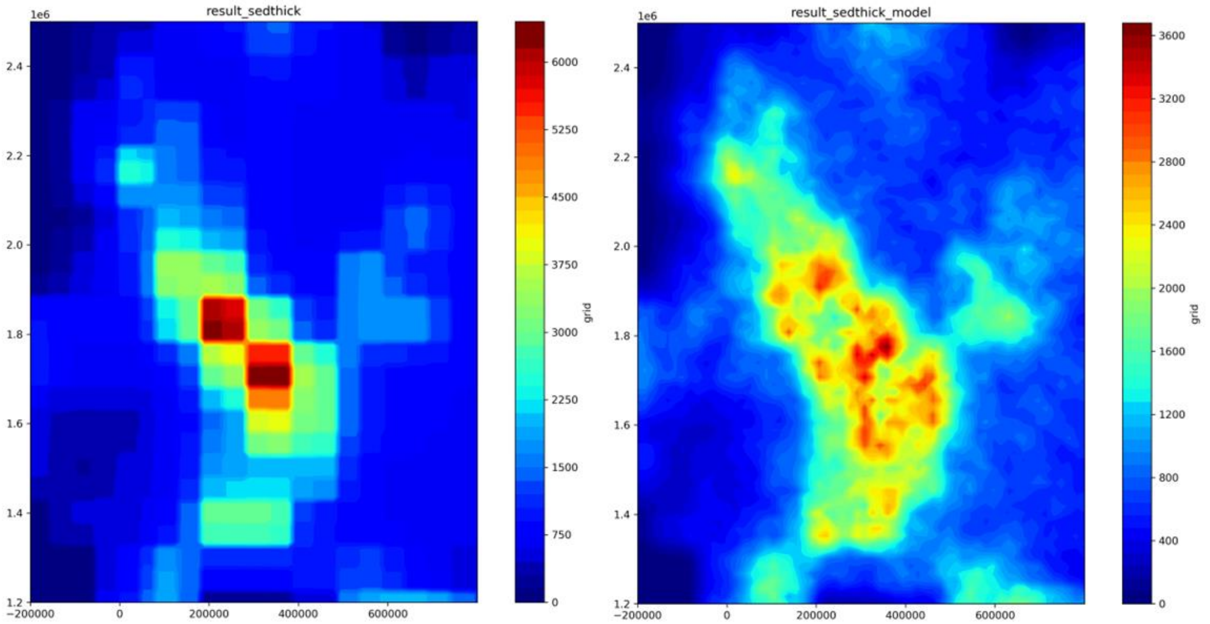

- Crustal density plot

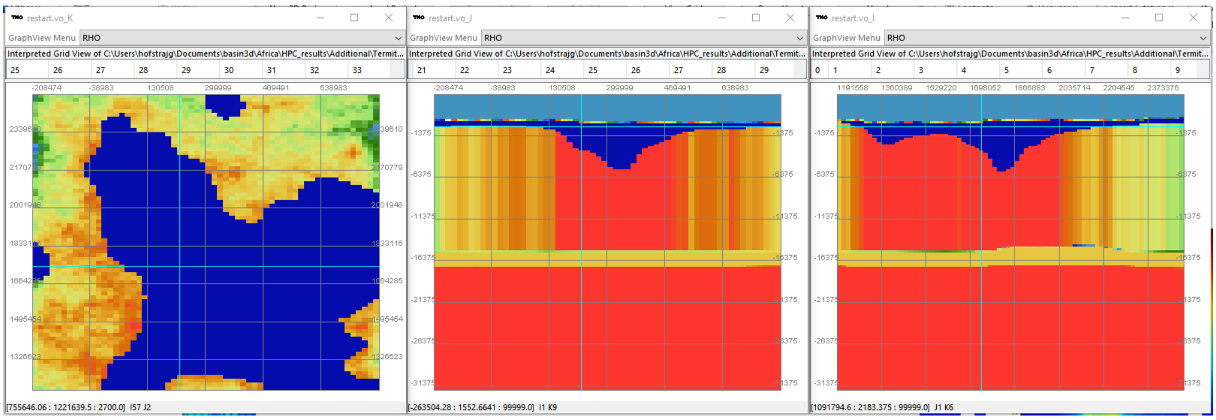

Tindouf

- Result observation VS model & Residual

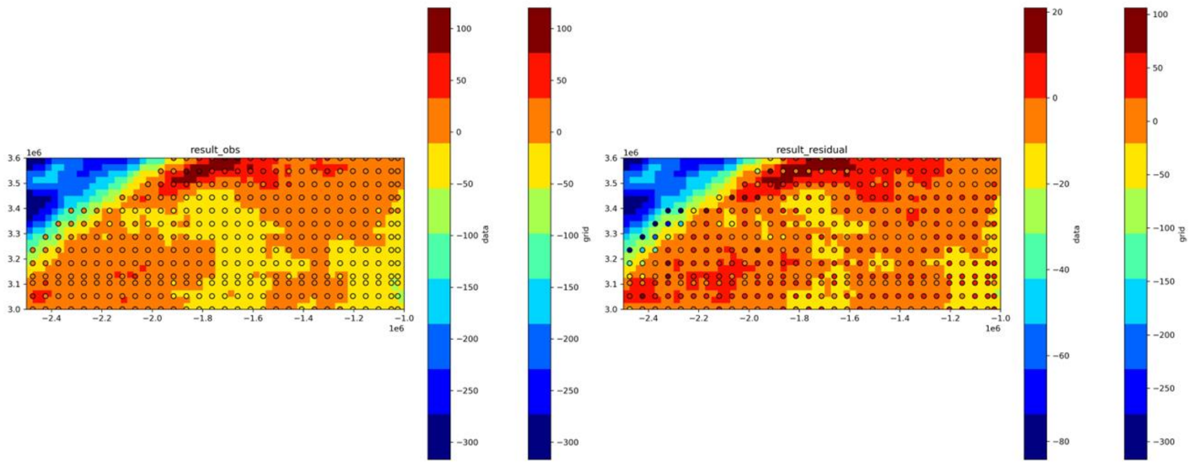

- Obs-Mod plot

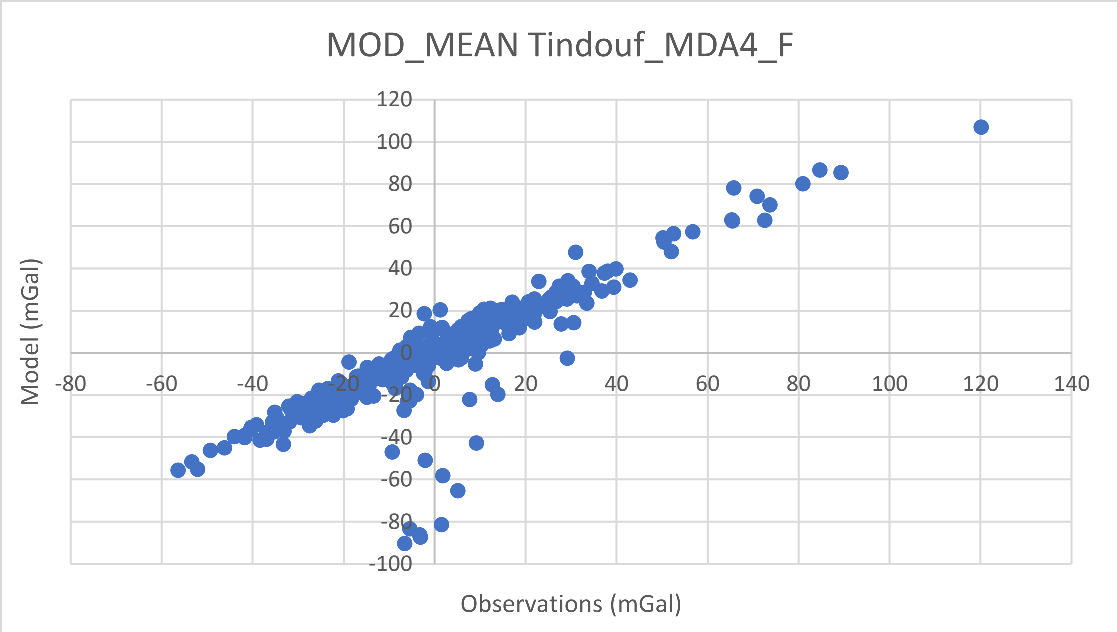

- Result sediment thickness prior & sediment thickness model

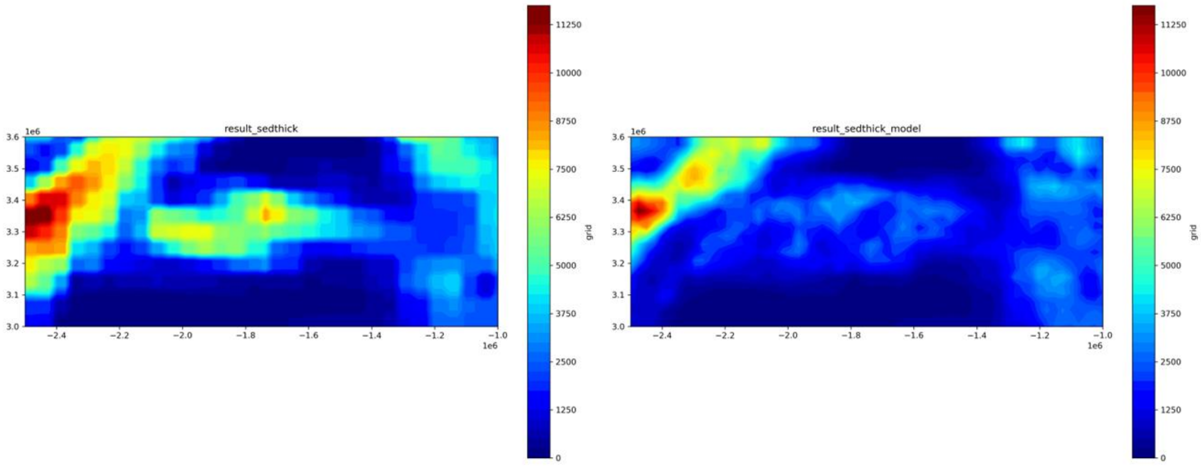

- Crustal density plot

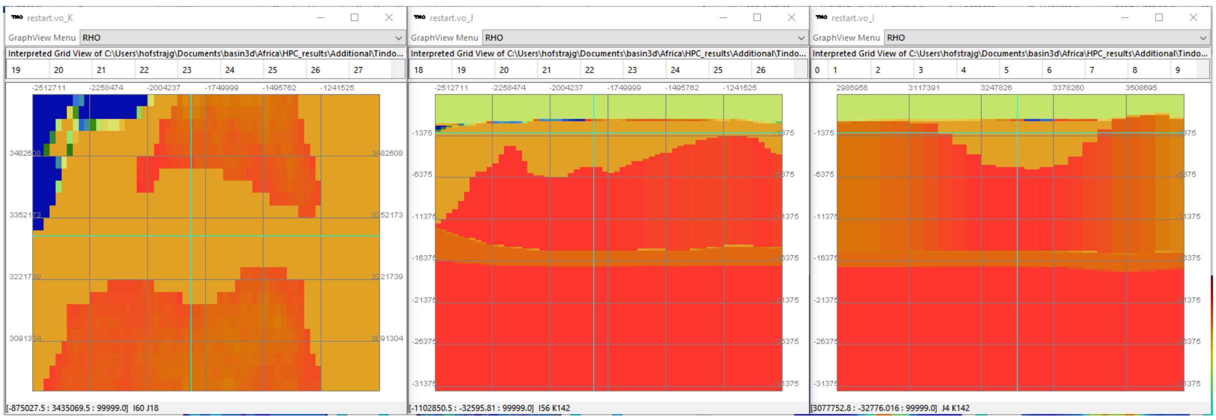

Upper-Egypt

- Result observation VS model & Residual

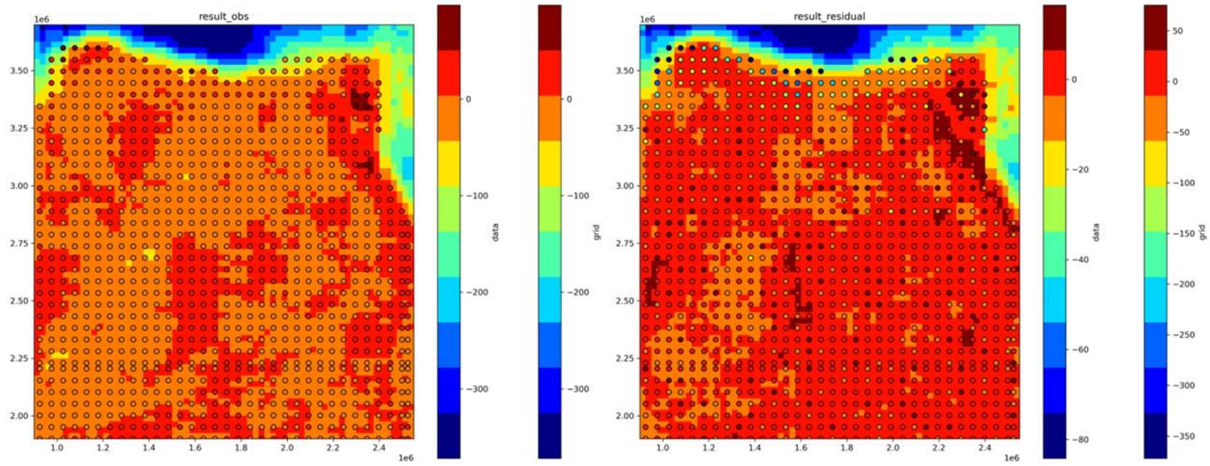

- Obs-Mod plot

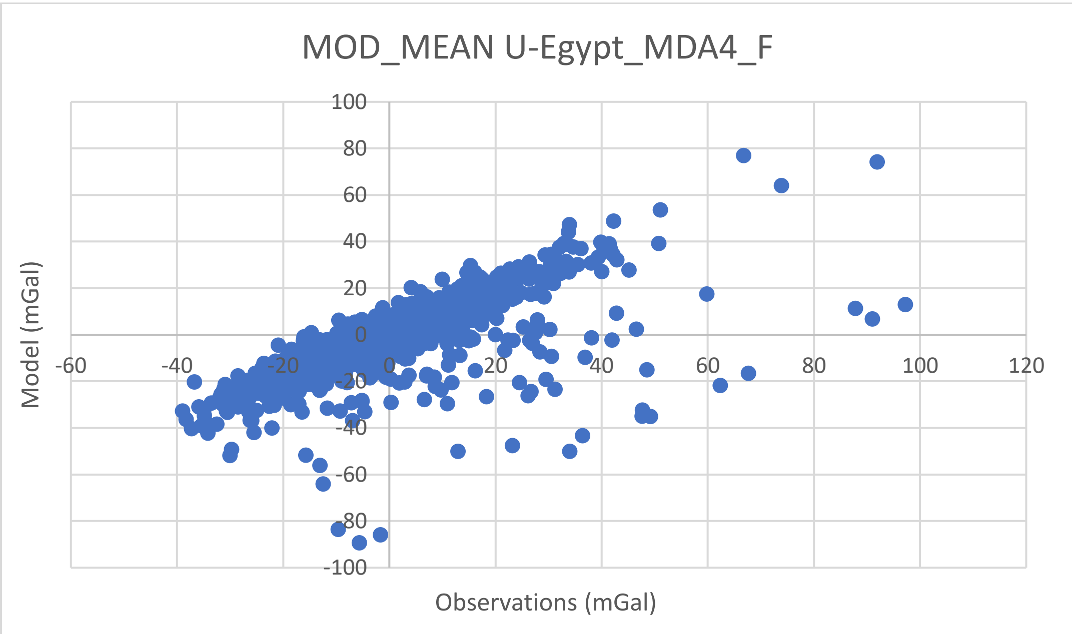

- Result sediment thickness prior & sediment thickness model

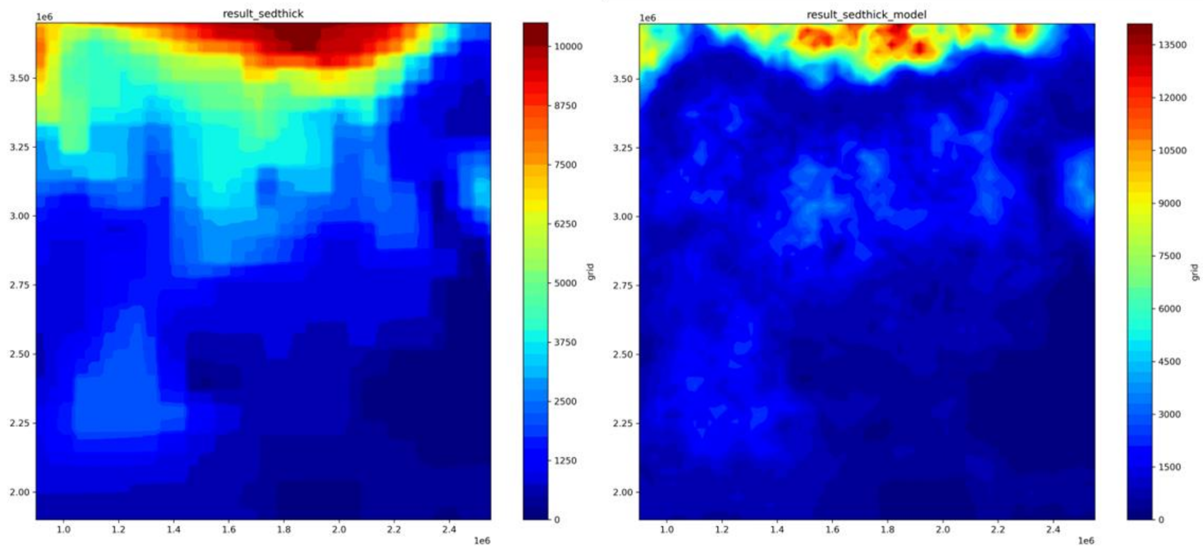

- Crustal density plot

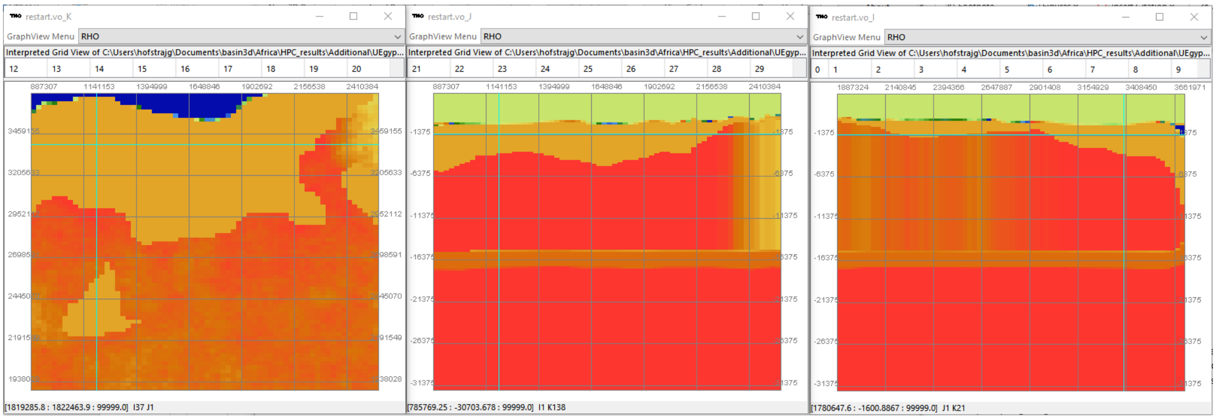

Volta

- Result observation VS model & Residual

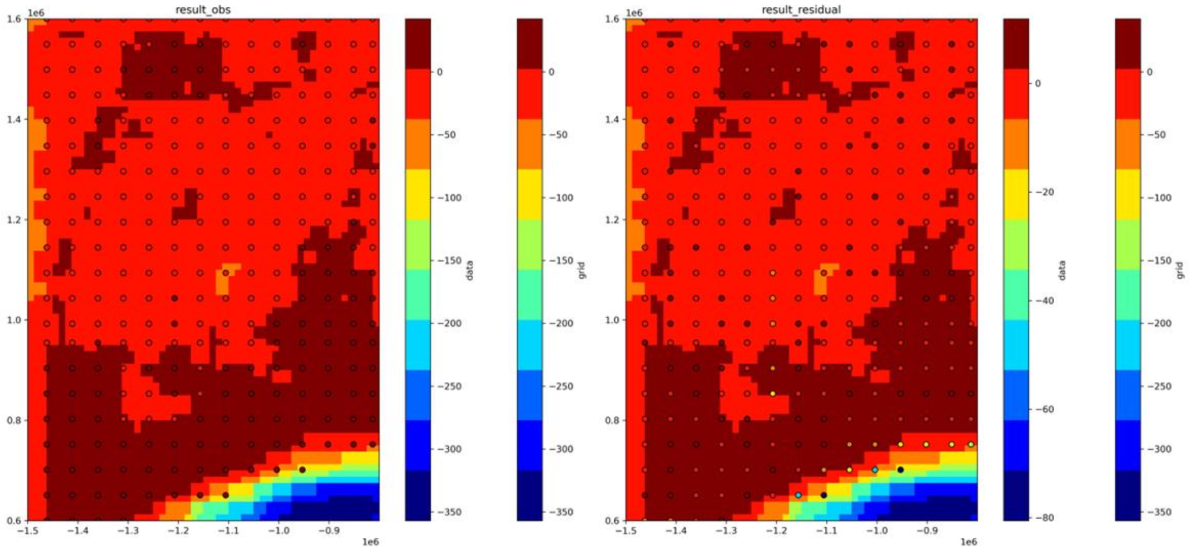

- Obs-Mod plot

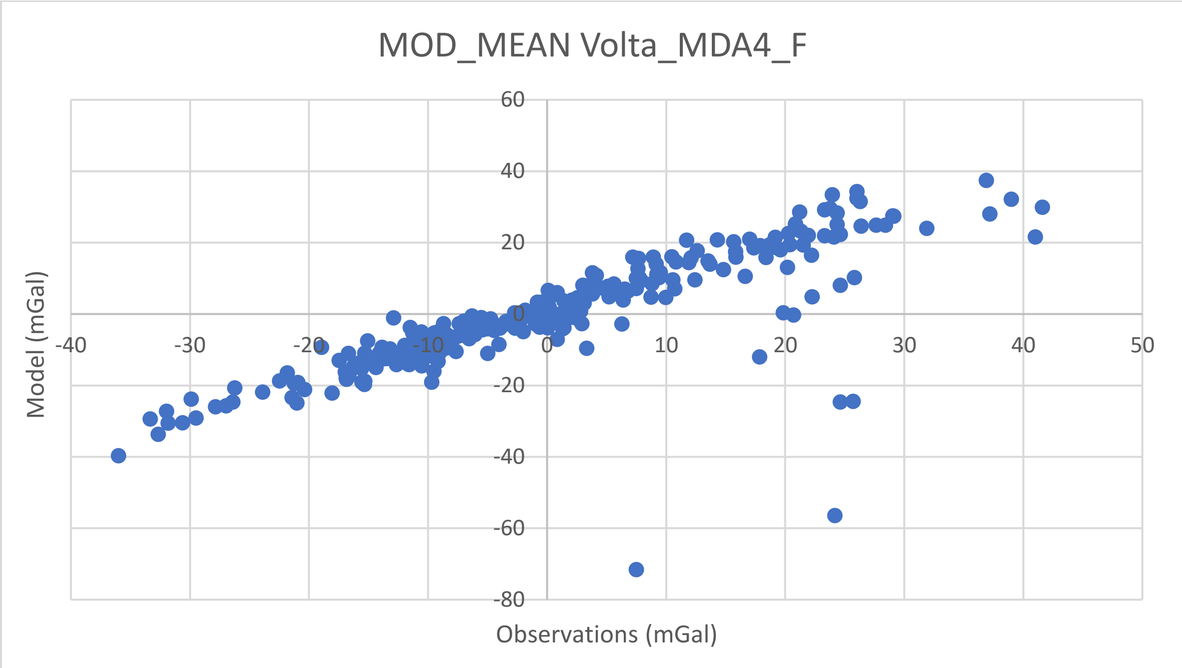

- Result sediment thickness prior & sediment thickness model

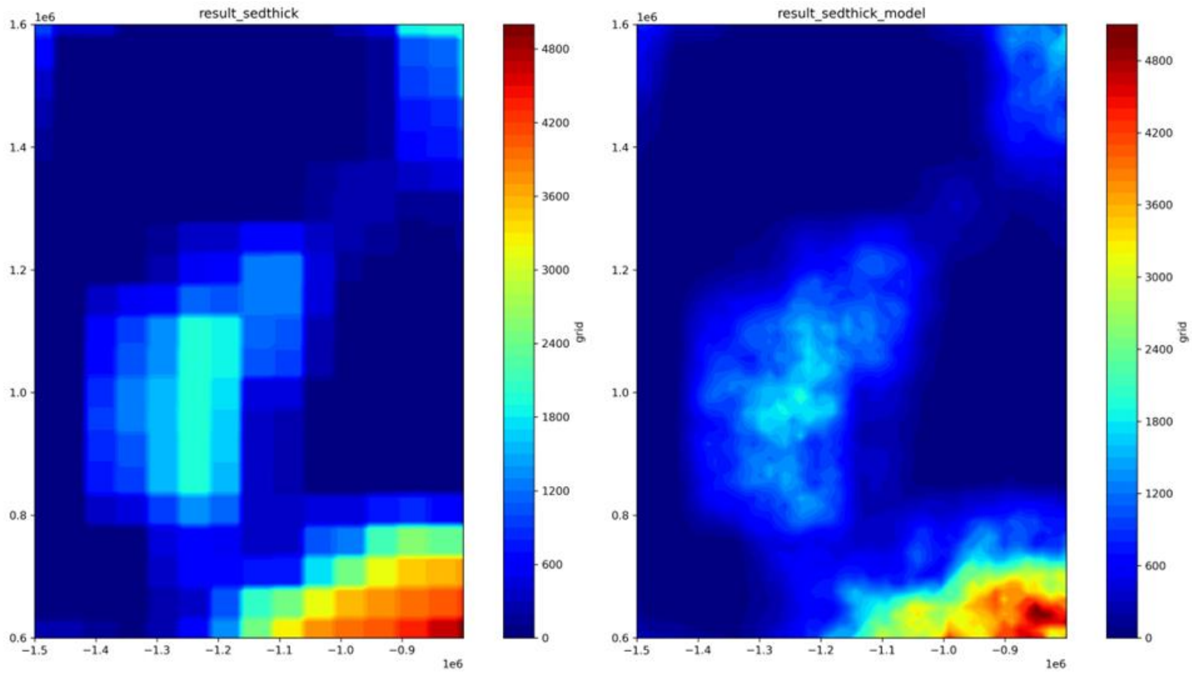

- Crustal density plot

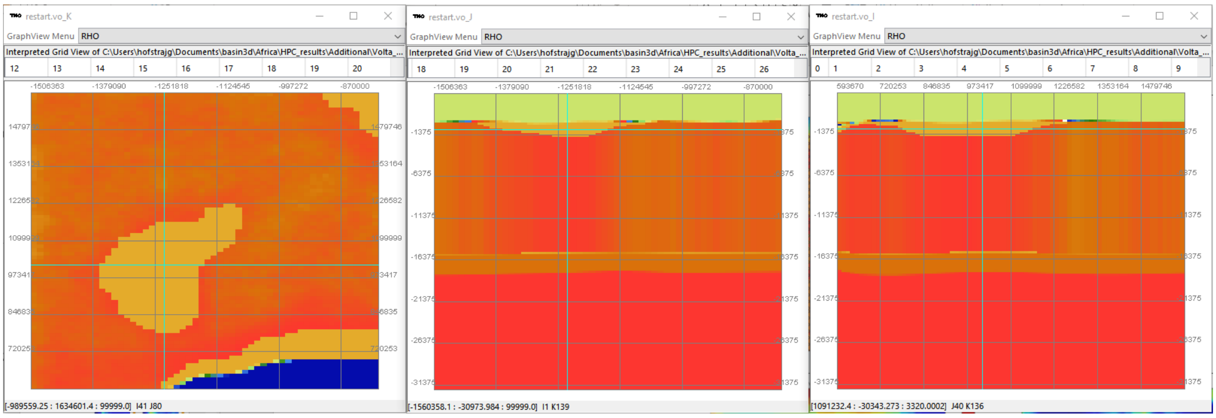

Zaire

- Result observation VS model & Residual

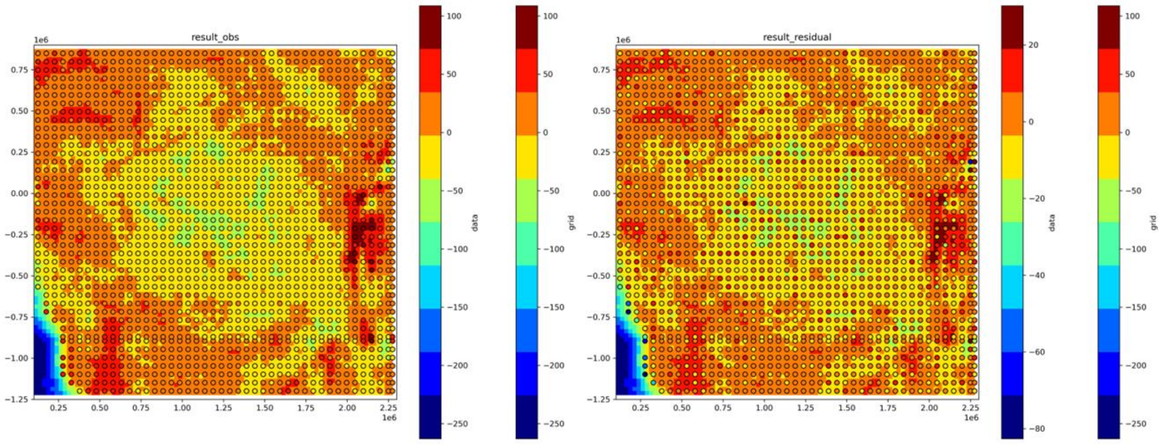

- Obs-Mod plot

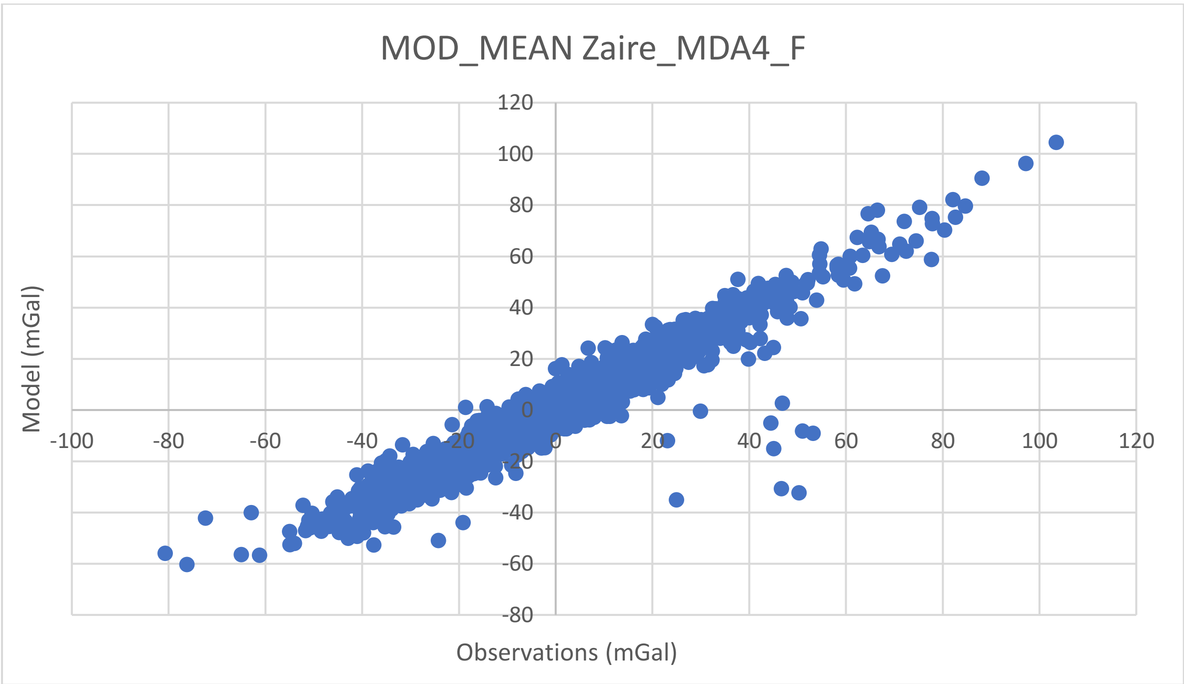

- Result sediment thickness prior & sediment thickness model

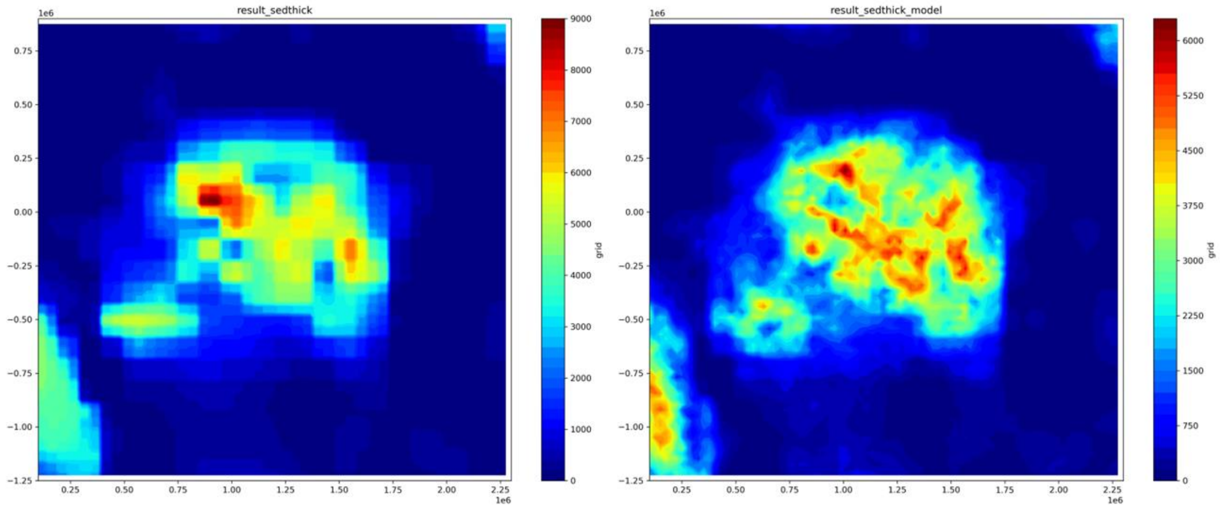

- Crustal density plot

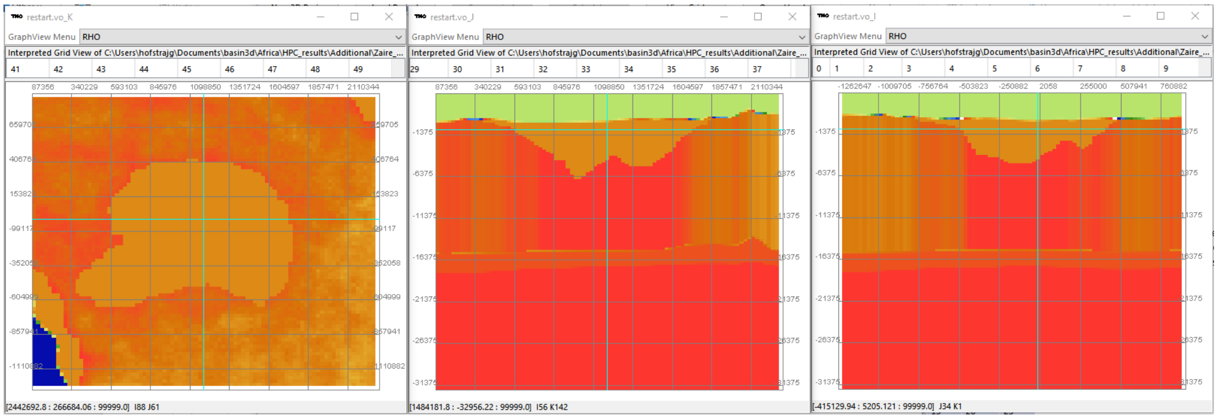

Northern SE Rifts

- Result observation VS model & Residual

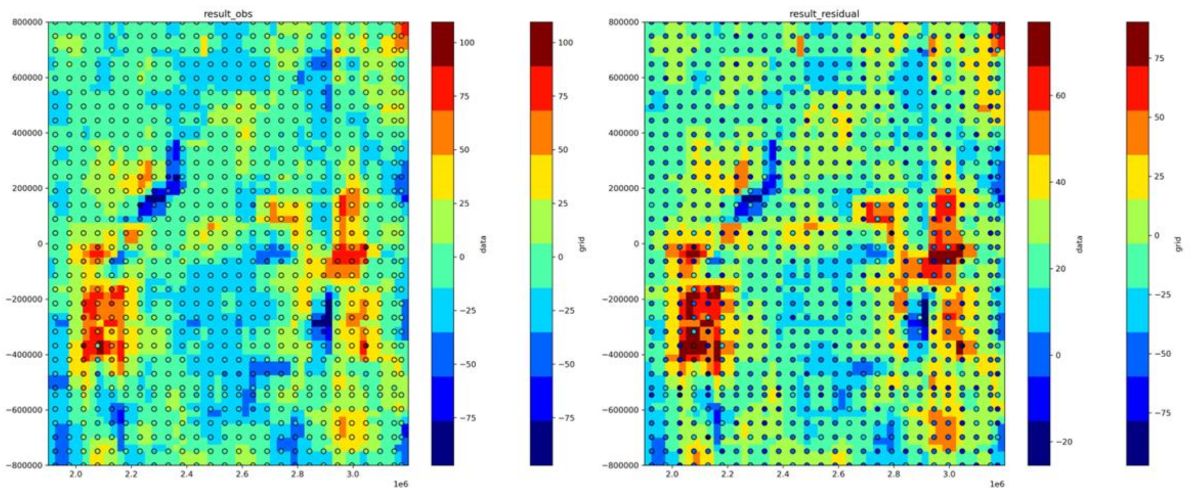

- Obs-Mod plot

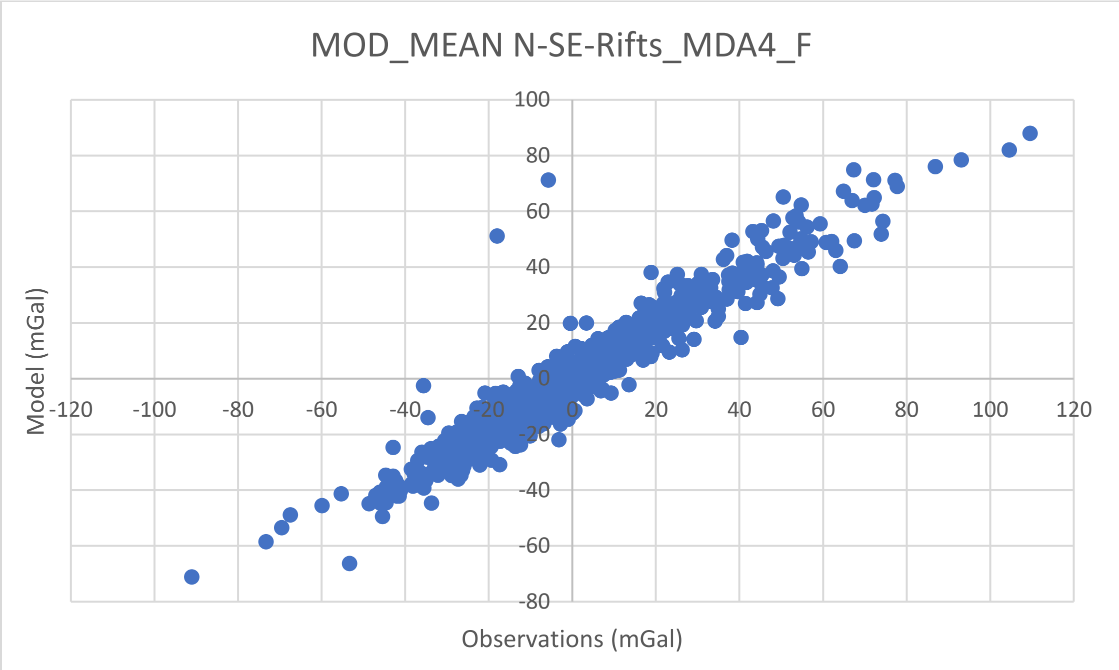

- Result sediment thickness prior & sediment thickness model

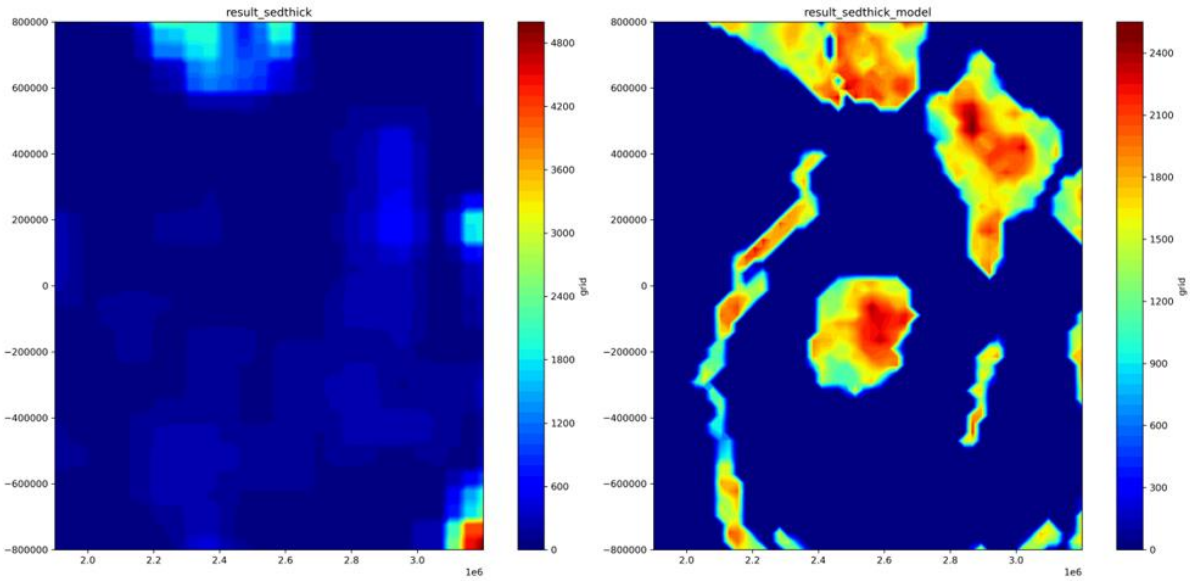

- Crustal density plot

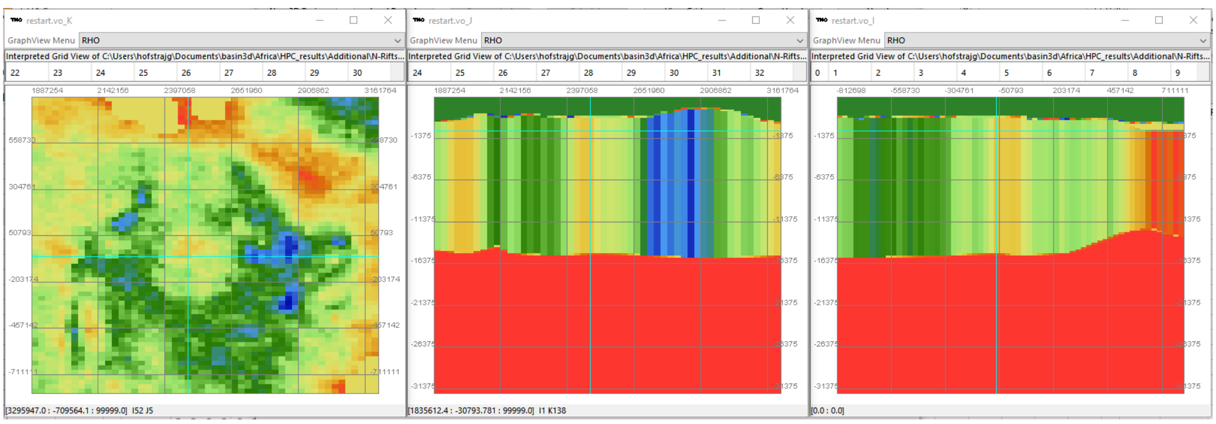

Southern SE Rifts

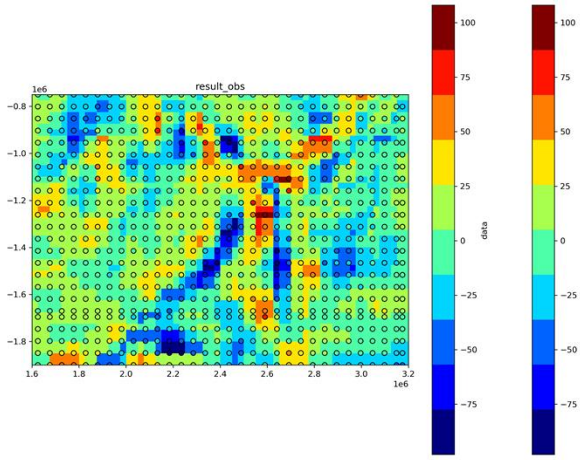

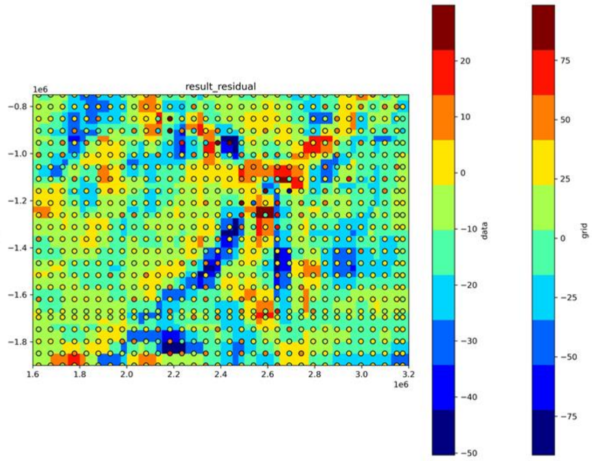

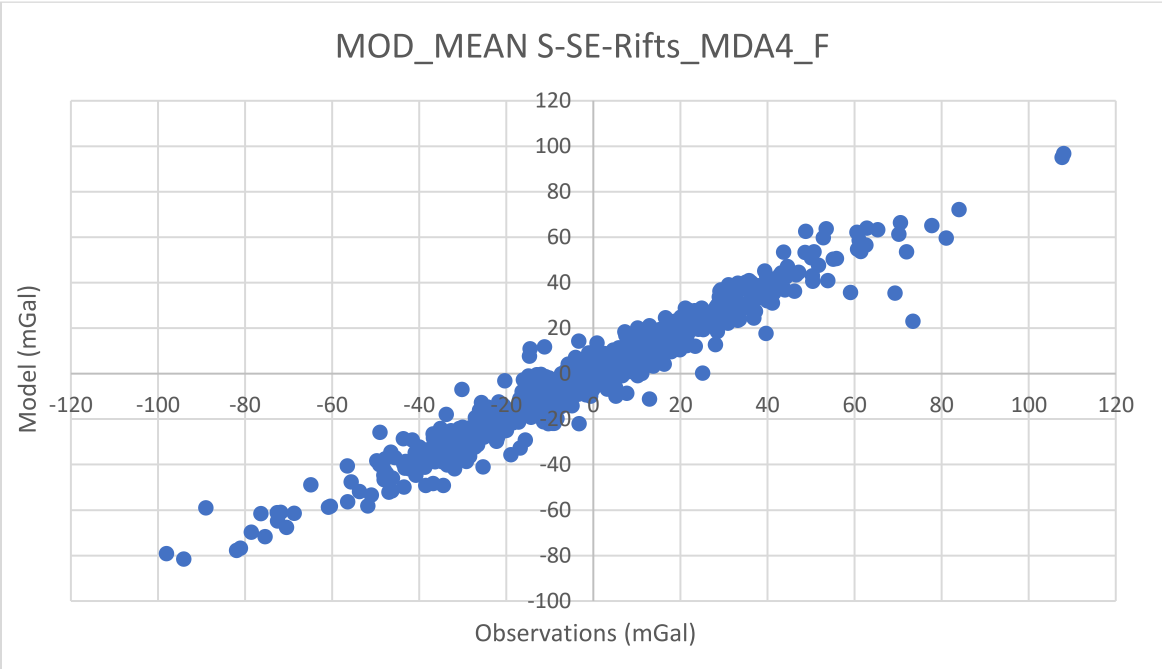

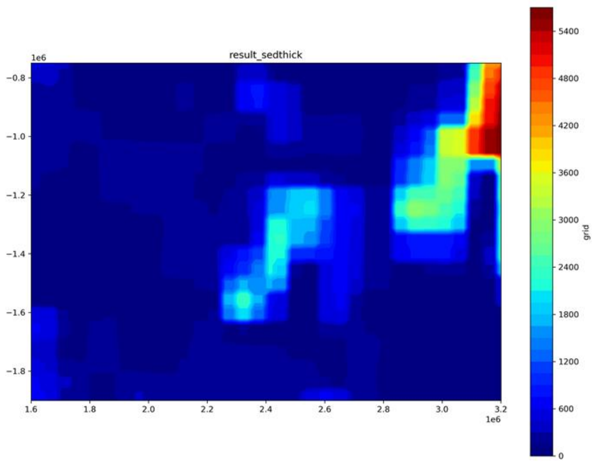

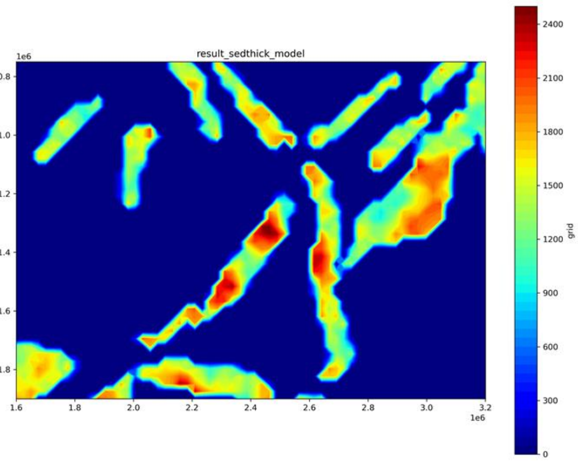

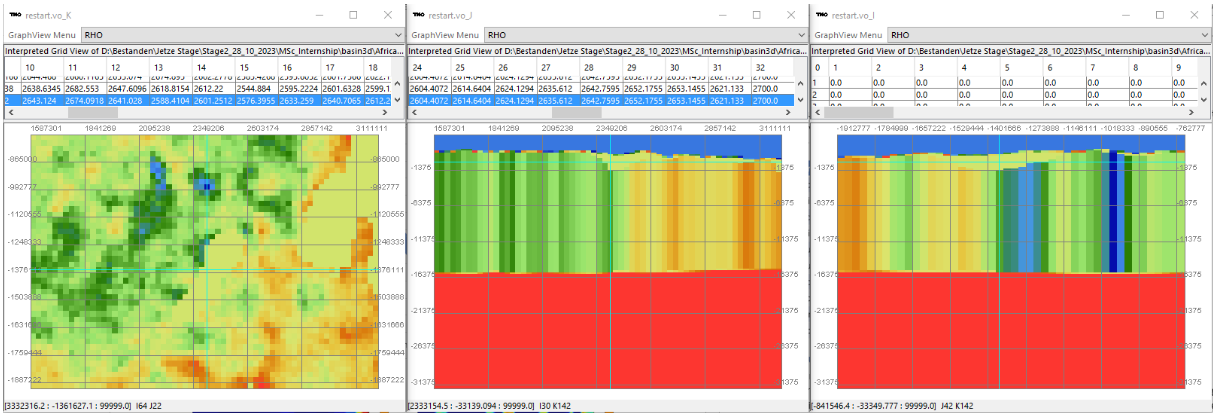
restart.vo_K
restart.vo_J
restart.vo_I
GraphView Menu
RHO
[3332316.2 : -1361627.1 : 99999.0] I64 J22
[2333154.5 : -33139.094 : 99999.0] I30 K142
[-841546.4 : -33349.777 : 99999.0] J42 K142